The MeerKAT Absorption Line Survey (MALS) Data Release. I. Stokes I Image Catalogs at 1-1.4 GHz

The Astrophysical Journal Supplement Series, 270:33 (37pp), 2024 February https://doi.org/10.3847/1538-4365/acf7b9

The MeerKAT Absorption Line Survey (MALS) Data Release. I. Stokes *I* Image Catalogs at 1–1.4 GHz

P. P. Deka[1], N. Gupta[1], P. Jagannathan[2], S. Sekhar[2,3], E. Momjian[2], S. Bhatnagar[2], J. Wagenveld[4], H.-R. Klöckner[4], J. Jose[5], S. A. Balashev[6,7], F. Combes[8], M. Hilton[9,10], D. Borgaonkar[1], A. Chatterjee[5], K. L. Emig[11,18], A. N. Gaunekar[5], G. I. G. Józsa[4,12], D. Y. Klutse[10,13], K. Knowles[12], J.-K. Krogager[14], A. Mohapatra[1], K. Moodley[10,13], Sébastien Muller[15], P. Noterdaeme[16], P. Petitjean[16], P. Salas[17], and S. Sikhosana[10,13]
[1] Inter-University Centre for Astronomy and Astrophysics, Post Bag 4, Ganeshkhind, Pune 411 007, India; parthad@iucaa.in
[2] National Radio Astronomy Observatory, Socorro, NM 87801, USA
[3] South African Radio Astronomy Observatory, 2 Fir Street, Black River Park, Observatory 7925, South Africa
[4] Max-Planck-Institut für Radioastronomie, Auf dem Hügel 69, D-53121 Bonn, Germany
[5] Thought Works Technologies India Private Limited, Yerawada, Pune 411 006, India
[6] Ioffe Institute, 26 Politeknicheskaya St., St. Petersburg, 194021, Russia
[7] HSE University, Saint Petersburg, Russia
[8] Observatoire de Paris, Collège de France, PSL University, Sorbonne University, CNRS, LERMA, Paris, France
[9] Wits Centre for Astrophysics, School of Physics, University of the Witwatersrand, Private Bag 3, 2050, Johannesburg, South Africa
[10] School of Mathematics, Statistics & Computer Science, University of KwaZulu-Natal, Westville Campus, Durban 4041, South Africa
[11] National Radio Astronomy Observatory, 520 Edgemont Road, Charlottesville, VA 22903, USA
[12] Department of Physics and Electronics, Rhodes University, P.O. Box 94, Makhanda 6140, South Africa
[13] Astrophysics Research Centre, University of KwaZulu-Natal, Durban 4041, South Africa
[14] Université Lyon1, ENS de Lyon, CNRS, Centre de Recherche Astrophysique de Lyon UMR5574, F-69230 Saint-Genis-Laval, France
[15] Department of Space, Earth and Environment, Chalmers University of Technology, Onsala Space Observatory, SE-43992 Onsala, Sweden
[16] Institut d'astrophysique de Paris, UMR 7095, CNRS-SU, 98bis bd Arago, F-75014 Paris, France
[17] Green Bank Observatory, 155 Observatory Road, Green Bank, WV 24915, USA
Received 2022 December 1; revised 2023 July 28; accepted 2023 August 10; published 2024 February 1

Abstract

The MeerKAT Absorption Line Survey (MALS) has observed 391 telescope pointings at the *L* band (900–1670 MHz) at $\delta \lesssim +20°$. We present radio continuum images and a catalog of 495,325 (240,321) radio sources detected at a signal-to-noise ratio (S/N) > 5 over an area of 2289 deg^2 (1132 deg^2) at 1006 MHz (1381 MHz). Every MALS pointing contains a central bright radio source ($S_{1\ \mathrm{GHz}} \gtrsim 0.2$ Jy). The median spatial resolution is 12″ (8″). The median rms noise away from the pointing center is 25 μJy beam^{-1} (22 μJy beam^{-1}) and is within $\sim$15% of the achievable theoretical sensitivity. The flux density scale ratio and astrometric accuracy deduced from multiply observed sources in MALS are <1% (8% scatter) and 1″, respectively. Through comparisons with NVSS and FIRST at 1.4 GHz, we establish the catalog's accuracy in the flux density scale and astrometry to be better than 6% (15% scatter) and 0.″8, respectively. The median flux density offset is higher (9%) for an alternate beam model based on holographic measurements. The MALS radio source counts at 1.4 GHz are in agreement with literature. We estimate spectral indices (α) of a subset of 125,621 sources (S/N > 8), confirm the flattening of spectral indices with decreasing flux density, and identify 140 ultra-steep-spectrum ($\alpha < -1.3$) sources as prospective high-z radio galaxies ($z > 2$). We have identified 1308 variable and 122 transient radio sources comprising primarily active galactic nuclei that demonstrate long-term (26 yr) variability in their observed flux densities. The MALS catalogs and images are publicly available at https://mals.iucaa.in.

Unified Astronomy Thesaurus concepts: Active galaxies (17); Radio interferometry (1346); Surveys (1671); Radio source catalogs (1356)

Supporting material: machine-readable tables

1. Introduction

Over the years, there have been several radio continuum surveys at centimeter wavelengths to study both the evolution of active galactic nucleus (AGN) and star formation (SF) activity across the Universe, independent of biases due to dust obscuration. The extragalactic nonthermal emission at $\sim$1 GHz arises from (i) magnetized plasma, i.e., radio core, jets, and lobes associated with AGNs (Padovani et al. 2017), and (ii) relativistic electrons associated with supernova remnants in star-forming galaxies (SFGs; Condon 1992).

The radio emission associated with SF activity is generally fainter and dominates the radio source population only below continuum flux densities of 100 μJy (e.g., Simpson et al. 2006; Seymour et al. 2008; Smolčić et al. 2017a; Algera et al. 2020; An et al. 2021). Consequently, radio source population studies have adopted a tiered approach in which deep small-area surveys focus on SFGs or radio-quiet quasars, and large area, shallow surveys encompass detections of powerful radio-loud AGN and nearby SFGs. The former category includes deepest radio surveys targeting a few square degrees of the sky with exquisite panchromatic coverage and reaching μJy level sensitivities (e.g.,

[18] Jansky Fellow of the National Radio Astronomy Observatory.

Garn et al. 2008; Smolčić et al. 2017b; Owen 2018; Mauch et al. 2020; Heywood et al. 2022).

The latter category historically comprised practically monochromatic surveys covering a large fraction of the entire visible sky, for example, the NRAO Very Large Array (VLA) Sky Survey (NVSS; Condon et al. 1998) and the Faint Images of the Radio Sky at Twenty Centimeters (FIRST; Becker et al. 1995), at 1.4 GHz. The NVSS observed the sky at declinations north of $\delta > -40°$ with a spatial resolution of 45″ and sensitivity of $\sim$0.45 mJy beam^{-1}. The FIRST survey covered over 10,000 deg^2 of the north and south Galactic caps with a resolution and sensitivity of 5″ and $\sim$0.15 mJy beam^{-1}, respectively, albeit with a lower surface brightness sensitivity than NVSS. These surveys are complemented by the Sydney University Molonglo Sky Survey (SUMSS; Mauch et al. 2003) at 843 MHz (resolution $\sim 45''/\sin\delta$; sensitivity $\sim$1 mJy beam^{-1}) surveying the southern sky at $\delta < -30°$ and avoiding the Galactic plane $|b| < 10°$, the Westerbork Northern Sky Survey (Rengelink et al. 1997) at 325 MHz surveying the entire sky north of $\delta > 30°$ at a 5σ rms sensitivity of 18 mJy and resolution of 54″ cosec δ, and the first Alternative Data Release (ADR1) of the TIFR GMRT Sky Survey (TGSS; Intema et al. 2017) surveying the northern sky at $\delta > -53°$ with a resolution of $\sim$25″ and median rms noise of $\sim$3.5 mJy beam^{-1} at 150 MHz.

The spectral energy distribution (SEDs) of radio sources derived from combining a large number of surveys at multiple frequencies is a fundamental tool to understand physical processes responsible for the radio emission (e.g., Rybicki & Lightman 1979; Prandoni et al. 2006; de Gasperin et al. 2018). For SFGs, SEDs involving measurements at high frequencies ($\nu > 2$ GHz) can be used to disentangle contributions to the radio emission due to free–free emission from H II regions and synchrotron emission from cosmic-ray electrons (e.g., Condon 1992; Niklas et al. 1997; Murphy et al. 2011; Tabatabaei et al. 2017; Linden et al. 2020; Algera et al. 2021; Stein et al. 2023). For radio-loud AGNs, the SED and its possible spatial variation can be used to understand the properties of ionized gas, estimate the age of radio plasma and identify young radio sources (age $<10^5$ yr) that are still embedded within the host galaxy's interstellar medium (e.g., Baum et al. 1990; Bicknell et al. 1997; de Vries et al. 1997; Murgia et al. 1999; Kameno et al. 2000; Snellen et al. 2000; Saikia & Gupta 2003; de Vries et al. 2009; Keim et al. 2019; Ricci et al. 2019; O'Dea & Saikia 2021). In addition, slow transients and variability of radio emission detected at timescales ranging from seconds, hours, days, to years, may be used to study a wide range of phenomena associated with stellar systems, supernovae, gamma-ray bursts (GRBs), and AGNs (Cordes et al. 2004).

Modern radio telescopes are capable of observing with large instantaneous bandwidths and, hence, efficiently delivering large radio source catalogs covering a wide frequency range and variability timescales required to address the above-mentioned science cases. Examples of such ongoing surveys are: the VLA Sky Survey (VLASS; Lacy et al. 2020; Gordon et al. 2021) at 2–4 GHz, the Rapid ASKAP Continuum Survey (RACS; McConnell et al. 2020; Hale et al. 2021) at 887.5 MHz, the Low Frequency Array Two-meter Sky Survey (LoTSS; Shimwell et al. 2017, 2019, 2022) at 120–168 MHz, the Galactic and Extragalactic All-sky Murchison Wide-field Array survey (GLEAM; Hurley-Walker et al. 2017) at 72–231 MHz and its extension GLEAM-X with improved sensitivity and resolution (Hurley-Walker et al. 2022), and the Evolutionary Map of the Universe survey (EMU; Norris et al. 2021) at 944 MHz. The spatial resolutions of these surveys are 2.″5 (VLASS), 15″–25″ (RACS), 6″ (LoTSS), 100″ (GLEAM; 45″ for GLEAM-X), and 11″–18″ (EMU). The Stokes-*I* sensitivities are 69 μJy beam^{-1}, 0.25–0.3 mJy beam^{-1}, 100 μJy beam^{-1}, 6–10 mJy beam^{-1} (1.27 mJy beam^{-1} for GLEAM-X), and 25–30 μJy beam^{-1}, respectively. These large area surveys are being complemented by deep small-area surveys such as MeerKAT International Gigahertz Tiered Extragalactic Exploration (MIGHTEE; Jarvis et al. 2017), which is imaging 20 deg^2 of the sky down-to thermal noise levels of <2 μJy beam^{-1}, although rms in the central regions is limited by confusion at $\sim$8″ resolution (Heywood et al. 2022). The combination of these surveys will enable large population studies of SFGs and AGNs, and the detection of extreme and rare objects.

The MeerKAT Absorption Line Survey (MALS) is observing $\sim$500 pointings, each centered at a radio source brighter than $\sim$200 mJy at 1 GHz, with the *L* band (900–1670 MHz) and *UHF* band (580–1015 MHz) of the MeerKAT telescope (Gupta et al. 2016). It will deliver a radio continuum catalog of about *one million radio sources* from the sky coverage of $\sim$1000 deg^2 at a sensitivity of $\sim$20 μJy beam^{-1}. The MeerKAT telescope consists of 64 dishes of 13.5 m diameter located at the Square Kilometre Array (SKA) site in Karoo, South Africa (Jonas & MeerKAT Team 2016). For reference, MeerKAT's field of view, i.e., the FWHM of the primary beam and spatial resolution[19] at $\sim$1 GHz, are 88′ and $\sim$10″, respectively (Mauch et al. 2020).

While the radio continuum component of MALS will enable a wide a range of radio continuum science associated with SFGs, AGNs, and clusters of galaxies (see Gupta et al. 2016, for details), its uniqueness lies in that for each pointing the survey will also produce spectral line cubes at a spectral resolution of $\sim$6.1 km s^{-1}. Consequently, for each radio source brighter than 1 mJy it will also be possible to search for cold atomic and molecular gas associated with AGNs via H I 21 cm and OH 18 cm absorption lines at $0 < z < 1.4$ and $0 < z < 1.9$, respectively (e.g., Combes et al. 2021; Gupta et al. 2021; Srianand et al. 2022). MALS is also enabling the most sensitive and comprehensive search for radio recombination lines nominally arising from hydrogen in ionized gas at $z \lesssim 5$ (Emig et al. 2023). These observations enable the direct exploration of the relationship between cold gas, ionized gas, and AGN/SF activity over the redshift range ($0 < z < 2$) in which maximum evolution in these quantities takes place (e.g., Hopkins & Beacom 2006; Silverman et al. 2009; Fanidakis et al. 2012; Heckman & Best 2014).

In this paper, we describe the first release of MALS Stokes-*I* continuum data products for the 391 pointings observed at the *L* band during the first phase of the survey (see Figure 1 for the sky coverage). The subsequent MALS observing phases will largely observe in the *UHF* band. We focus on two spectral ranges in the *L* band: 976.4–1036.5 MHz and 1350.9–1411.0 MHz, hereafter referred to as SPW2 and SPW9, respectively. We utilize the properties of SPW9 images and their comparison with the NVSS catalog, also at $\sim$1.4 GHz, to demonstrate the quality of the catalog. The processes presented here lay out the foundation for

[19] Based on `robust = −1.3` weighting of visibilities as implemented in the Astronomical Image Processing System (Greisen 2003) used in Mauch et al. (2020).

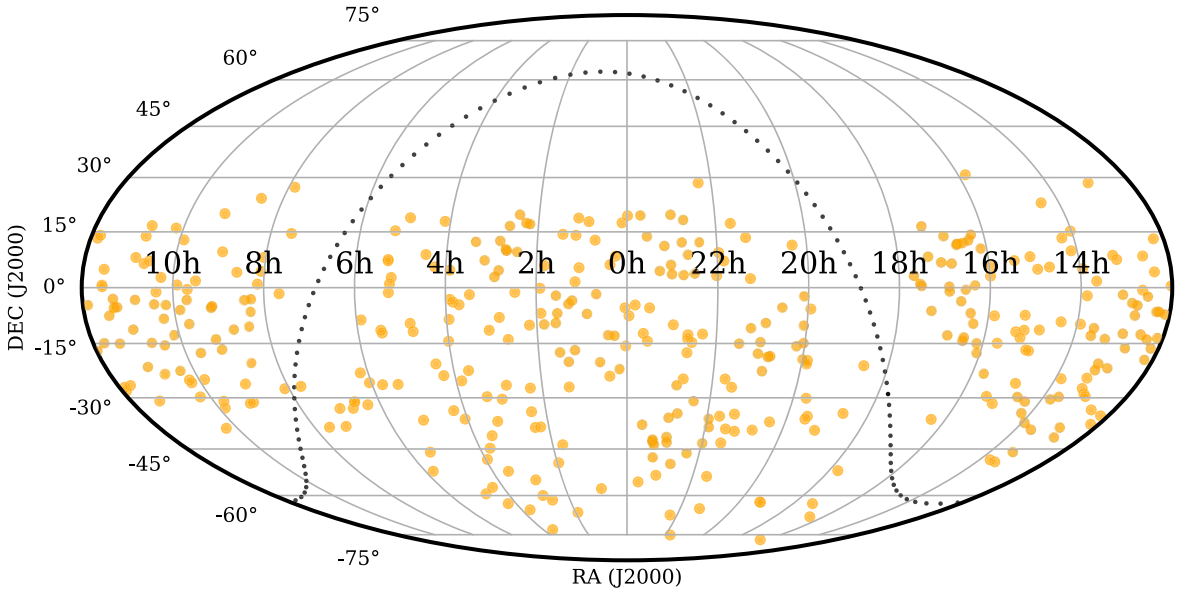

Figure 1. Sky distribution of the 391 MALS pointings observed in the *L* band shown in Mollweide projection in equatorial coordinates (J2000). The dotted line marks the Galactic plane.

subsequent *L*- and *UHF*-band data releases corresponding to narrowband, i.e., SPW specific, and wideband continuum products. For value addition to the community, the SPW2 data products are included in this first data release. The catalog and initial results from wideband imaging of 10 MALS pointings are presented in Wagenveld et al. (2023).

This paper is structured as follows. In Section 2, we present details of observations and data analysis for the 391 pointings that are part of this data release. In Section 3, we describe the noise properties of the images, and analyze artifacts. The cataloging procedure, which will also be used for future continuum data releases, is also presented here. In Section 4, we investigate the accuracy of the astrometry and the flux density scale. In this context, we make a detailed comparison with NVSS, and elaborate on the primary beam correction. In Section 5, we use the MALS catalog to determine radio source counts and discuss the completeness of the catalog. Further, we demonstrate the usage of the catalog to potential users by investigating the long-term variability at 1.4 GHz and spectral indices of the radio source population over 0.3–1000 mJy. The results and future prospects are summarized in Section 6.

Throughout this paper, we use ΛCDM cosmology with $\Omega_m = 0.315$, $\Omega_\Lambda = 0.685$, and $H_0 = 67.4\,\mathrm{km\,s^{-1}\,Mpc^{-1}}$ (Planck Collaboration et al. 2020). All of the positions are provided in J2000 equatorial coordinates. The spectral index, α, is defined as $S_\nu \propto \nu^\alpha$, where S_ν is flux density at frequency ν.

2. Observations, Calibration, and Imaging

Each MALS pointing is centered at a radio source brighter than 200 mJy at ∼1 GHz in NVSS or SUMSS. We have carried out a large spectroscopic campaign using the Nordic Optical Telescope (NOT) and the Southern African Large Telescope (SALT) to measure the redshifts and confirm the nature of 303 AGN candidates identified on the basis of mid-infrared colors. The NOT component of the survey is presented in Krogager et al. (2018). Gupta et al. (2022) present the details of the SALT campaign and the selection process of the pool of 650 radio sources based on which approximately 500 pointings are anticipated to be observed at both the *L* and *UHF* bands using ∼1655 hr of MeerKAT time.

The sky coverage of 391 pointings observed at the *L* band during the first phase of the survey from 2020 April 1 to 2021 January 18, is shown in Figure 1 (see Appendix A for the list). For these observations, the 856 MHz bandwidth of the *L* band centered at 1283.9869 MHz was split into 32,768 frequency channels. This mode of the SKA Reconfigurable Application Board correlator corresponds to a channel spacing of 26.123 kHz, which is $6.1\,\mathrm{km\,s^{-1}}$ at the center of the band. The correlator dump time was 8 s. For dual, linearly polarized *L*-band feeds with orthogonal polarizations labeled X and Y, the data were acquired for all four polarization products: XX, XY, YX, and YY. On average, 59 antennas of MeerKAT-64 array participated in these observations.

Typically, a single *L*-band observing run included three targets. The total on-source time of 56 minutes on each target was split into three scans of 1120 s duration at different hour angles to improve the uv-coverage. Each scan on a target source was bracketed by a 60 s long scan on a complex gain calibrator. We also observed 3C 286, 3C 138, PKS 1939-638, and/or PKS 0408-658 for 5–10 minutes at the start, middle, and end of an observing run for flux density scale, delay, and bandpass calibrations. Thus, the total duration of an *L*-band observing run was about 3.5 hr, which resulted in a measurement set of ∼5 TB. There are five exceptions to this observing scheme. Four MALS pointings were observed twice, i.e., have a total on-source time of 112 minutes (see Appendix A for details), and the time on J183339.98−210339.9 (PKS 1830-211) is 90 minutes.

The MALS data were processed using the Automated Radio Telescope Imaging Pipeline (ARTIP) based on NRAO's Common Astronomy Software Applications (CASA) package (The CASA Team et al. 2022). The details are provided in Gupta et al. (2021). In short, since here we are interested in Stokes-*I* imaging, for processing we generated a measurement set consisting of only XX and YY polarization products. We also dropped channels at the extreme edge of the bandpass

Table 1
Details of *L*-band SPWs

SPW Id. (1)	Freq. Range (MHz) (2)	Image Freq. (MHz) (3)
SPW0	869.4–929.5	904.1
SPW1	922.9–983.0	952.9
SPW2	**976.4–1036.5**	**1006.0**
SPW3	1029.9–1090.0	1060.3
SPW4	1083.4–1143.5	1109.7
SPW5	1136.9–1197.0	1191.7
SPW6	1190.4–1250.5	1220.8
SPW7	1243.9–1304.0	1273.9
SPW8	1297.4–1357.5	1331.6
SPW9	**1350.9–1411.0**	**1380.9**
SPW10	1404.4–1464.5	1434.4
SPW11	1457.9–1518.0	1487.9
SPW12	1511.4–1571.5	1541.4
SPW13	1564.9–1625.0	1614.5
SPW14	1618.4–1671.9	1643.0

Note. Column (1): Spectral window (SPW) ID. The SPWs of interest in this paper are highlighted in bold. Column (2): frequency range covered by the corresponding visibility measurement set. Column (3): reference frequency of the continuum image.

resulting in a measurement set with 30,720 frequency channels. An initial radio-frequency interference (RFI) mask described in Gupta et al. (2021) was applied to exclude the frequency channels affected by persistent strong RFI. After this, wideband model visibilities for the flux density calibrators were predicted, and an initial calibration on a subset of frequency channels (19,000–20,000) was performed to identify any malfunctioning antennas and baselines. For 3C 286 and 3C 138, we used models based on `Perley-Butler 2017` (Perley & Butler 2017). For PKS 1939-638, the model based on `Stevens-Reynolds 2016` was used (Partridge et al. 2016) whereas for PKS 0408-658 a model with $S_{1284\,\mathrm{MHz}} = 17.066$ Jy and $\alpha = -1.179$ was used. Next, the pipeline proceeded to calibrate the entire band, and performed RFI flagging using `tfcrop` and `rflag` in CASA. The delay, bandpass, and temporal complex gain calibration solutions were applied to the target source visibilities.

After calibration, the spectral line and wideband continuum imaging processes diverge. For spectral line or cube imaging, we split the continuous band of 30,720 frequency channels into 15 spectral windows (SPWs) labeled SPW0 to SPW14 (see Table 1). To ensure that no spectral features at the edge of any SPW are lost, the adjacent SPWs have an overlap of ∼7 MHz (256 channels). The measurement sets for these SPWs are then processed for continuum imaging with self-calibration and cube imaging. For each SPW, a continuum data set is generated by flagging RFI-affected frequency ranges and averaging data in frequency by 32 channels to reduce the data volume. This is then imaged using `robust=0` weighting and `w-projection` algorithm with 128 planes as the gridding algorithm in combination with `Multi-scale Multi-term Multi-frequency synthesis` (`MTMFS`) for deconvolution, with nterms = 1 and four pixel scales (0, 2, 3, and 5) to model the extended emission (Rau & Cornwell 2011). Imaging masks were appropriately adjusted using the `Python Blob Detection and Source Finder` (`PyBDSF`[20]; Mohan & Rafferty 2015) between major cycles during imaging and self-calibration runs. This ensured that at any stage the artifacts in the vicinity of bright sources are excluded from the CLEANing process and the source model. The relevant details of how this is achieved through `PyBDSF` are presented in Section 3. Here, we started with high source detection thresholds and gradually reduced these as the imaging progresses through major cycles and self-calibration runs. Overall, the pipeline performed three rounds of phase-only and one round of amplitude and phase self-calibration. The final 6k × 6k continuum images with a pixel size of 2″ have a span of 3.°3 for all SPWs, and have been CLEANed down to three times the local rms noise based on a `PyBDSF` mask.

For cube imaging of an SPW, the self-calibration solutions obtained from the continuum imaging are applied to the line data set, and continuum subtraction is performed using the model, i.e., CLEAN components obtained from the last round of self-calibration. The continuum subtracted visibilities are then inverted to obtain spectral line cubes, which may then be deconvolved for line emission (for example, see Boettcher et al. 2021; Maina et al. 2022). The wideband continuum imaging utilizing full *L*-band bandwidth would require the `w-projection` algorithm in combination with `MTMFS` for deconvolution, but with nterms = 2 (see Wagenveld et al. 2023).

In this paper, we focus on continuum images at 1006.0 and 1380.9 MHz from the spectral line processing of SPW2 and SPW9. For 60.2 MHz bandwidth, 59 antennas and 56 mins of integration, the theoretical rms noise for `robust=0` weighting of visibilities are 22 μJy beam^{-1} (SPW2) and 19 μJy beam^{-1} (SPW9). We use SPW9 images, which are close to the observing frequency of NVSS, to verify the astrometry and flux density scales of MALS. For the latter, we make the reasonable assumption that the flux variability due to intrinsic source properties or interstellar scintillations is not a significant factor at 1.4 GHz (see also Section 5.3). The SPW2 images at the low-frequency (1006.0 MHz) end of the *L* band are used to measure spectral indices of the sources. Note that we prefer SPW2 over SPW0 and SPW1 for relatively lower RFI and avoiding additional complications due to *L*-band roll-off. As previously mentioned, the processes presented in this paper lay the foundation for subsequent *L*- and *UHF*-band data releases corresponding to narrowband (i.e., SPW specific) data products.

3. Image Analysis and Catalogs

3.1. Noise Variations in Raw Images

We used `PyBDSF` to generate radio source catalogs from SPW2 and SPW9 images. In general, the brightest sources in radio images are often associated with artifacts and raise the rms noise in the vicinity above the theoretically expected value. For reliable detection of sources, `PyBDSF` tackles such noise variations by generating rms maps using a sliding box of adjustable dimensions, i.e., smaller near brighter sources and vice versa. The intermediate rms values in the map are then obtained by interpolating between the measurements. We performed source finding on "raw," i.e., primary beam-uncorrected images obtained from `ARTIP` and use noise properties derived from the rms maps to quantify the impact of bright sources in the field of view. Note that the noise

[20] `PyBDSF version 1.10.1.`

Table 2
PyBDSF Parameters for Catalog Generation

Parameter	Value
adaptive_rms_box	True
adaptive_thresh	100.0
rms_box	(150, 30)
rms_box_bright	None
thresh_isl	3.0
thresh_pix	5.0
thresh	None
atrous_do	True
atrous_orig_isl	True
atrous_jmax	3
group_by_isl	True

properties of primary beam-corrected images and the Stokes-*I* catalogs are presented in Section 3.2. Additionally, we also identify 50 representative pointings—discussed at the end of this section—from the sample. We subject SPW9 images of this representative subset to visual inspection to closely track the possible sources of errors and optimize the PyBDSF input parameters.

The key PyBDSF input parameters are summarized in Table 2. The remaining input parameters were set to their default values, the details of which can be found in the PyBDSF documentation (Mohan & Rafferty 2015). We set adaptive_rms_box = True and adaptive_thresh = 100.0 to allow PyBDSF to estimate rms and mean using a smaller box close to bright sources detected at signal-to-noise ratio (S/N) > 100. This is based on the visual inspection of SPW9 images from 50 representative pointings, which revealed significant artifacts around sources brighter than $>100\sigma$, where σ represents the local rms noise. We adopted default values of (i) thresh_isl = 3σ as the threshold to identify the boundary of the island for fitting the radio emission, and (ii) thresh_pix = 5σ as the threshold to detect sources. Although, we set the source detection threshold, i.e., thresh_pix to 5σ, the choice of thresh = None, implied that in general a variable threshold for thresh_pix based on the false detection rate algorithm is used (Hopkins et al. 2002). The value of 5σ for thresh_pix is used only when the number of false pixels is <10% of the estimated number of true pixels.

We note that PyBDSF runs with the default rms_box parameter resulted in box sizes as large as ∼900 pixels in a few cases and ∼600 pixels in the remaining. Such large boxes over-smoothed the internally calculated rms maps and resulted in detections of imaging artifacts as real sources. Therefore, we experimented with a range of tuples corresponding to rms_box and rms_box_bright to define the box and step sizes to be used in general and close to bright sources. The tuple rms_box = (150, 30) was found to minimize the number of such artifacts getting fitted. This is also the value adopted by RACS to obtain optimal results (Hale et al. 2021). We found that setting rms_box to significantly smaller values than this results in omission of fainter sources in the vicinity of bright sources. Also, we set rms_box_bright = None. This implies that we rely on the internal machinery of PyBDSF to determine the suitable box and step sizes in the vicinity of bright sources. We verified that the resultant box and step sizes were significantly smaller than rms_box, and the approach performed better compared to when rms_box_bright was fixed to any specific value smaller than rms_box.

MeerKAT has excellent surface brightness sensitivity to detect large-scale extended radio emission. Therefore, for better modeling of extended emission, we set atrous_do = True to turn on the wavelet decomposition module with a maximum of three wavelet scales (atrous_jmax = 3). Note that we set atrous_orig_isl = True, to ensure that wavelet Gaussians lie within the islands determined using the original image, i.e., prior to any wavelet decomposition. Finally, we also set group_by_isl = True to allow PyBDSF to group all Gaussians within an island into a single source.

We define two rms measurements using the rms maps from "raw," i.e., primary beam-uncorrected continuum images. We measure σ_1 and σ_2 as median rms values using annular rings of 32 pixels wide, at diameters of one and two times the primary beam FWHM. These values, i.e., σ_1^{spw9} and σ_2^{spw9} for SPW9 images are provided in Appendix A, and plotted in the top panels of Figure 2 as a function of peak flux density of the brightest source in the field. Note that for 318/391 pointings, hereafter referred to as belonging to Class-A (see column 6 of Table A1), the radio source at the pointing center is indeed the brightest source in the SPW9 image. However, for 73/391 (∼19%) pointings, serendipitously, an off-axis source happens to be brighter than the central source. Hereafter, we refer to these pointings as Class-B. In Figure 2, the points for Class-B pointings are color coded with respect to the distance of the brightest source from the pointing center.

For clarity, in Figure 2 we have omitted three and four pointings with rms > 100 μJy beam^{-1} and 200 μJy beam^{-1} for σ_1^{spw9} and σ_1^{spw2}, respectively. As discussed below, since σ_1 is typically larger than σ_2, for σ_2^{spw9} and σ_2^{spw2} these omissions in the left panels of Figure 2 translate to the exclusion of one and three of these pointings, respectively, in the right panels. In terms of abovementioned classes for σ_1^{spw9}, two of the three outliers with σ_1^{spw9} = 111 μJy beam^{-1} and 138 μJy beam^{-1} correspond to Class-A pointings with very strong central radio sources with peak flux densities of 11.9 Jy beam^{-1} and 2.81 Jy beam^{-1}, respectively. Interestingly, the third outlier with σ_1^{spw9} = 380 μJy beam^{-1} is a Class-B pointing with an off-axis (distance ∼0.°6) source of 1.1 Jy beam^{-1}.

Overall, Figure 2 clearly demonstrates that both σ_1^{spw9} and σ_2^{spw9} are correlated with the brightness of the central source. The increase is steeper, as is implied by the trend for σ_1^{spw9}, in the inner regions of the primary beam. Overall, the median σ_2^{spw9} is only ∼15% higher than the expected theoretical value, but the same difference for σ_1^{spw9} is ∼40%. The dominant role of the central source in this context is further demonstrated in the bottom panels of Figure 2 showing rms noise for SPW2. As expected, on average the central radio source is brighter in SPW2 at lower frequency (1006.0 MHz). Consequently, σ_1^{spw2} increases even more rapidly and is about 60% higher compared to the theoretical rms noise. In comparison, the value of σ_2^{spw2} is barely affected.

The brightness of a source and its location within the primary beam can elevate the rms noise in the field through a variety of effects. In particular, in the case of bright off-axis sources (Class-B pointings) the direction-dependent effects through pointing errors can be the dominant factor. In order to closely track the possible sources of errors, we subdivide Class-A into four subclasses (A.1–A.4) based on the quartiles partitioning the peak flux density range (0.08–11.87 Jy beam^{-1}) of the central source in SPW9 images. The peak flux density ranges for these are as follows:

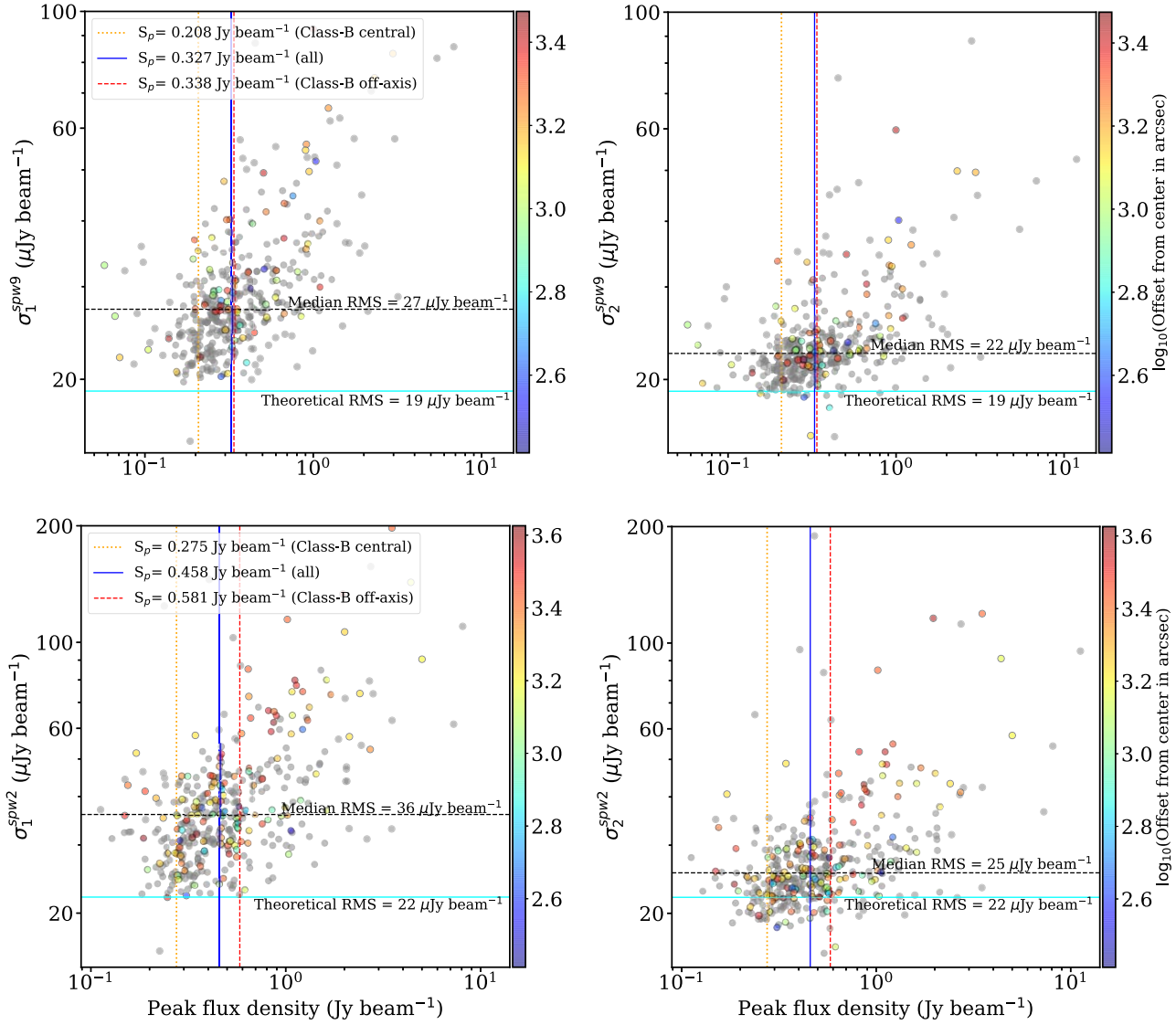

Figure 2. The rms measured at 1 and 2 times the primary beam FWHM, i.e., σ_1 (left panels) and σ_2 (right panels), respectively, as a function of peak flux density (S_p) of the brightest source in primary beam-uncorrected SPW9 (top panels) and SPW2 (bottom panels) images. In the cases for which an off-axis source is brighter than the central radio source (i.e., Class-B pointings), the points have been color coded with respect to the distance of the source from the pointing center. In each panel, the three vertical lines from left to right mark median flux densities for (i) central source in Class-B, (ii) central source in all (391), and (iii) off-axis source in Class-B pointings. Horizontal dashed lines mark theoretical and observed rms noise values. For clarity, in the top- and bottom-left panels, three and four points with σ_1 greater than 100 and 200 μJy beam^{-1} have been omitted, respectively.

A.1 = 0.08–0.23 Jy beam^{-1}, A.2 = 0.23–0.32 Jy beam^{-1}, A.3 = 0.32–0.49 Jy beam^{-1}, and A.4 = 0.49–11.87 Jy beam^{-1}. The effect of the central source in raising the rms floor is apparent from Figures 3 and 4. The cumulative distribution functions (CDFs) of rms noise pixels (Figure 3), especially the bottom two panels, exhibit an increase in overall rms of the image as the peak flux density of the brightest source in the image increases. From Class-A.1 to A.4 and B, the distribution starts shifting toward the right and becomes progressively flatter, indicating an increase in the fraction of noisy pixels contributed by brighter sources. This is also corroborated by the median-stacked rms maps presented in Figure 4 showing that for classes A.4 and B the effect extends well beyond the beam FWHM. Note that for class B, we have not oriented images at position angles of bright off-axis source; hence, the impact of the off-axis sources is smeared out.

Finally, for rigorous artifact analysis involving visual inspection to closely track various systematic errors and the purity of the catalog in Section 3.3, we identify 50 representative pointings, 10 from each class spanning the typical range of CDF profiles. These pointings were picked without any visual examination and can be recognized through the dashed–dotted lines in Figure 3 and "_R" in column 6 of Table A1.

3.2. Primary Beam Correction and Stokes-I Catalog

[21]The "raw" images from `ARTIP` are not corrected for the effects of the primary beam pattern of MeerKAT. Mauch et al. (2020) demonstrated that the Stokes-*I* primary beam response of MeerKAT from holographic measurements is well approximated by a cosine-tapered field illumination function. We use the publicly available `katbeam`[21] module (version 0.1) to generate the primary beam responses at the reference frequencies of SPW-based images (see Table 1) and apply

[21] https://github.com/ska-sa/katbeam

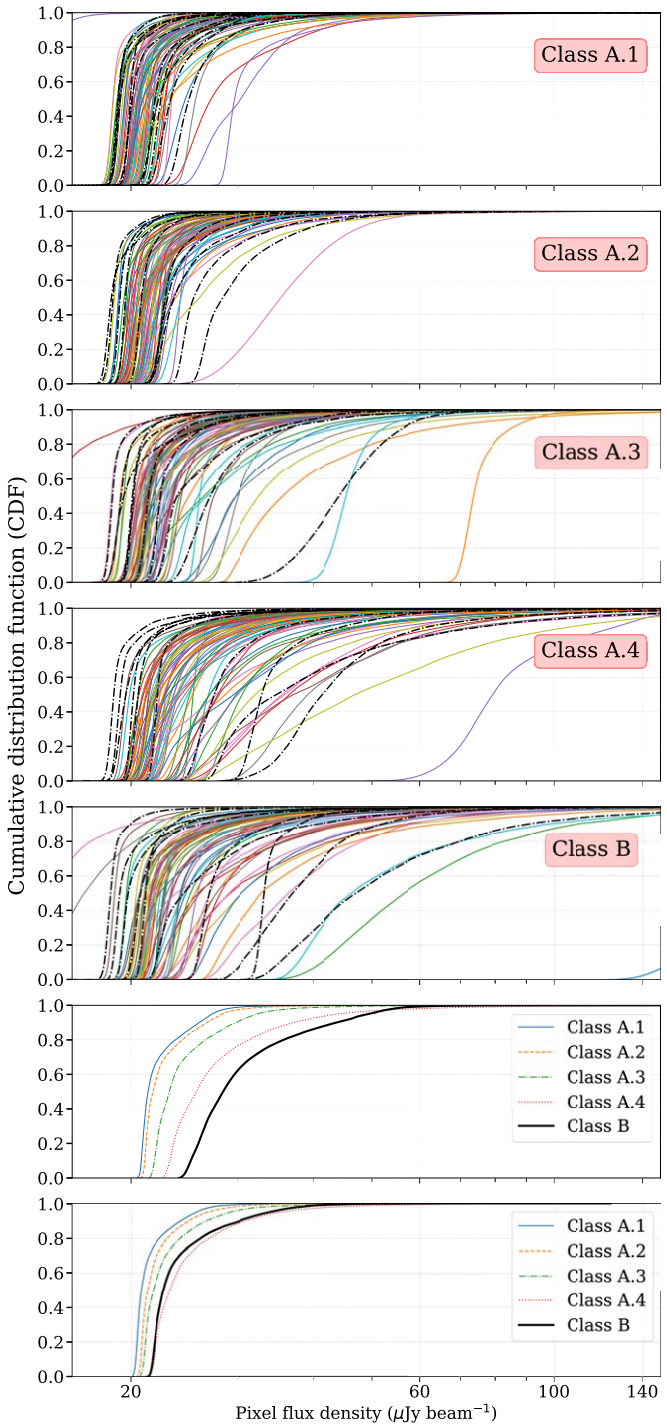

Figure 3. Cumulative distribution function (CDF) of pixels in the rms maps of 391 pointings, arranged as per Class-A.1 to Class-A.4, and Class-B (top five panels). The profiles from mean- and median-stacked rms images are shown in the bottom two panels. The dashed–dotted lines in the top five panels correspond to 'representative' pointings selected (see the end of Section 3.1). The curves with lowest rms for Class-A.1, -A.3, and -B correspond to four pointings with double the integration time (see the text for details).

these to "raw" images using the CASA task `impbcor` to recover intrinsic source properties.

The primary beam gain is often poorly determined in the outermost regions. Therefore, the usual practice is to cut off the primary beam normalization at 0.2. However, we adopted a `cut_off` value of 0.05, which resulted in primary beam-corrected SPW9 and SPW2 images of extent $\sim 1\overset{\circ}{.}92$ and $\sim 2\overset{\circ}{.}73$ in diameter, respectively. Figures 5 and 6 show two SPW9 images as examples—one of these is from Class-A.1 and the another one is from Class-A.3. The latter is chosen such that the peak flux density of the central source is close to the median value (327 mJy beam^{-1}) for the sample. The increase in rms noise away from the pointing center due to the primary beam correction is apparent in both the images. Also, the radio sources are detected right up to the edge of the images.

We note that a primary beam `cut_off` value of 0.2 will yield images of extent (diameter) $\sim 2\overset{\circ}{.}12$ (SPW2) and $\sim 1\overset{\circ}{.}49$ (SPW9). The choice of lower `cut_off` allows us to detect $\sim$20% additional sources. The comparison of the properties of these radio sources included in the current and future data releases expands the scope for an independent investigation of the frequency-dependent behavior of the primary beam across the *L* and *UHF* bands (for example, see Section 4.3). These sources may also be of interest for various science cases, e.g., absorption line search and radio continuum variability, that do not necessarily require the measurement of absolute flux densities. The reliability of sources detected in the outermost regions of the primary beam is discussed in Section 3.3.

We used `PyBDSF` parameters summarized in Table 2 to generate radio source catalogs from primary beam-corrected SPW2 and SPW9 images. In Section 3.1, we discussed the correspondence between the flux density of the brightest source in the field and noise variations across pointings using "raw" images. We reexamined the appropriateness of the choice of the same `PyBDSF` parameters for primary beam-corrected images. Of particular interest here is the modeling of extended emission associated with radio sources. In Figure 7, we show examples of four radio sources with different morphologies. The individual Gaussian components fitted to model the radio emission are also shown. In panels A, C, and D, the radio source is modeled using multiple components (magenta ellipses), all of which are then grouped to form a single source (thick orange ellipse). Such sources are labeled by `PyBDSF` as "M"-type implying a single source fitted with multiple Gaussian components. A single source fitted with a single component is labeled as "S" (panel (B) of Figure 7). Note that due to the choice of `PyBDSF` parameter, `group_by_isl = True`, there are no 'C' type sources (i.e., multiple sources within an island) in the MALS catalogs.

We used "Source list" and "Gaussian list" catalogs from `PyBDSF` to generate final MALS radio continuum catalogs for both SPW2 and SPW9. Table 3 lists all of the columns and also provides a short description of each column. Columns 1–16 provide overall details of the pointing in which the source is detected. This includes `Pointing_id` based on the position of the central source in NVSS or SUMSS, the observing band and date of observation, the version of the primary beam model, the details of flux density calibration, the restoring beam, and various rms noise estimates, i.e., `Sigma_1`, `Sigma_2` and `Sigma_20`. All of these details are common to all of the sources detected in a pointing. Unlike `Sigma_1` and `Sigma_2`, `Sigma_20` is based on the primary beam-corrected images. Further, while `Sigma_1` and `Sigma_2` provide rms at one and two times the beam FWHM, `Sigma_20` is representative of rms noise coverage in the central region of the images (see Wagenveld et al. 2023, for details). Nonetheless, the three noise estimates are correlated. Typically (median), `Sigma_20` is 1.8 and 2.2 times `Sigma_1`

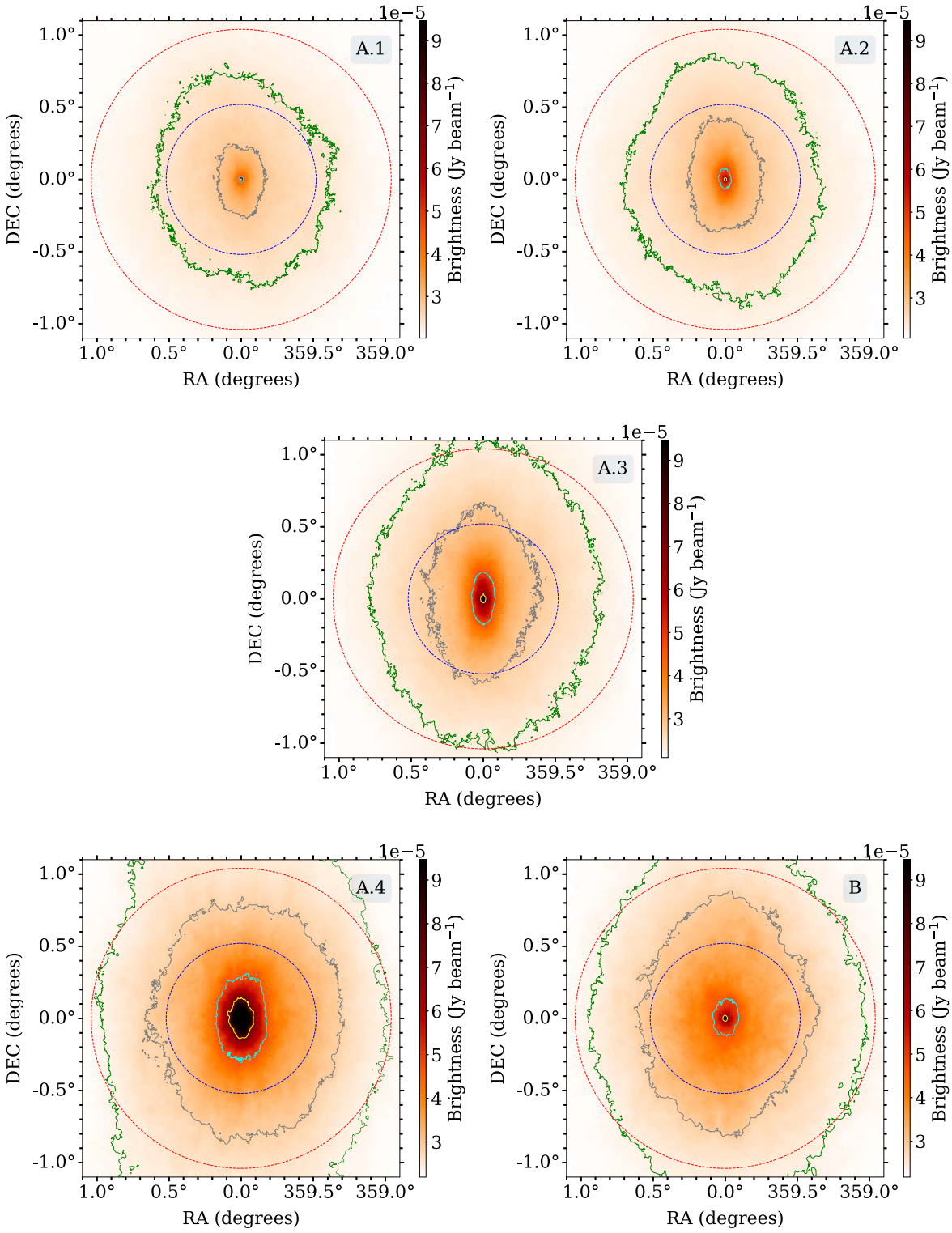

Figure 4. Median-stacked rms maps for various pointing classes (indicated in the top-right labels) based on primary beam-uncorrected SPW9 images. The blue and red dotted circles represent diameters of one and two times the primary beam FWHM where σ_1 and σ_2 are measured. The color-bar range is saturated at the peak intensity (95 μJy beam^{-1}) of stacked Class-A.1 map. The contours correspond to 25% (green), 30% (gray), 50% (cyan), and 80% (yellow) of the same peak intensity.

and `Sigma_2`, respectively. Note that this paper focuses only on sources detected in the SPW2 and SPW9 continuum images but the catalog columns have been defined to support all subsequent releases based on *L*- and *UHF*-band continuum images for individual SPWs or the entire wideband (see column 9; i.e., `SPW_id`).

The properties of individual sources are provided in columns 17–67. Since rms noise and systematic errors depend on distance from the pointing center and the proximity to a bright radio source, we provide `Distance_pointing`, the distance from the pointing center (column 17), and `Distance_NN`, the distance from the nearest neighbor (column 18). The `PyBDSF`

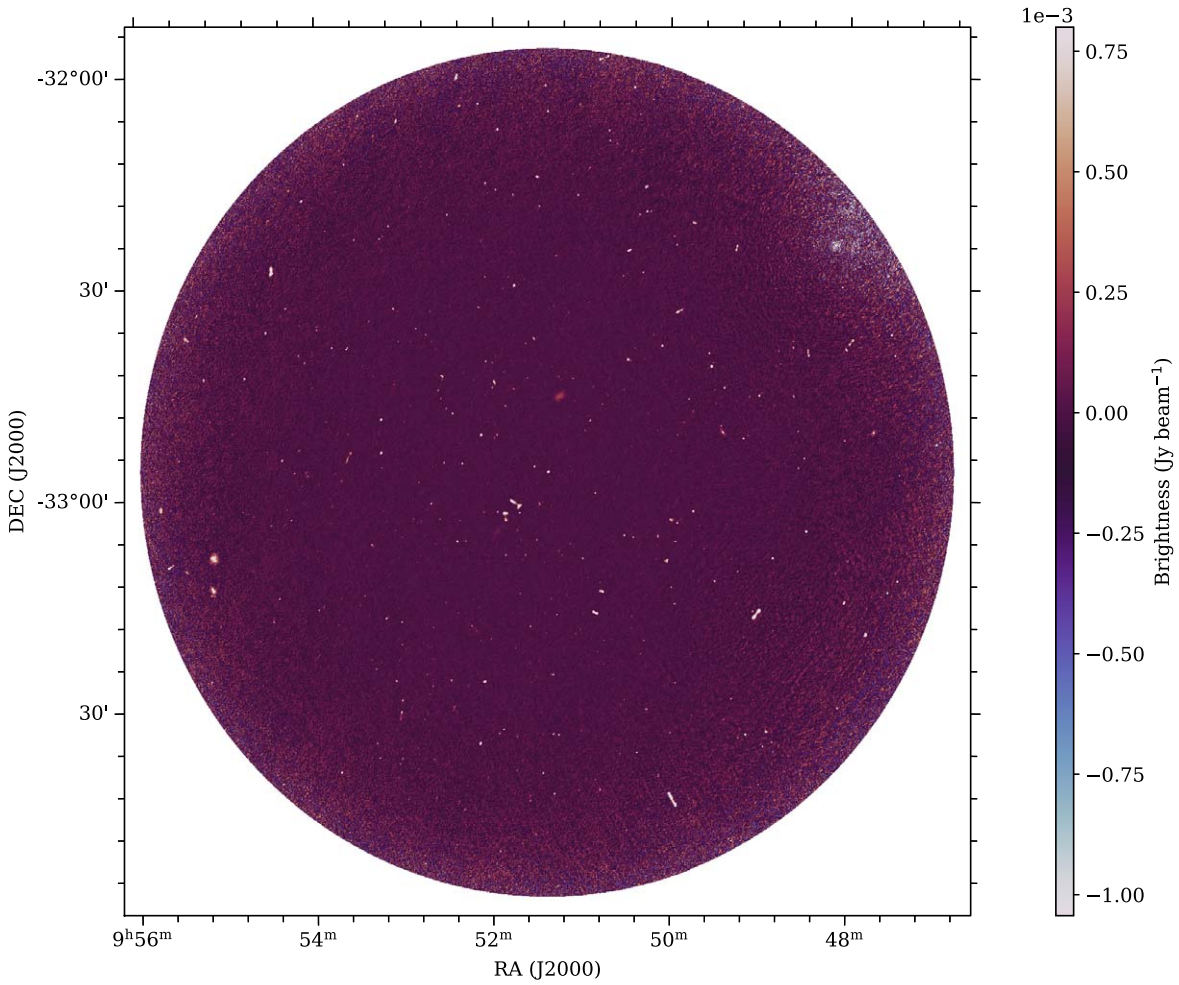

Figure 5. MeerKAT primary beam-corrected *L*-band SPW9 image centered on the radio source J095123.18-325554.8 (Class-A.1; $S_p \sim 153.0$ mJy beam^{-1}), with `robust=0` weighting. The rms in the vicinity of the central source is 40 μJy beam^{-1}, and the restoring beam is $7\farcs7 \times 6\farcs2$ with a position angle of $-16°$. The dynamic range is ∼3800.

label `S_code` = "S" or "M" discussed above is provided in column 19. The number of Gaussian components (`N_Gauss`) fitted to the source and the maximum separation between the components (`Maxsep_Gauss`) are provided in columns 20 and 21, respectively. The angular sizes, positions, and flux densities of sources are provided in columns 22–56, and the details of individual components are provided in columns 68–86. Column 86 provides unique Gaussian component identifiers. Columns 57–64 provide spectral index measurements. Columns 65 and 67 are concerned with the reliability of source detection and its morphology, respectively. We note that columns 19, 22–42, 44, 48–55, and 68–85 are direct outputs from the `PyBDSF` runs. The remaining columns are based on additional analysis discussed in the subsequent Sections of this paper.

In total, we detect 240,321 sources consisting of 285,209 Gaussian components from 391 primary beam-corrected SPW9 images at 1380.9 MHz, of which 215,328 and 24,993 are of type (`S_code`) "S" and "M," respectively. On average (mean), we detect 629 and 551 sources in 318 and 73 pointings of type Class-A and B, respectively. The median dynamic ranges defined as the ratio of peak flux density of the brightest source and σ_1^{spw9} achieved at SPW9 are 11,800 (Class-A) and 12,300 (Class-B). In comparison, the total number of sources in SPW2 images at 1006.0 MHz is 495,325, with 586,290 Gaussian components. Of these 441,988 and 53,337 are of type "S" and "M," respectively. The larger number of sources in SPW2 images can be attributed to larger sky coverage (total 2289 deg^2) compared to that of SPW9 images (total 1132 deg^2). Using a matching radius of 6″, 205,435 sources were found to be common between SPW2 and SPW9.

The catalogs and images for SPW2 and SPW9 can be accessed at https://mals.iucaa.in. Each MALS data release will identify a "reference" SPW, and columns 57–67 based on information from multiple SPWs will be filled only in the 'reference' SPW catalog. Since a larger number of sources are detected in SPW2, the reference SPW adopted for MALS DR1 is SPW2.

From https://mals.iucaa.in, users can download the source catalog (i.e., columns 1–67) of 205,435 sources common between SPW2 and SPW9, as well as 240,321 (495,325) sources corresponding to SPW9 (SPW2). The Gaussian component catalogs are also available. These consist of columns 1 (`Source_name`), 20 (`N_Gauss`), and 68–85 (Gaussian parameters) from Table 3. In Tables B1 and B2 (Appendix B), we present the first few rows of the source and

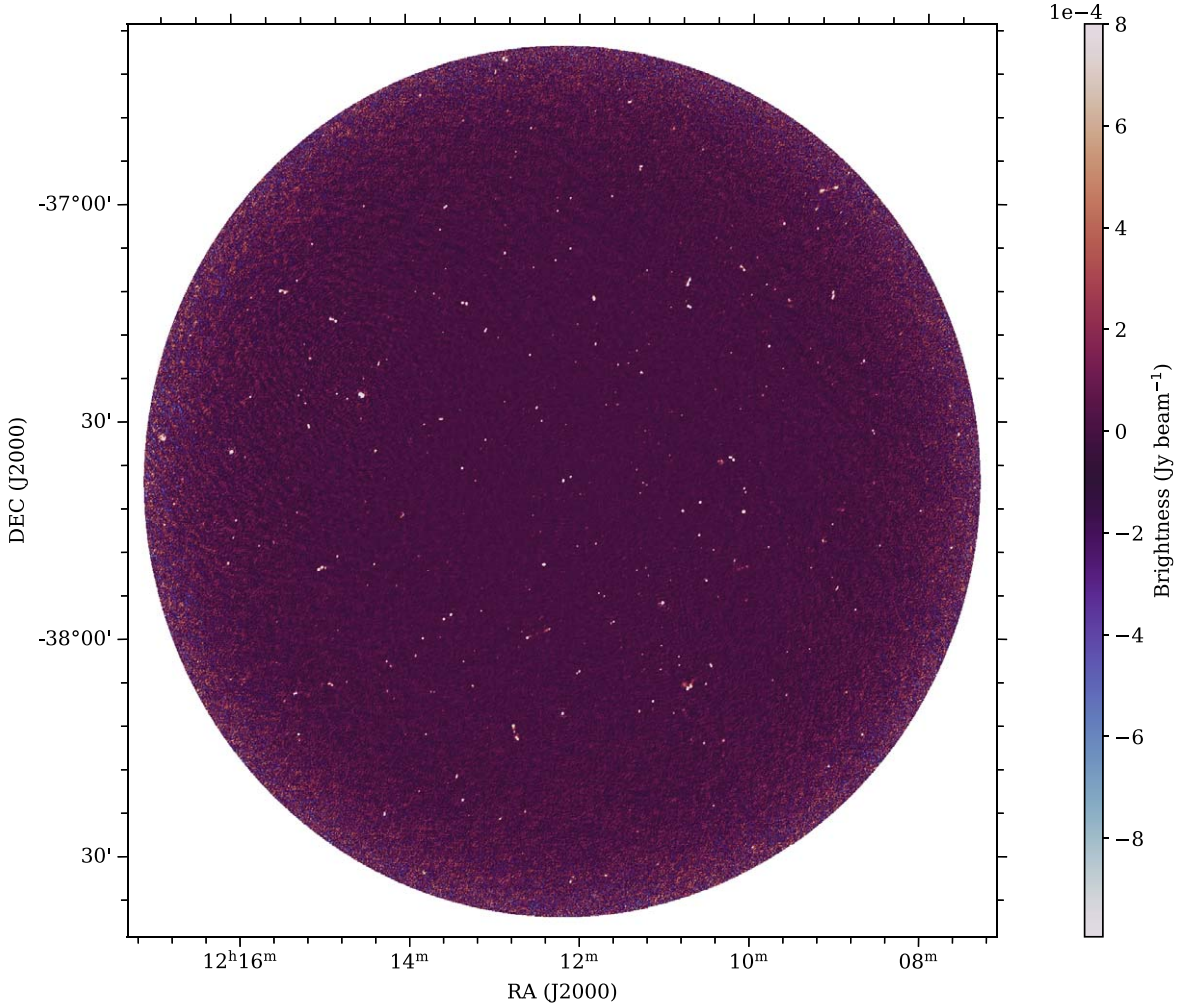

Figure 6. MeerKAT primary beam-corrected *L*-band image centered on the radio source J121211.89-373826.9 (Class-A.3; $S_p \sim 351.9$ mJy beam^{-1}), with `robust=0` weighting. The rms in the vicinity of the central source is 50 μJy beam^{-1}, and the restoring beam is $9\farcs0 \times 6\farcs5$ with a position angle of $-24°$. The dynamic range is ∼7000.

Gaussian component catalogs, respectively. Note that in the current release, columns 3, 57, 58, 65, and 67 in the source catalog are empty. Column 3 is relevant only for the *UHF* band, whereas 57 and 58 are for wideband images, hence not relevant for DR1 and included only for the completeness. Columns 65 and 67 require analysis involving images from all of the other SPWs, and hence will be provided in a future release.

3.3. Purity of the Catalog

Catalogs as output from `PyBDSF` are contaminated by spurious sources, which could either be due to statistical noise fluctuations or due to bright sidelobes around strong sources. To get a handle on these false detections, we followed the simple procedure of inverting (multiply by −1) an image and then running source finding on it with the same set of threshold parameters, rms, and (inverted) mean maps as were used for the actual catalog generation. This method is based on the idea that statistical noise fluctuations are symmetric around the mean and therefore sources detected in the 'negative' images due to noise peaks will provide an estimate of the false sources detected in our actual catalogs (e.g., Hurley-Walker et al. 2017; Intema et al. 2017; Hale et al. 2021). In the vicinity of bright sources, the systematic errors will dominate and the sources detected in the 'negative' image may represent an upper limit on the level of spurious sources.

From 391 SPW9 pointings, we detect 2548 'negative' sources, which is merely ∼1% of the sources in the DR1 catalog. The cumulative distribution of artifacts shows a steep dependence on S/N, which saturates near S/N ≈ 8. About 95% of the artifacts lie at S/N < 8. Therefore, we consider S/N = 8 as a reasonable cutoff to define samples for various analysis. Figure 8 shows the fraction of these artifacts as a function of distance from the pointing center in three S/N bins. As expected, the fraction is larger near the pointing center and the edges of the beams (see shaded regions in Figure 8). We advise caution in using low S/N sources belonging to the shaded region by applying filters corresponding to `Distance_pointing` parameter. Outside the shaded regions, the distribution, even at distances larger than 45′ from the pointing center,[22] is largely uniform and negligible, especially for S/N > 8.

[22] The `cut_off` = 0.2 usually used for primary beam normalization corresponds to a distance of 45′ from the pointing center (see Section 3.2).

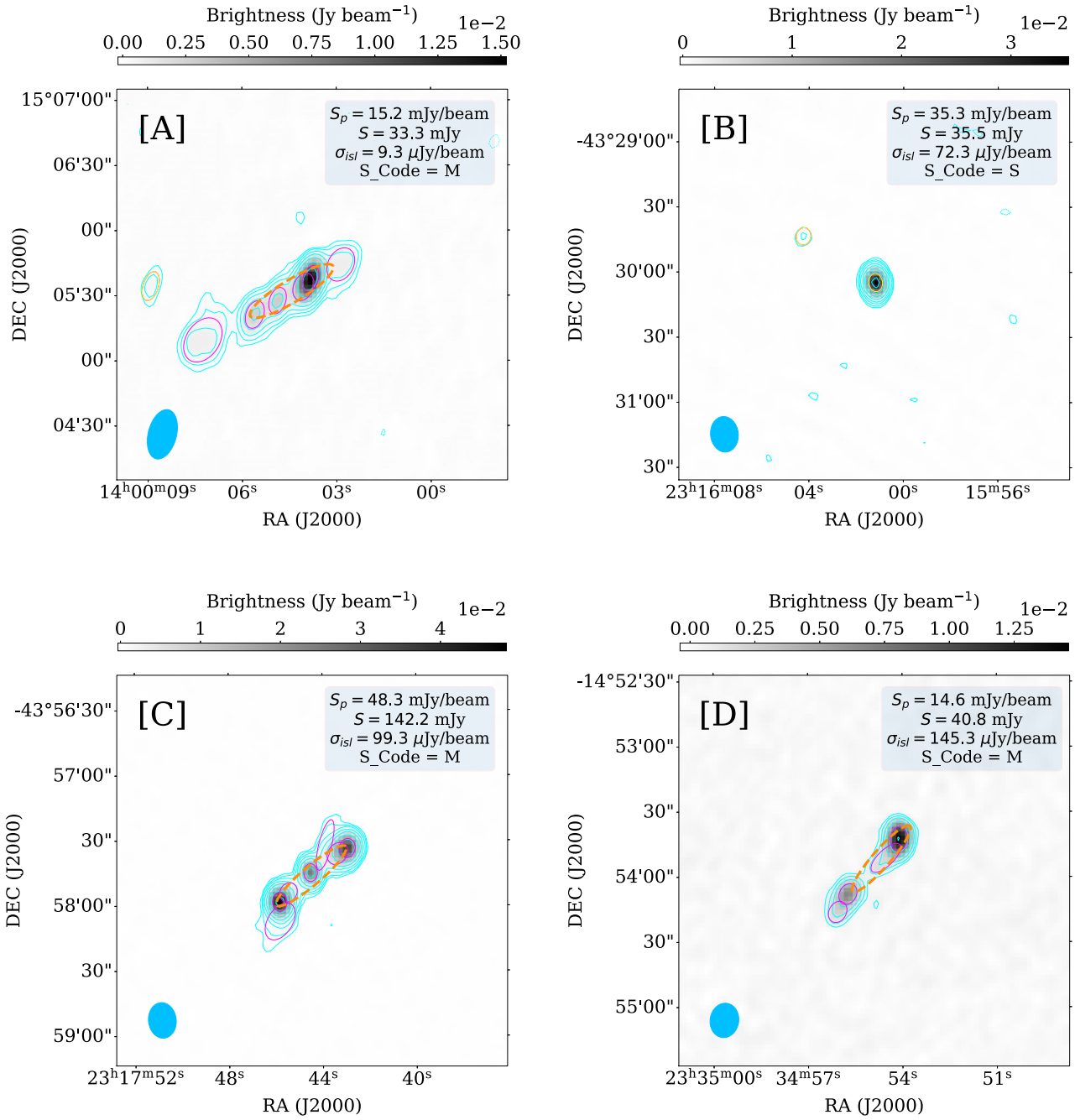

Figure 7. Image cutouts ($3' \times 3'$) exhibiting typical morphology of radio sources detected in primary beam-corrected SPW9 images. The contour levels are shown at $3 \times$ `isl_rms` $\times$ (-1, 1, 2, 4, 8, 16,...) mJy beam^{-1}. The FWHM of major and minor axes of the fit to the source are shown using solid yellow, for `S_Code=S`, and dashed orange ellipse, for `S_Code=M` (see Table 3 for details). The individual Gaussian components fitted—six in A, one in B, seven in C, and four in D—to model the emission are shown as solid magenta ellipses. Note that in panel B, for an `S_Code=S` type source, the yellow ellipse coincides with the magenta ellipse representing the fitted single-Gaussian component. In panels A and B, another unrelated compact source, in a different island, is also detected. The `isl_rms` used for plotting contours in these panels is the average of the two islands. The restoring beams are shown as filled ellipses at the bottom-left corner of the images.

In Figure 9, we show the S/N distribution of residual pixels from primary beam-corrected images for each class of pointings discussed in Section 3.1. The residual image is generated by `PyBDSF` after subtracting all of the fitted source components from an image. Therefore, it should represent only the random background noise, whose S/N distribution is expected to be Gaussian. In each panel, the Y-axis is plotted in `log`-scale to show any deviation from the fitted Gaussian. The dotted gray vertical lines indicate the data range used to fit the plotted Gaussian to the distribution. In the majority of the cases, only marginal deviation from the fit is seen. In cases where there is a significant excess emission toward the positive side (e.g., bottom-right panel in Figure 9), we inspected them visually and found that the dominant fraction of outlier pixels belongs to 'empty islands,' i.e., islands where there is no Gaussian component fitted to the emission because `thresh_pix` is less than 5σ. As an additional check, we also ran `PyBDSF` on these images with an additional parameter

Table 3
Catalog Column Descriptions

Number (1)	Name (2)	Description (3)
1	Source_name	MALS name of the source (JHHMMSS.ss+DDMMSS.s) based on its R.A. and decl. (J2000).
2	Pointing_id	The MALS pointing ID (JHHMMSS.ss ± DDMMSS.s) based on the position (J2000) of the central source in NVSS or SUMSS.
3	Obs_date_U	The date and time (UTC) of the start of *UHF*-band observing block(s) in the format YYYY-MM-DDThh:mm.
4	Obs_date_L	The date and time (UTC) of the start of *L*-band observing block(s) in the format YYYY-MM-DDThh:mm.
5	Obs_band	The observing band: $L = L$ band and $U = UHF$ band.
6	PBeamVersion	The primary beam model (katbeam or plumber) version used for the primary beam correction (see Section 4.3 for details). All of the columns except Total_flux_measured and Total_flux_measured_E in MALS DR1 are based on the katbeam model (see also Flux_correction).
7	Fluxcal	The list of calibrator(s) used for flux density and bandpass calibration of the data set.
8	Fluxscale	The flux density scales used for the flux density calibrators.
9	SPW_id	This defines whether the continuum image is made using an SPW or the entire wideband (WB). The possible values are LWB-WP, LWB-AWP, UWB-WP, UWB-AWP, LSPW_*i*, and USPW_*i*; here *i* goes from 0–14. For example, LWB and UWB imply *L*- and *UHF*-band wideband image, respectively. LSPW_2 and LSPW_9 correspond to SPW2 and SPW9 of the *L* band included in DR1 presented here. WP and AWP identify the imaging algorithm used for wideband imaging. WP: W-Projection algorithm is used to correct for the wide-field effect of noncoplanar baselines (Cornwell et al. 1992), and the primary beam correction is applied after the imaging. AWP: A-term is also included, and the wideband effects of the primary beam are corrected prior to integration in time and frequency for the continuum imaging (Bhatnagar et al. 2013).
10	Ref_freq	The reference frequency (MHz) of the continuum image.
11	Maj_restoring_beam	The major axis (arcseconds) of the restoring beam.
12	Min_restoring_beam	The minor axis (arcseconds) of the restoring beam.
13	PA_restoring_beam	The position angle (degrees) of the restoring beam.
14	Sigma_1	The rms noise (μJy beam^{-1}) measured from primary beam-uncorrected rms image in an annular ring at primary beam FWHM.
15	Sigma_2	The rms noise (μJy beam^{-1}) measured from primary beam-uncorrected rms image in an annular ring at 2 times the primary beam FWHM.
16	Sigma_20	The rms noise (μJy beam^{-1}) at a cumulative fraction of 0.2 of the rms noise distribution of the primary beam-corrected rms image (σ_{20}; see Wagenveld et al. 2023 for details).
17	Distance_pointing	The distance of the source (arcminutes) from the pointing center.
18	Distance_NN	The distance of the source (arcminutes) from the nearest neighbor in the field.
19	S_Code[b]	The PyBDSF code defining the source structure. S = a single source in the island, fitted with a single-Gaussian component. C = a source with other neighbors within the island, fitted with a single-Gaussian component. M = a source fitted with multiple Gaussian components.
20	N_Gauss	The number of Gaussian components fitted to the source.
21	Maxsep_Gauss	The maximum separation (arcseconds) between the Gaussian components. This is set to −1 for "S"-type sources.
22	Maj[b]	The FWHM (arcseconds) of the major axis of the source.
23	Maj_E[b]	The 1σ error on Maj.
24	Min[b]	The FWHM (arcseconds) of the minor axis of the source.
25	Min_E[b]	The 1σ error on Min.
26	PA[b]	The position angle (degrees) of the major axis of the source measured east of north.
27	PA_E[b]	The 1σ error on PA.
28	DC_Maj[b]	The FWHM (arcseconds) of the deconvolved major axis of the source.
29	DC_Maj_E[b]	The 1σ error on DC_Maj.
30	DC_Min[b]	The FWHM (arcseconds) of the deconvolved minor axis of the source.
31	DC_Min_E[b]	The 1σ error on DC_Min.
32	DC_PA[b]	The position angle (degrees) of the deconvolved major axis of the source measured east of north.
33	DC_PA_E[b]	The 1σ error on DC_PA.
34	RA_mean[b]	The R.A. (J2000) of the mean intensity-weighted position of all pixels above the island threshold, measured if source is fitted with multiple Gaussians.
35	RA_mean_E[b]	The 1σ error on RA_mean estimated using Equation 1.
36	DEC_mean[b]	The decl. (J2000) of the mean intensity-weighted position of all pixels above the island threshold, measured if source is fitted with multiple Gaussians.
37	DEC_mean_E[b]	The 1σ error on DEC_mean estimated using Equation 1.
38	RA_max[b]	The R.A. (J2000) of the pixel corresponding to maximum flux density.
39	RA_max_E[b]	The 1σ error on RA_max estimated using Equation 1.
40	DEC_max[b]	The decl. (J2000) of the pixel corresponding to maximum flux density.
41	DEC_max_E[b]	The 1σ error on DEC_max estimated using Equation 1.
42	Total_flux[b]	The total integrated flux density (mJy) of the source based on Gaussian component fits, i.e., corrected for primary beam and wideband effects.
43	Total_flux_E	The 1σ error on Total_flux estimated using Equation 2.
44	Total_flux_E_fit[b]	The fitting error on total flux density to be taken into account to obtain Total_flux_E (see Section 4.2 and Equation 2).

Table 3
(Continued)

Number (1)	Name (2)	Description (3)
45	Total_flux_E_sys	The systematic error to be taken into account to obtain Total_flux_E (see Section 4.2 and Equation 2).
46	Total_flux_measured[c]	The total integrated flux density (mJy) of the source based on alternate primary beam model, i.e., plumber (Section 4.3) obtained by multiplying Total_flux (column 42) and Flux_correction (column 56).
47	Total_flux_measured_E[c]	The 1σ error on Total_flux_measured.
48	Peak_flux[b]	The peak flux density (mJy beam^{-1}) of the source.
49	Peak_flux_E[b]	The 1σ error on Peak_flux.
50	Isl_Total_flux[b]	The total integrated flux density (mJy) of the island in which the source is located.
51	Isl_Total_flux_E[b]	The 1σ error on Isl_Total_flux.
52	Isl_rms[b]	The average background rms noise (mJy beam^{-1}) of the island in which the source is located.
53	Isl_mean[b]	The average background mean value (mJy beam^{-1}) of the island in which the source is located.
54	Resid_Isl_rms[b]	The average residual background rms noise (mJy beam^{-1}) of the island in which the source is located.
55	Resid_Isl_mean[b]	Average residual background mean value (mJy beam^{-1}) of the island in which the source is located.
56	Flux_correction	The factor to be multiplied to flux density measurements and errors to obtain the values corresponding to the plumber beam model (see Section 4.3 and Appendix C).
57	Spectral_index	The spectral index and curvature of the source determined from the wideband MTMFS image. For an extended source, a mean value for the pixels above some threshold in the island is reported (see Section 5.2).
58	Spectral_index_E	The 1σ error on Spectral_index (see Section 5.2).
59	Spectral_index_spwused	The spectral windows used for determining spectral index and curvature using the narrowband multifrequency synthesis (MFS) images. For example, [''L:1~4;7,'' 'U:3~8;12''] implies Total_flux from spectral windows 1–4 and 7 for the *L* band, and 3–8 and 12 for the *UHF* band are used.
60	Spectral_index_spwfit	The spectral index and curvature of the source based on Total_flux from narrowband (i.e., SPW-based) images.
61	Spectral_index_spwfit_E	The 1σ error on Spectral_index_spwfit.
62	Spectral_index_MALS_Lit	The spectral index and curvature based on Total_flux from narrowband images from MALS and measurements from the literature.
63	Spectral_index_MALS_Lit_E	The 1σ error on Spectral_index_MALS_Lit.
64	Spectral_index_Lit	The list of external surveys (e.g., VLASS, TGSS) used. For example, ["TGSS-ADR1," "L:2"], flux densities from TGSS ADR1 and SPW2 of MALS *L* band are used.
65	Real_source	This is a Boolean (True or False) indicating whether a source is a real astrophysical source or an artifact.
66	Resolved	This is a Boolean (True or False) indicating whether a source is resolved based on the reliability envelope method (see Figure 10).
67	Source_linked	This is a list of Source_name, i.e., other MALS sources to which the source may be linked to. This accounts for the linkages missed by grouping mechanism of PyBDSF.
68	G_RA[b]	The R.A. (J2000) of maximum intensity of the Gaussian component.
69	G_RA_E[b]	The 1σ error on G_RA.
70	G_DEC[b]	The decl. (J2000) of maximum intensity of the Gaussian component.
71	G_DEC_E[b]	The 1σ error on G_DEC.
72	G_Peak_flux[b]	The measured peak flux density (mJy beam^{-1}) of the Gaussian component (using PyBDSF).
73	G_Peak_flux_E[b]	The 1σ error on G_Peak_flux.
74	G_Maj[b]	The FWHM (arcseconds) of the major axis of the Gaussian component.
75	G_Maj_E[b]	The 1σ error on G_Maj.
76	G_Min[b]	The FWHM (arcseconds) of the minor axis of the Gaussian component.
77	G_Min_E[b]	The 1σ error on G_Min.
78	G_PA[b]	The position angle (degrees) of the major axis of the Gaussian component.
79	G_PA_E[b]	The 1σ error on G_PA.
80	G_DC_Maj[b]	The FWHM (arcseconds) of the deconvolved major axis of the Gaussian component.
81	G_DC_Maj_E[b]	The 1σ error on G_DC_Maj.
82	G_DC_Min[b]	The FWHM (arcseconds) of the deconvolved minor axis of the Gaussian component.
83	G_DC_Min_E[b]	The 1σ error on G_DC_Min.
84	G_DC_PA[b]	The position angle (degrees) of the deconvolved major axis of the Gaussian component.
85	G_DC_PA_E[b]	The 1σ error on G_DC_PA.
86	G_id	A unique Gaussian component identifier.

Notes.
[a] This is unique only for a combination of POINTING_ID and SPW_ID.
[b] This is direct output from PyBDSF.
[c] Columns 46 and 47 are based on the plumber beam model. All of the other flux density measurements provided in the catalog are based on the katbeam model. The measurements corresponding to the plumber model can be obtained using Flux_correction provided in column 56.

incl_empty=True, which includes the empty islands in the source (''srl'') catalog. In addition to this, we also found excess positive pixels due to residual emission left during modeling of complex "M"-type sources as well as due to random positive noise peaks, although the contribution from these two factors is not always appreciable.

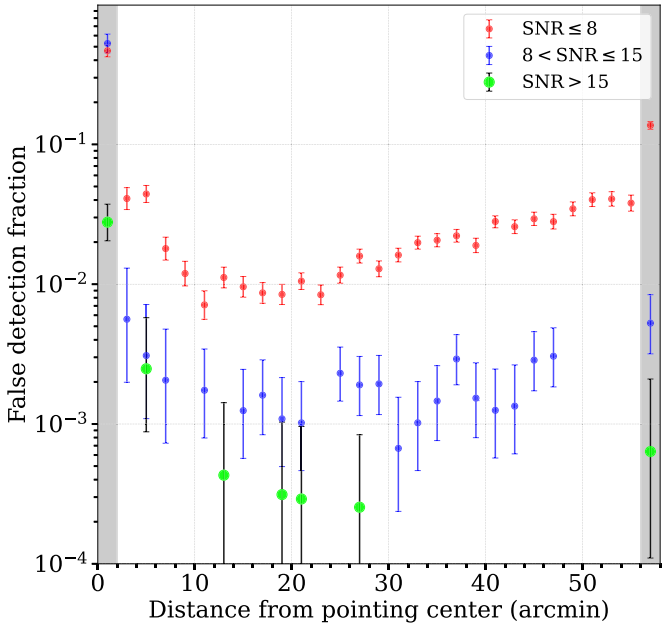

Figure 8. The fraction of "negative" sources with respect to the sources from actual images as a function of distance in three different S/N bins. The bin size is 2′. Error bars denote 1σ Poissonian uncertainties. The shaded portion marks regions with a high false detection rate. Note the absence of artifacts with S/N > 15 in most of the bins, except near the center and at the edges.

The negative pixels with S/N $\leqslant -5$ can have three different origins: improper modeling of source emission resulting in negative pixels in the residual image after component subtraction, random negative noise peaks, and strong negative peaks near bright sources due to statistical errors related to calibration. The first case affects the measurement of flux densities in poorly modeled (mostly "M"-type) sources. Considering only ∼10% of sources in our catalog are of "M"-type, this should not affect our analysis significantly. Still, we recommend the user to compare the ``Isl_Total_flux'' and ``Total_flux'' parameters to judge the quality of Gaussian component fits. The latter two causes of 'bright' negative pixels are particularly responsible for contamination of the catalogs through the generation of false sources discussed above and can be eliminated from the analysis by considering sources detected at >8σ.

4. Stokes-*I* Properties and Accuracy

We examine the astrometric and flux density accuracy of MALS catalogs by comparing them with NVSS and FIRST at 1.4 GHz. FIRST is more sensitive and has ∼10 times better spatial resolution than NVSS (see Section 1). But only 119 MALS pointing centers are covered in FIRST. In comparison, a total of 348 out of 391 MALS pointings overlap with the NVSS sky coverage ($\delta \gtrsim -40°$). Therefore, for optimal utilization of the available data, we split the analysis into *three* parts as following. In the *first* part involving MALS and NVSS, we consider only the targets at the pointing center. These are detected at very high S/N (>5000), are largely compact, and are unaffected by errors from the primary beam correction. In this part, we also include 64 out of 88 gain calibrators observed as part of MALS observations that are common with NVSS. Like central targets, all of these are also bright (>1 Jy at 1.4 GHz) and at the pointing center.

As previously mentioned, four out of 391 MALS pointings, i.e., J1133+0040, J1142−2633, J1144−1455, and J2339−5523, were observed twice. In the *second* part involving only MALS, we compare the properties of all of the sources from two observing runs to obtain an estimate of systematic errors in astrometry and flux densities. The assumption here is that the majority of these sources are intrinsically nonvariable within the timescale of observations: ∼8 days for J2339−5523 and ∼14 days for the remaining three.

In the *third* part, we extend the analysis to off-axis sources detected at S/N >8 in MALS SPW9 images. In order to minimize additional uncertainties due to resolution differences between these surveys, we limit the comparison to isolated and compact sources in MALS. For isolation, we consider SPW9 sources with no neighbor within 60″ radius, i.e., Distance_NN >60″. The adopted isolation radius is about three times the NVSS resolution (σ). It is sufficiently large to exclude sources that are simple in NVSS but split into multiple sources or components in MALS. Such sources will have systematically larger positional and flux density offsets. The issues arising from differing surface brightness sensitivities of the surveys can be controlled by selecting only compact sources in MALS. For this we retain only sources with S_Code = ``S'' and apply the widely used procedure of deriving an S/N-dependent "reliability" envelope encompassing 95% of these sources with total-to-peak flux density ratio < 1 (Figure 10; Bondi et al. 2008; Shimwell et al. 2017; Smolčić et al. 2017b; Hale et al. 2021). The derived envelope, i.e., fit to "×" in Figure 10 is then reflected on the other side, and all of the sources outside the envelope are rejected. Note that the increased scatter in Figure 10 at low S/Ns may be due to the elevated gain errors and noise (for example, see Figure 7 of Shimwell et al. 2017). Overall, for MALS-NVSS comparison, we obtain a sample of 15,834 compact sources from 22,425 isolated SPW9 sources (S/N >8; S_Code=``S''). Next, we use the envelope method to further reject sources that may be compact in MALS but resolved in FIRST to obtain a sample of 7795 sources suitable for MALS-FIRST comparison.

In passing, we note that 43/391 (∼11%) pointings with $-72° < \delta < -40°$ do not overlap with NVSS and FIRST. Therefore, these are not included in the astrometric and flux-scale comparisons. However, the observing conditions, i.e., daytime versus nighttime including the telescope elevation ranges as well as the image quality inferred from σ_1 and σ_2 (Section 3.1) of these pointings are similar with respect to the rest. Therefore, we do not expect errors associated with these to behave any differently.

4.1. Astrometric Precision

The left panel of Figure 11 shows astrometric comparison for central targets and gain calibrators. The median offsets in R.A. and decl., i.e., ΔR.A. and Δdecl. are −0.″03 and 0.″02, respectively. The median absolute deviations (MAD) in ΔR.A. and Δdecl. are 0.″32 and 0.″42, respectively.

More accurate positions for 35 MALS central targets and 71 gain calibrators are available from the VLA Calibrator Manual.[23] The median ΔR.A. = 0.″00 (MAD = 0.″04) and Δdecl. = 0.″01 (MAD = 0.″04) from comparison of these are even smaller. The histogram distributions of ΔR.A. and Δdecl. are also shown in Figure 11. These are well modeled by Gaussian functions with $\sigma = 0.''48$ and 0.″62, respectively, and are consistent with the scatter ($\sigma = 1.483 \times$ MAD) estimated

[23] https://science.nrao.edu/facilities/vla/observing/callist

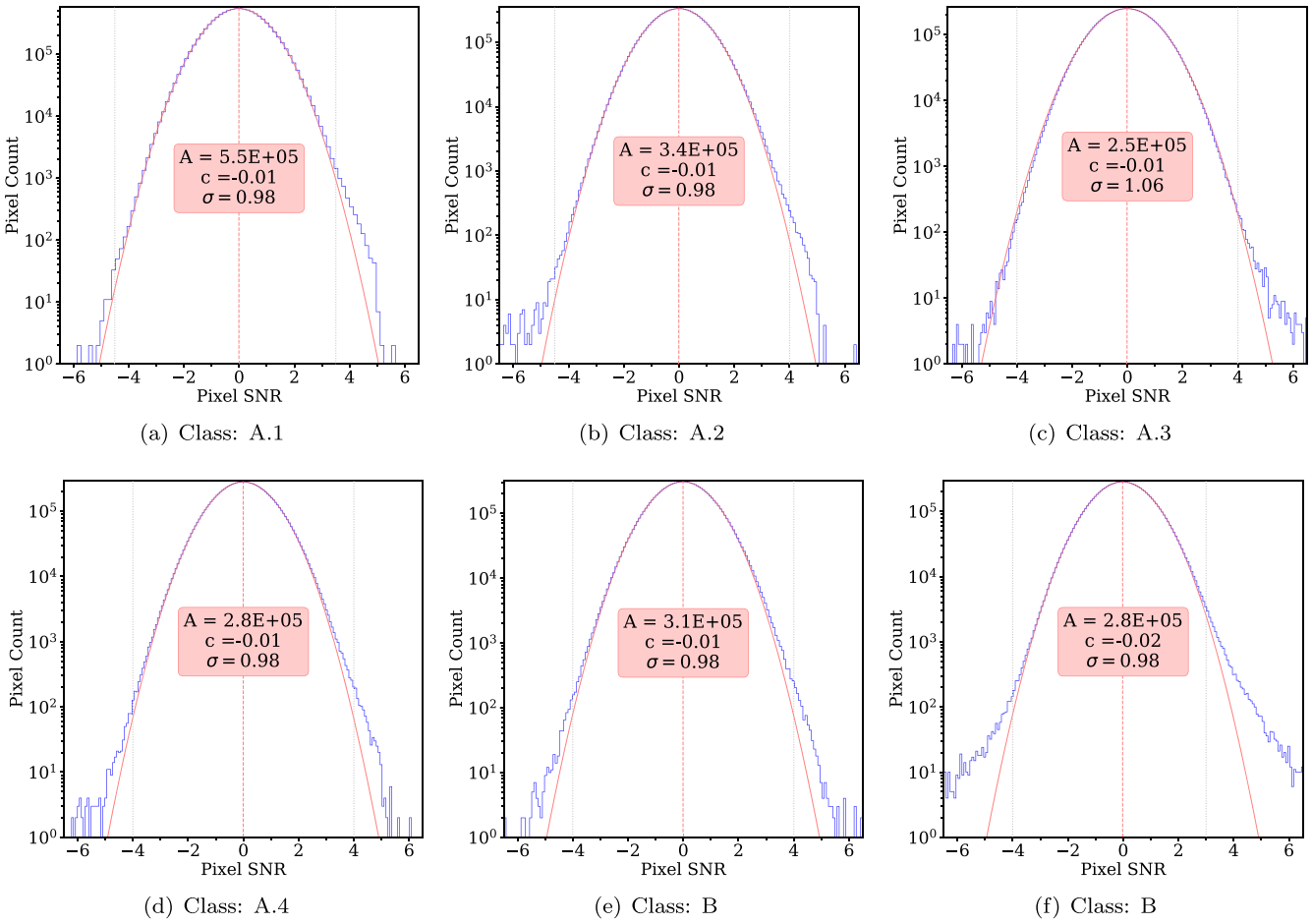

(a) Class: A.1 (b) Class: A.2 (c) Class: A.3

(d) Class: A.4 (e) Class: B (f) Class: B

Figure 9. Examples of S/N distribution of pixels in the residual images generated by `PyBDSF` for each class of pointings discussed in Section 3.1. The sigma-clipped Gaussian ($Ae^{-(x-c)^2/2\sigma^2}$) fitted to the distribution using only the S/N range marked using the dotted vertical lines is also shown.

from MADs. We note that three central targets, i.e., J0110-1648, J1234+0829, and J2218+2828 have complex morphology in MALS and are inappropriate for astrometric comparison. Hence, these have been omitted from Figure 11.

In the right panel of Figure 11, we provide astrometric comparison of 1150 sources detected (S/N >8; `S_code` = ``S'') in four multiply observed MALS pointings. The median R.A. and decl. offsets between sources detected in the two epochs are $0\farcs03$ (MAD $= 0\farcs17$) and $0\farcs00$ (MAD $= 0\farcs20$), respectively. The scatter is slightly larger at lower S/N (see color-coded points for S/N < 15) and a single Gaussian is not a good fit to the distributions of ΔR.A. ($\sigma = 0\farcs25$) and Δdecl. ($\sigma = 0\farcs25$) but consistent within 20% with the scatter inferred from robust MAD statistics. Overall, the scatter is quite small compared to the size of the average SPW9 synthesized beam, which, for clarity, is shown as a circle of diameter $4''$, i.e., half of its actual size. Also, prior to mixing the sources from individual fields to generate the combined sample of multiply observed sources, we have verified that each of the fields (the four fields span a decl. range of $\sim 50°$) show similar distributions of astrometric offsets, and therefore the results reported here are not biased by a particular set(s) of observations.

For the *third* part of the comparison with NVSS involving all of the compact and isolated sources detected in SPW9 images, we consider sources brighter than 10 mJy in NVSS. This reduces the scatter introduced by position uncertainties in NVSS, which increase from $\sim 1''$ at an integrated flux density of 10 mJy to $\sim 6''$ at the 5σ detection threshold of 2.5 mJy (see Figure 30 in Condon et al. 1998). The astrometric comparison of these is shown in Figure 12 with individual points color coded according to their S/N values in `log` scale. The median R.A. and decl. offsets are $-0\farcs05$ (MAD $= 0\farcs63$) and $0\farcs02$ (MAD $= 0\farcs78$), respectively. We found that $\sim$95% of the sources show a positional mismatch with NVSS that is smaller than MALS SPW9 average restoring beam (see circle in Figure 12). From the comparison with sources (S/N > 10) compact in FIRST (Figure 13), the median ΔR.A. and Δdecl. are $0\farcs02$ (MAD $= 0\farcs21$) and $0\farcs05$ (MAD $= 0\farcs29$), respectively.

Overall, small (i.e., subpixel) level values of median ΔR.A. and Δdecl. indicate that the systematic errors associated with source positions are under control. Therefore, we do not apply any offsets to the images or positions reported in the catalog. The offsets obtained from the comparison with FIRST are comparable to those estimated using multiply observed sources, affirming that these provide a reasonable estimate of the systematic errors associated with the astrometry. To capture the S/N dependence of ΔR.A. and Δdecl. (see distributions in Figure 13), we grouped them in bins consisting of 400 or more sources. We modeled offsets in each S/N bin using a Gaussian and also estimated the scatter (σ) for each bin using MAD

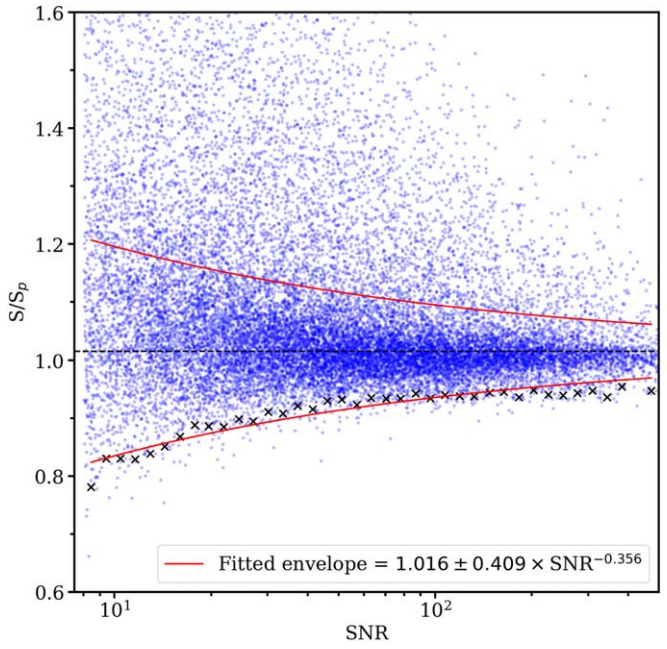

Figure 10. The reliability envelope used to select compact sources from a sample of isolated, single-component sources (S/N > 8) detected in MALS SPW9 images. The black "×" symbols mark the lower envelope encompassing 95% of these sources with total-to-peak flux density ratio < 1. The solid red line represents the fit to "×" and the reflected envelope. Out of 22,425 sources, 15,834 (∼70%) lie inside the envelope.

statistics. The two estimates are consistent within 10%. Since the MAD-based estimate is robust to outliers and systematically larger, we adopt this as a slightly conservative contribution to the systematic error ($\sigma_{\rm astrom,sys}$) budget. We model the S/N-dependent behavior of scatter in ΔR.A. and Δdecl. as $\sigma_{\rm astrom,sys} = (1.8 \times {\rm S/N}^{-0.8} + 0.2)$ and $(3.1 \times {\rm S/N}^{-1.0} + 0.3)$, respectively. These offsets level off at S/N ⩾80 with values of ΔR.A. = 0.″2 and Δdecl. = 0.″3.

The errors on (`RA_mean`, `DEC_mean`) and (`RA_max`, `DEC_max`) reported in Table 3 have been estimated following:

$$\sigma = \sqrt{\sigma^2_{\rm astrom,fit} + \sigma^2_{\rm astrom,sys}}, \quad (1)$$

where $\sigma_{\rm astrom,fit}$ is the error in R.A. or decl. from `PyBDSF` fitting, and $\sigma_{\rm astrom,sys}$ is the systematic error based on the analysis of offsets in off-axis (for S/N < 400) and central sources (S/N > 400). In MALS DR1, the same recipe has been used to derive astrometric errors for SPW2. Note that for S/N = 8 (15), $\sigma_{\rm astrom,sys}$ = 0.″5 (0.″4) and 0.″7 (0.″5), respectively. For the catalog, the astrometric error corresponding to the median S/N of 9 is 0.″8.

Finally, to investigate variations in astrometric accuracy across the survey footprint, we estimated astrometric offsets for each pointing as the median of $\sqrt{(\Delta{\rm R.A.})^2 + (\Delta{\rm decl.})^2}$ for all of the compact and isolated sources within the pointing. Due to better overlap with the MALS footprint, we use NVSS for this purpose. The results are shown in Figure 14. Clearly, there are no significant deviations across the survey footprint—neither in R.A. nor in decl. for individual pointings or when grouped into bins of 10°. We also do not find any relationship between the offsets and the flux density of the central source. The two pointings with most extreme offsets of ∼2.″5 are J1007−1247 and J2023−3655.

4.2. Flux Density Scale

In the left panel of Figure 15, we compare the flux density measurements of MALS central targets and gain calibrators with NVSS. We reject three central targets with complex morphology in MALS (Section 4.1). Also, to account for the small frequency difference ($\Delta\nu \approx 20$ MHz) between NVSS (at 1.40 GHz) and MALS-SPW9 catalogs (at 1.38 GHz), we scaled the NVSS flux densities to the frequency of our observations using a spectral index of $\alpha = -0.74$ (see Section 5.2). Further, due to the coarser spatial resolution (FWHM = 45″), a single NVSS source may split into multiple sources in MALS. Among 345 central targets, 72 have additional radio sources in MALS within 60″ radius and the remaining are isolated. The median MALS-to-NVSS flux ratio considering all of the central targets and gain calibrators is 1.00 (MAD = 0.04), implying that the flux densities of radio sources at the pointing center are in excellent agreement with NVSS. In all cases, the total flux density of additional sources is small (median ∼1% of the NVSS flux) and, therefore, inconsequential to the sample statistics. Note that several gain calibrators are observed multiple times in MALS. For comparison with NVSS, we have taken the average of their flux density measurements. In Figure 15, the five outliers among gain calibrators are blazars, well known in the literature for their variability at radio wavelengths.

The right panel of Figure 15 provides a comparison of flux densities of 1150 sources (S/N > 8; `S_code` = "S") detected in four multiply observed MALS pointings. The median integrated flux density ratio is 1.01 (MAD = 0.08). This increase in the scatter as compared to the central targets can be attributed to the low-S/N (⩽15) sources. The latter, when treated separately, have an MAD of 12%. In contrast, the high-S/N (>15) sources alone, exhibit an MAD of only 5%, similar to the central sources (∼4%). In conclusion, at low S/N, issues related to inaccurate modeling of source emission lead to a increased scatter in the distribution.

Next, we compared the MALS and NVSS flux densities of 15,834 compact and isolated sources detected over the entire MALS footprint (Figure 16). At 1.38 GHz, the median MALS-to-NVSS ratio is 1.06 (MAD = 0.15). The MALS-to-FIRST ratio estimated using 5990 compact sources is 1.12 (MAD = 0.15). Restricting the comparison to brighter (>10 mJy) 4506 sources (30% of 15,834) in NVSS, we find a median MALS-to-NVSS ratio of 1.03 (MAD = 0.09). This is very similar to the values obtained from the comparison of multiply observed sources presented in the right panel of Figure 15. In conclusion, the overall observed flux density offset of 6%–12% between these surveys is well within the absolute flux density accuracy expected at these frequencies (∼1 GHz). Thus, we do not apply any adjustment to the flux density scale of MALS sources.

The fitting errors (`Total_flux_E_fit`) on flux densities from `PyBDSF` are likely underestimated. The larger scatter in flux density comparisons at lower S/Ns could be due to improper Gaussian modeling caused by confusion with adjacent noise pixels. The flux density comparison of MALS with NVSS and FIRST could also be affected by additional sources of error, e.g., direction-dependent errors including the accuracy of primary beam correction and long-term variability of AGNs. Therefore, we use the comparison between multiply observed sources in MALS to obtain an estimate of S/N-dependent systematic uncertainty (`Total_flux_E_sys`) in

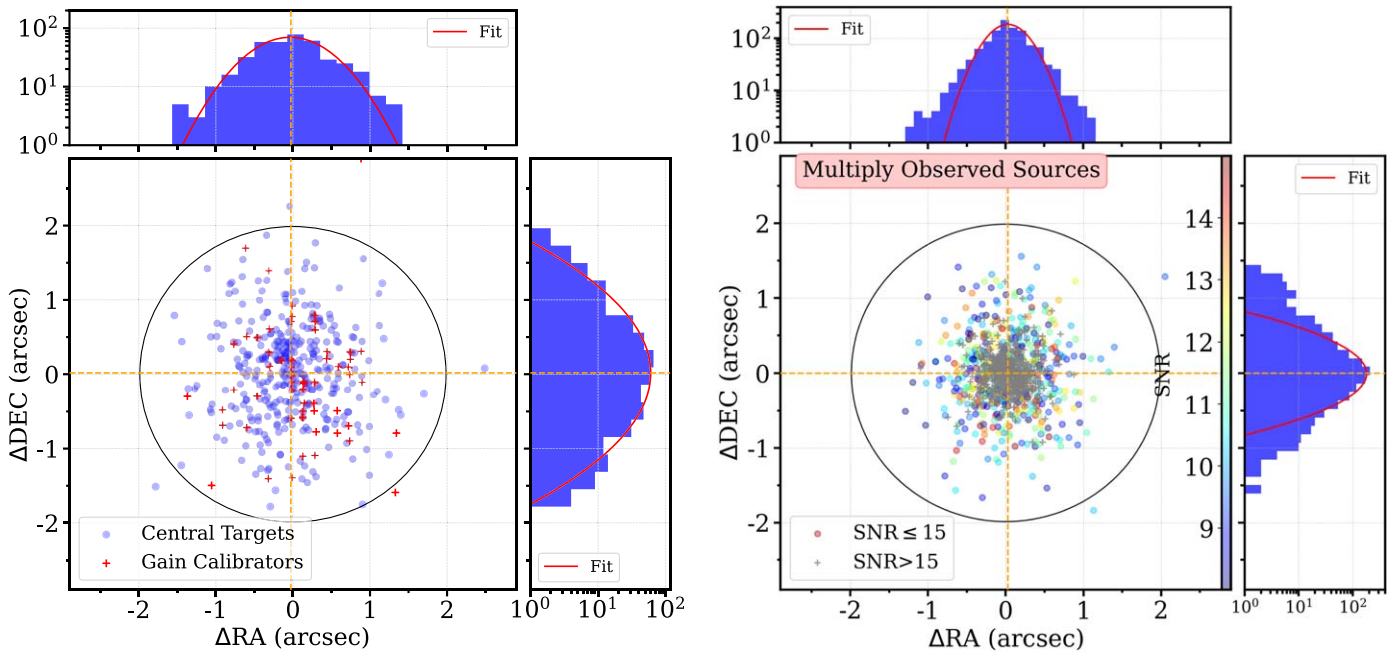

Figure 11. Astrometric comparison of 345 targets and 64 gain calibrators from MALS with NVSS (left) and 1150 compact sources detected in four twice-observed MALS fields (right). The dashed lines mark median offsets. The circle represents half of the average SPW9 restoring beam FWHM (8″). For clarity, three points have been omitted from the left panel (see the text for details). In the right panel, sources with $8 \leqslant S/N \leqslant 15$ are color coded. The histogram distributions of ΔR.A. and Δdecl. and Gaussian fits to these are also shown.

the flux density measurement. For this, we fit a simple power law, $1.13 \pm 0.01 \times S/N^{-0.743 \pm 0.002}$, to the scatter ($1.483 \times$ MAD) in the percentage variation observed in flux density measurements of these sources (Figure 15; right panel). The systematic error is then given by, $\texttt{Total\_flux\_E\_sys} = \texttt{Total\_flux} \times \ 1.13 \times S/N^{-0.74}$. The total error is then calculated as the quadratic sum of the fitting and systematic errors as,

$$\texttt{Total\_flux\_E} = \sqrt{\texttt{Total\_flux\_E\_fit}^2 + \texttt{Total\_flux\_E\_sys}^2}. \quad (2)$$

In MALS DR1, the same recipe has been used to derive total errors on flux densities for SPW2.

Finally, in Figure 17 we present the median flux density ratios of compact and isolated sources for each pointing. Clearly, there are no systematic trends across the survey footprint, neither in R.A. nor in decl. for individual pointings or when grouped in bins of 10°. However, two pointings, i.e., J1833-2103 and J0211+1707, associated with central sources of ∼10 Jy and ∼0.7 Jy show extreme median offsets (∼30%). In general, we do not find any relationship between the offsets and the flux density of the central source.

4.3. Accuracy of Primary Beam Correction

In Figure 18, we plot the ratio of MALS and NVSS flux densities of compact and isolated sources as a function of distance from the pointing center. The median offset for this comparison involving the primary beam model from `katbeam` is 1.06 (MAD = 0.15). In general, the offsets are <∼10%, implying that the `katbeam` allows for a reasonable primary beam correction. Note that MeerKAT's primary beam is elliptical (Mauch et al. 2020), and the `katbeam` only provides a static beam for image domain correction at a position angle of 0°. We noticed that the peak of the `katbeam` model for SPW9 is offset with respect to the center of the image by about 11″. As expected, adjusting for this offset does not lead to any significant change in the values.

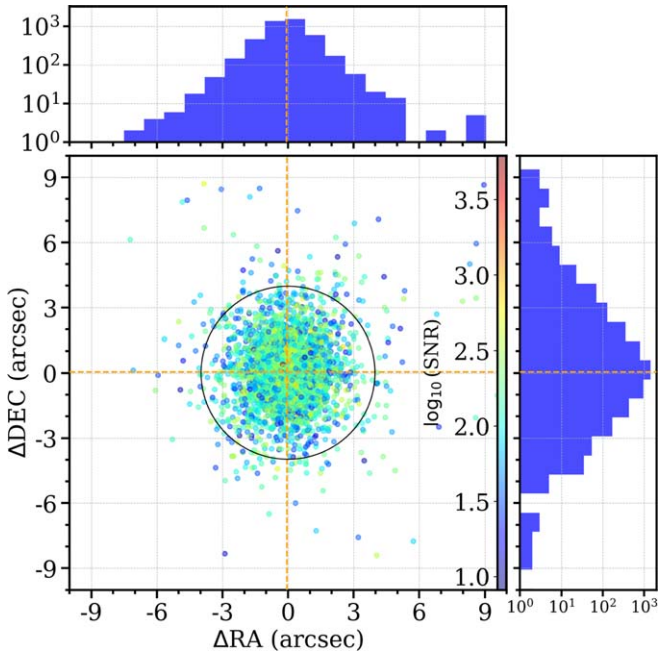

Figure 12. Astrometric comparison of 4506 compact and isolated field sources from MALS with NVSS. The dominant fraction (∼95%) is within the restoring beam (∼8″; circle). The dashed lines mark the median offsets.

We also performed primary beam correction using `plumber`[24] (Sekhar et al. 2022). `plumber` generates primary beam

[24] https://github.com/ARDG-NRAO/plumber

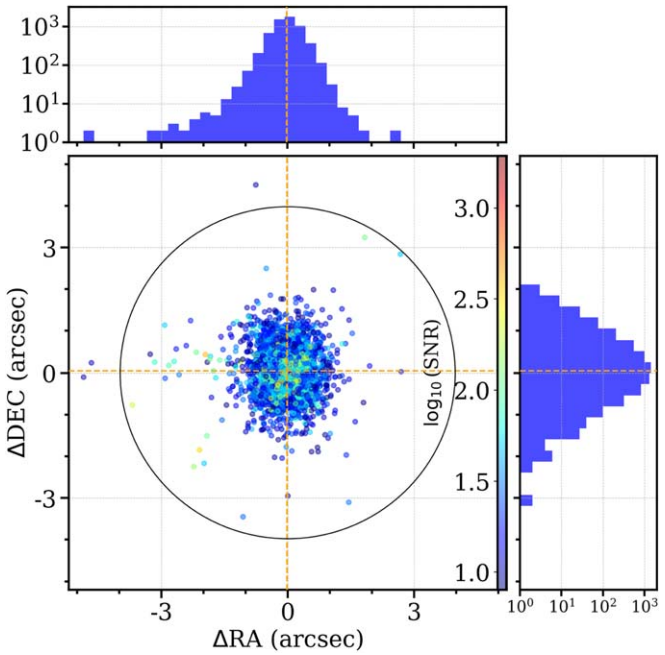

Figure 13. Astrometric comparison of 5990 sources from MALS with FIRST. The remaining details are the same as in Figure 12.

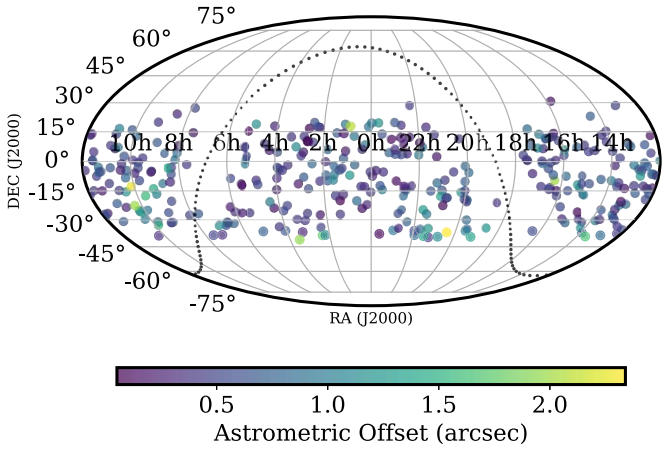

Figure 14. Sky distribution of MALS pointings—the points have been color coded on the basis of median astrometric offsets between MALS and NVSS. The MALS pointings at $\delta < -40°$ do not overlap with NVSS and, hence, are absent in this plot.

models for radio interferometers using Zernike model coefficients of the antenna aperture illumination pattern (also see de Villiers 2023, for holographic measurements). The typical *L*-band observation of an MALS target are split into three scans at different hour angles over a duration of 3.5 hr. In such a situation, the primary beam correction ought to be applied over the range of parallactic angles using convolution kernels during the gridding of the visibilities (Bhatnagar et al. 2013). In the image plane, one can at best use the illumination pattern at a specific orientation or averaged (smeared) over the range of parallactic angles traversed during the observation. None of the image plane options are ideal, and at best are approximations of a visibility-plane primary beam correction. Therefore, we adopted the simple approach of generating a beam model for each pointing at the parallactic angle at the center of the observing run.

The ratios of `katbeam` and `plumber` beam models for SPW9 and SPW2 are shown in Figure 19. In Appendix C (Table C1), we also provide annular averaged (2′ bins) values for these. In general, in the inner region, the two beam models follow each other and diverge in the outer regions. The difference between the two models is much less dramatic at SPW2, and both are consistent within 3% up to $\Delta\theta = 70'$, where $\Delta\theta$ is the angular distance from the pointing center. Compared to SPW9, at SPW2 the `katbeam` is narrower than the `plumber` beam. Consequently, the spectral indices obtained using the former—especially in the outer regions of the image—are slightly steeper, i.e., the median spectral index changes from −0.70 to −0.74 (see last column of Table C1 and Section 5.2).

For the data release presented here, we provide SPW9 and SPW2 flux densities, i.e., `Total_flux`, `Isl_flux` and `Peak_flux`, based on `katbeam`. The column `Flux_correction` provides the multiplicative factor to be applied to these to obtain flux densities based on the `plumber` model. For convenience, total integrated flux densities for `plumber` model are provided in `Total_flux_measured`. For SPW9, over $0' < \Delta\theta < 40'$, the `plumber` corrected flux densities gradually increase from 0% to 3% relative to `katbeam` (Figure 18). In the outer regions, i.e., over 40′–60′, this increases steeply to 10%. Noticeably, the ratio based on the `plumber` beam model remains flatter, and close to the overall median (1.09) as far as 50′ from the pointing center. Therefore, the `plumber` model may be a closer representation of MeerKAT's primary beam in the outer regions. However, overall the `plumber` model yields a median flux density offset of 9% with respect to NVSS with an MAD of 16%, higher than the offsets obtained using `katbeam`. We anticipate further improvements by applying visibility-plane primary beam corrections via AW projection (Bhatnagar et al. 2013).

5. Discussion

In this section, we present the overall properties of SPW9 and SPW2 catalogs summarized in Table 4 and examine certain aspects to demonstrate their usage and utility. The distribution of total flux densities (`Total_flux`) and source size (`Maj`) are presented in Figure 20 (see also Table 4). As expected for the spatial resolution of 8″–12″, the majority of sources (∼90%) are modeled with a single-Gaussian component. Only 4% of the sources require three or more Gaussian components. Compared to SPW9, the radio source sizes are systematically larger at SPW2 (see bottom panels in Figure 20). The median value of the deconvolved major axis for SPW2 is 3.″9, whereas for SPW9 it is 2.″8. The median angular separations between the Gaussian components of "M" type (`S_code` = "M") sources are 15.″4 (SPW2) and 12.″6 (SPW9), respectively. The median flux density is also larger at SPW2. All of these suggest that the larger SPW2 sizes are due to the excess of extended emission and not an artifact of coarser resolution.

At the extreme right end of the distributions in the bottom panels of Figure 20 are the largest radio sources identified in the sample. Contrary to intuition, both the `Total_flux` and `Isl_Total_flux` for these complex morphology sources modeled with more than 50 Gaussian components are in good agreement—the two measurements for these differ by about ∼5% (see also Wagenveld et al. 2023). The details of four

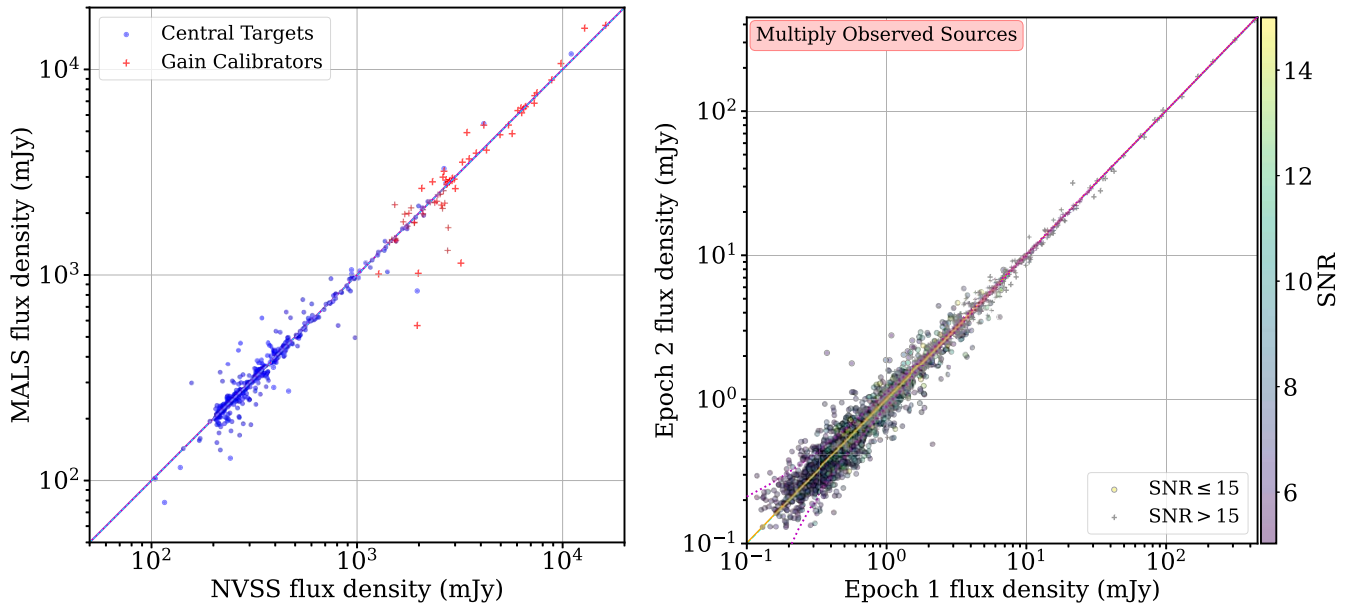

Figure 15. Integrated flux density comparison at 1.38 GHz of 345 central targets and 64 gain calibrators from MALS with NVSS (left) and 1150 compact sources (S/N > 8) detected in four twice-observed MALS fields (right). The dashed lines mark median offsets. In the right panel, sources with 8 ⩽ S/N ⩽15 are color coded.

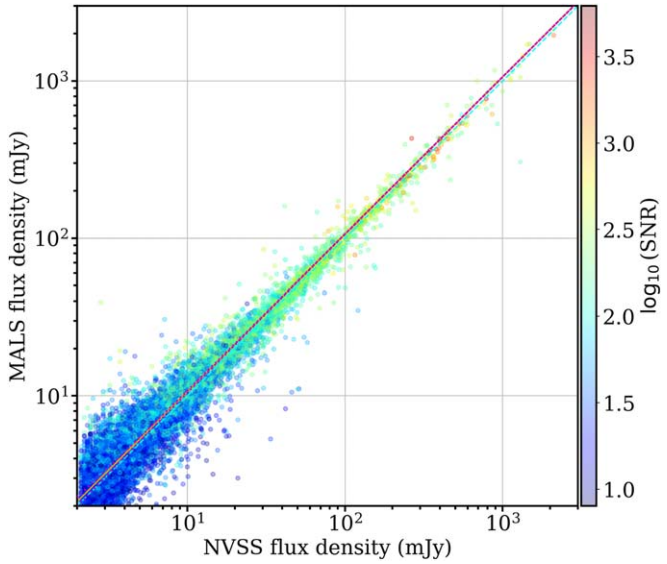

Figure 16. Flux density comparison at 1.38 GHz of 15,834 compact and isolated sources from MALS with NVSS.

unique largest radio sources (Maj ⩾300″) detected in SPW2 are as follows. Located at $z = 0.056$ (Jones & McAdam 1992), J231757.32-421337.3 is a radio galaxy with a projected linear extent of about 350 kpc. J150726.21+082924.9, which has a linear extent of about 520 kpc, is at $z = 0.079$ (Abazajian et al. 2009). Another radio galaxy, J024105.35+084448.2, associated with NGC1044, is located at $z = 0.021$ (Davoust & Considere 1995) and has a linear extent of about 150 kpc. The redshift of J034521.03−454816.7 (PKS 0343-459) is unknown. Overall, MeerKAT's high surface brightness sensitivity allows us to detect large radio sources with faint diffuse lobes. Two of the four distinct large sources in SPW2 are outside the field of the SPW9 images, and another is divided into multiple sources due to the increased resolution. So, in SPW9, we essentially only observe one source with Maj ⩾300″.

In general, complex Fanaroff–Riley class I (FRI; edge-darkened; Fanaroff & Riley 1974) morphologies are well represented by the PyBDSF Gaussian decomposition. But a single source with Fanaroff–Riley class II (FRII; edge-brightened) morphology in the lower-frequency SPW2 image may be split into multiple sources in the SPW9 image due to (i) higher spatial resolution, and (ii) weaker jet emission linking the lobes. We crossmatch "M"-type sources from SPW2 catalog with all of the sources in SPW9 catalog. We use a crossmatching radius equal to half the Maj parameter of the SPW2 source. Out of 34,103 matched sources, in 30,537 cases an SPW2 source is uniquely matched to a single source in SPW9. In the remaining 3566 cases, we find multiple matches in SPW9. About 90% of these are fainter than 90 mJy and form only a minuscule portion of the catalog. Nevertheless, the flux density and spectral index measurements for these could be miscalculated. The future MALS data releases will identify such missing linkages across the catalog through the Source_linked parameter in Table 3.

In the following, we derive radio source counts and discuss the completeness of the MALS catalog (Section 5.1). We also derive spectral indices using SPW2 and SPW9 flux densities to understand the nature of detected radio source population (Section 5.2). Using TGSS ADR1 flux densities, we identify ultra-steep-spectrum (USS) sources as potential high-z radio galaxies. Finally, we investigate the variable and transient population of sources from the catalog (Section 5.3). Throughout these analyses, we take into account the above-mentioned complications caused by differing radio source morphology and spatial resolution at SPW2 and SPW9. Therefore, in addition to being sanity checks and adding value, these explorations also serve as demonstrations of the usage of MALS catalog.

5.1. Differential Source Counts at 1.4 GHz

We estimate the differential source counts at 1.4 GHz following standard recipes in the literature (e.g., White et al. 1997; Condon et al. 1998). For scaling the integrated source

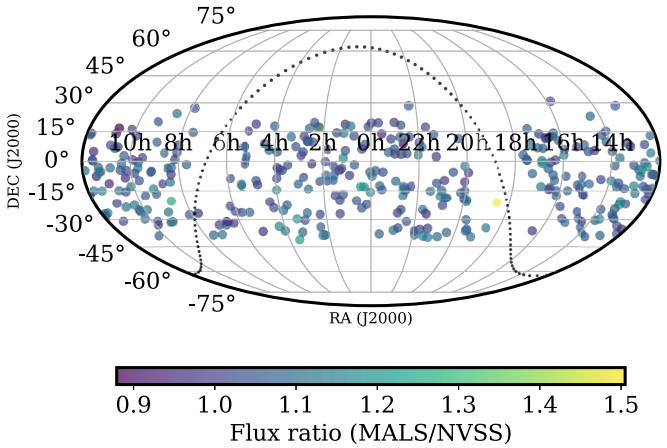

Figure 17. Sky distribution of MALS pointings for median flux density ratios between MALS and NVSS. The remaining details are the same as in Figure 14.

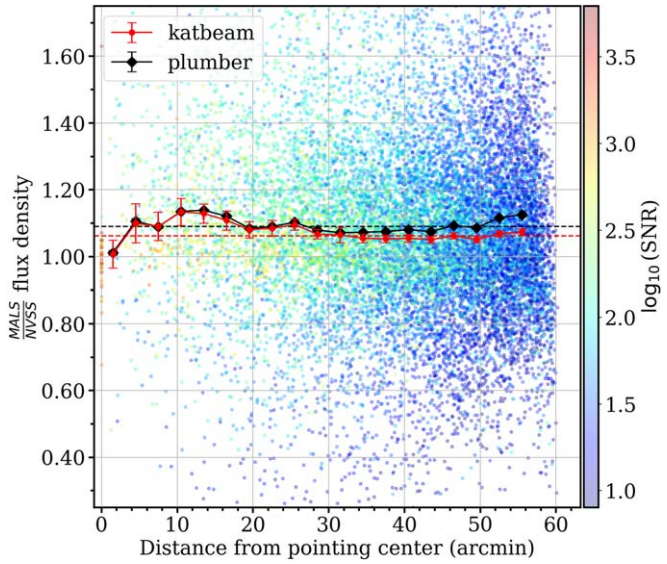

Figure 18. MALS SPW9 to NVSS flux density ratio for 15,834 sources. The scatter plot is for flux densities corrected using the `katbeam`. The circles and diamonds with error bars (1σ) correspond to ratios ($3'$ bins) based on beam models from `katbeam` and `plumber`, respectively. The NVSS flux densities have been scaled to 1380 MHz using $\alpha = -0.7$ for this analysis. The horizontal dashed lines represent median values for the whole sample.

flux densities (`Total_flux`) from the SPW9 catalog, we adopt a spectral index of -0.74 (see Section 5.2). We binned these flux densities in logarithmic bins (ΔS) of width 0.2 dex. The numbers of sources detected in each of these bins are normalized by the total survey area to obtain the differential source counts. These are then multiplied by $S^{2.5}$, where S is the mean of `Total_flux` corresponding to that bin. The weighting by $S^{2.5}$ divides these by counts expected in a static Euclidean Universe. These *raw* source counts are plotted in Figure 21 (see also Table D1). The bright targets at the center of each pointing were selected as part of the survey design. So, these have been excluded from the source count analysis. We also exclude the regions with low reliability, i.e., shaded regions shown in Figure 8.

The normalized source counts in each bin need to be corrected for the visibility function representing the area over which the source with a given flux density can be detected. We determine the visibility function by estimating the survey area over which the source with a given peak flux density can be detected at $S/N > 5$ based on the rms maps (generated from `PyBDSF` runs on primary beam-corrected images). The corresponding *corrected* differential source counts at 1.4 GHz for flux densities based on `katbeam` (`Total_flux`) and `plumber` (`Total_flux_measured`) beam models are plotted in Figure 21 and also provided in Table D1. The counts based on the two beam models agree within 2%. Note that the relevant survey area, i.e., column 4 in Table D1, is nearly constant for sources brighter than 2 mJy, and plummets to a few pointings below 0.1 mJy. Also, above 1 Jy only a handful of sources are detected in MALS, and the counts are highly uncertain.

Figure 21 also presents 1.4 GHz Euclidean-normalized differential source counts from various other surveys. It clearly demonstrates that the *corrected* source counts from MALS, within the scatter of various measurements, are in quite good agreement with the literature. The comparison between MALS and MeerKAT-DEEP2 counts shows that the SPW9 catalog is complete down to 2 mJy. Below 0.5 mJy level, the completeness falls off steeply, and at 0.1 mJy it is only about 50% complete. Between 0.5 and 200 mJy, the MALS source counts are systematically higher ($\sim$10%) than the source counts from NVSS and FIRST. The difference is, as expected, reduced to 3% if the MALS flux densities are reduced by 6% to account for the systematic offset with respect to NVSS noted in Section 4.2. Over the same flux density range, the counts from the MIGHTEE COSMOS field oscillate around MALS counts and may be affected by the cosmic variance. The XMM-LSS counts over 10–50 mJy are systematically lower, which Hale et al. (2023) suggested may likely be due to the incomplete grouping of emission components during source finding (see Hale et al. 2023 for details).

Overall, the slight offsets between source counts from various surveys in the 0.5–200 mJy range could originate from instrumental and analysis effects (see also Condon 2007; Prandoni et al. 2018; van der Vlugt et al. 2021). In particular, the visibility function estimated here for MALS does not include corrections for Eddington and resolution biases. Eddington bias leads to redistribution of source counts in flux density bins in the presence of random noise and biases the detectability of unresolved sources near the detection threshold (Eddington 1913, 1940). The resolution bias leads to underestimation of extended sources in a flux density bin. This is a consequence of the fact that the detection of a source depends on its peak flux density; therefore, a larger source due to its lower peak flux density will drop below the detection threshold much sooner than a smaller source (Prandoni et al. 2006; Smolčić et al. 2017b; Mandal et al. 2021; van der Vlugt et al. 2021).

A detailed exploration of the abovementioned issues will be presented in future papers involving MALS catalogs from more sensitive wideband images. This will include simulations involving injection of radio sources of known flux densities and sizes in residual images and subjecting these to the same source-finding procedures as used for cataloging to determine completeness as a function of rms and radio source morphology (see, e.g., Bonaldi et al. 2021; Shimwell et al. 2022; Hale et al. 2023). Indeed, wideband images of MALS exhibit large variations in completeness for compact and extended sources (see Figures 7 and 8 of Wagenveld et al. 2023).

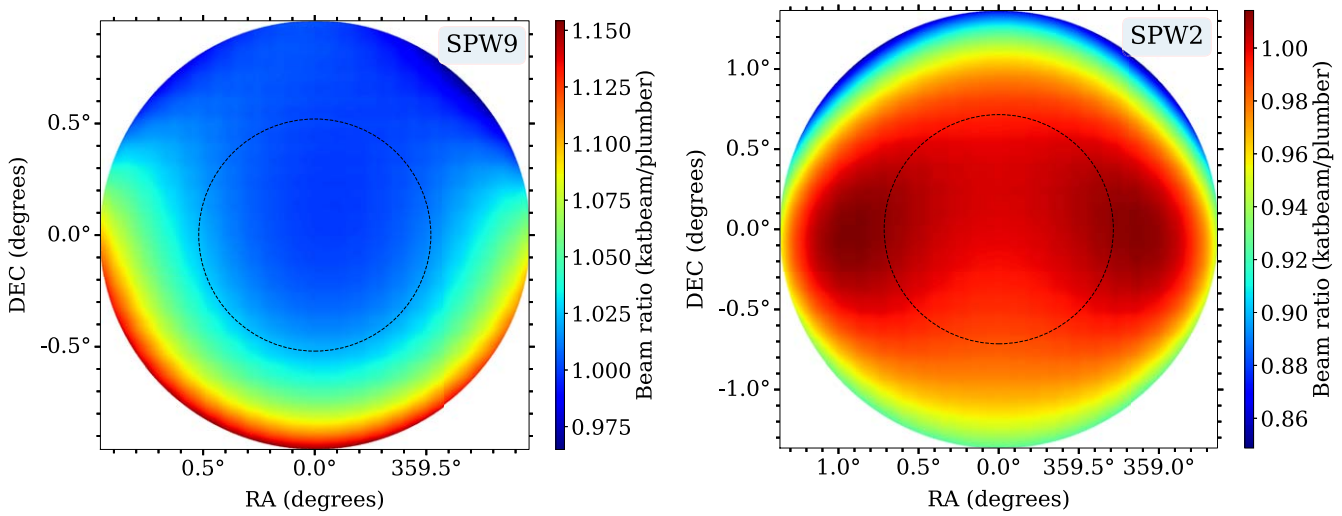

Figure 19. Ratios (`katbeam` / `plumber`) of primary beams for SPW9 (left) and SPW2 (right). The extent of these images is the same as the primary beam-corrected MALS images. The dashed circles mark beam FWHMs of 62.′5 (SPW9) and 85.′7 (SPW2) from Mauch et al. (2020).

Table 4
The MALS DR1 Catalog Summary for Two SPWs

	SPW9	SPW2
Number of sources	240,321	495,325
Median flux density (mJy)	0.87	1.03
Median angular size	9.″8	13.″2
Median deconvolved angular size	2.″8	3.″9
Number of sources (`S_code` = "S")	215,328	441,988
Number of sources (`S_code` = "M")	24,993	53,337
Number of Gaussian components	285,209	586,290
Number of sources with two components)	16,324	35,609
Number of sources with $\geqslant$3 components)	8669	17,728

Note. For a matching radius of 6″, 205,435 sources are common between SPW2 and SPW9.

5.2. Spectral Indices and Ultra-steep-spectrum Sources

Spectral indices provide useful information on the nature of radio sources and are helpful in disentangling various mechanisms responsible for the radio emission. In general, for a source, the spectral index (α) and the associated curvature (β) are related to its flux densities, S_1 and S_2 measured at ν_1 and ν_2, through the following relation:

$$S_1 = S_2\left(\frac{\nu_1}{\nu_2}\right)^{\alpha+\beta\log(\nu_1/\nu_2)}. \quad (3)$$

For the frequency coverage corresponding to SPW2 and SPW9, it is reasonable to ignore in-band curvature and use the simplified form of Equation (3) obtained by setting $\beta = 0$:

$$S_1 = S_2\left(\frac{\nu_1}{\nu_2}\right)^{\alpha}. \quad (4)$$

The associated 1σ uncertainties on α are calculated using:

$$\sigma_\alpha = \left| \frac{1}{\log(\nu_1/\nu_2)} \sqrt{\left(\frac{\Delta S_1}{S_1}\right)^2 + \left(\frac{\Delta S_2}{S_2}\right)^2} \right|, \quad (5)$$

where ΔS_1 and ΔS_2 are uncertainties associated with S_1 and S_2.

We used `Total_flux` and `Total_flux_E` in Equations (4) and (5) to calculate spectral indices and errors of 125,621 sources (S/N $>$ 8) crossmatched using a radius of 6″. The 6″ radius minimizes the number of nearest neighbors for sources without a match in SPW9. This maximizes the number of sources for which spectral indices can be estimated, however, at the expense of spurious spectral indices in the sample. Therefore, we advise caution and imposition of additional cuts to reject spurious matches and obtain suitable samples for various applications (for an example, see Section 5.2.2).

The spectral indices and errors are provided in the columns `Spectral_index_spwfit` and `Spectral_index_spwfit_E` of Table 3, respectively, of the SPW2 (reference SPW) catalog. Note that `Spectral_index_spwfit` is a two-element array, adopted to report both the spectral index and the curvature. In the first data release, we report only spectral indices (α), and leave the second element (β) blank. In the SPW2 catalog, we also provide upper and lower limits on spectral indices based on detection in either SPW2 or SPW9, respectively. The flux density for nondetection is taken as five times the local rms from the rms map. `Spectral_index_spwfit_E` is set to 999 or −999 to indicate whether the reported value in the SPW2 catalog is an upper or lower limit, respectively.

5.2.1. Systematic Uncertainty on α

Figure 22 shows α_{spw9}^{spw2} derived from `katbeam` corrected flux densities as a function of distance from the pointing center. We excluded from this analysis 12 pointings (marked with $\star$ symbols in the online machine-readable table version of Table A1) based on unusually high rms in the SPW2 images. This led to a sample of 122,077 sources detected in both of the SPWs with S/N $>$ 8. For comparison, the median spectral indices obtained using `plumber` corrected flux densities are also shown. The `katbeam`- and `plumber`-based spectral indices diverge from the median in the outer regions. Therefore, there may be systematic uncertainties of the order of $\pm$0.05 in spectral indices beyond 45′ from the pointing center (see the last column of Table C1). Further improvements in these will follow from better modeling of the frequency-dependent behavior of the MeerKAT beam.

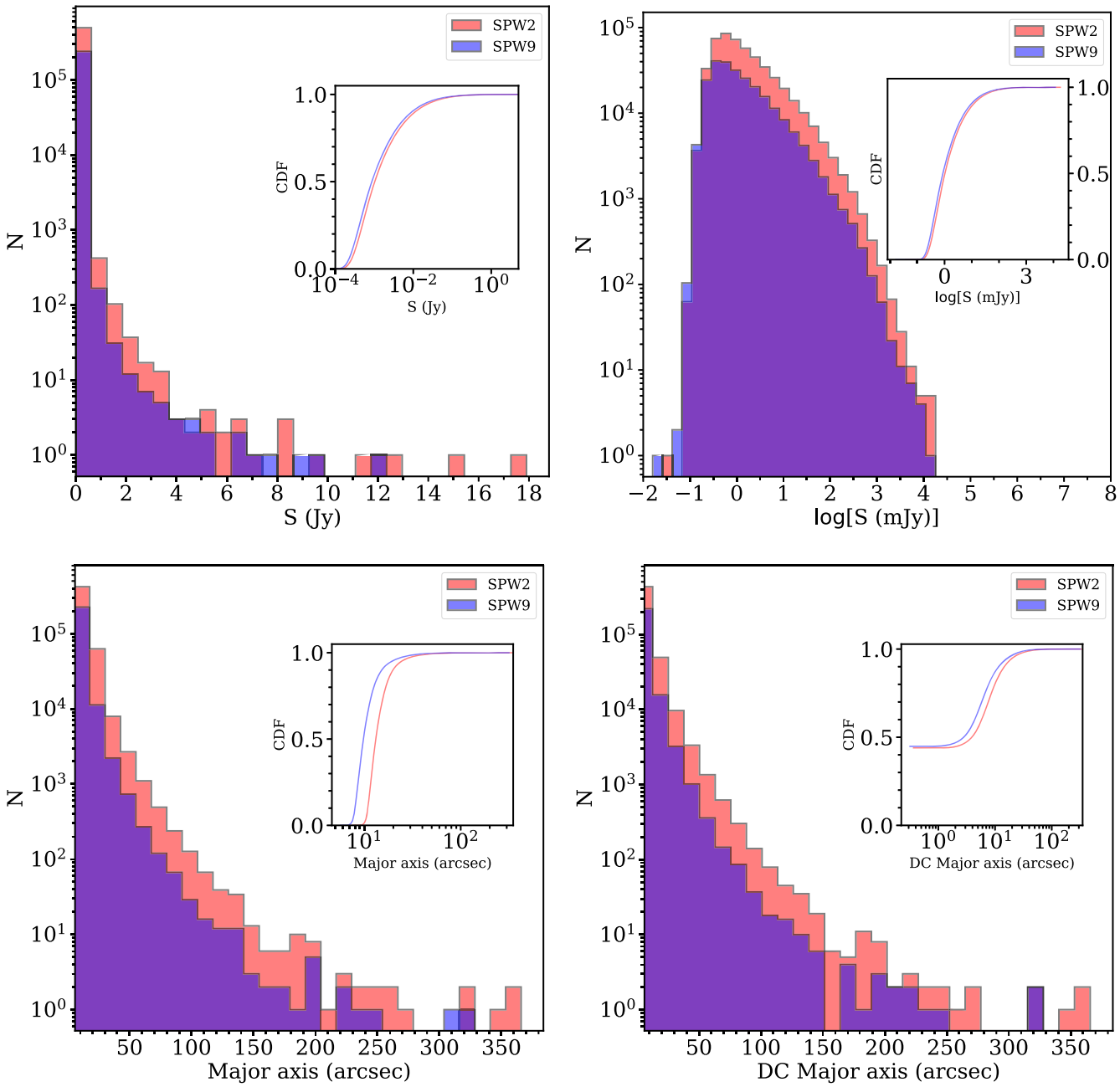

Figure 20. Distributions of integrated flux densities (S) in linear and log scales (top panels), and apparent and deconvolved (DC) major axis of sources (bottom panels). The insets show CDF.

Additionally, the α_{spw9}^{spw2} measurements could be affected by systematic uncertainties due to the splitting of a source in the SPW2 image into multiple sources in the higher-spatial-resolution SPW9 image. The flux density measurement of a source may also be affected by blending with a nearby source in one of the SPWs. The extent of contamination due to blending depends on the complex interplay between intrinsic spectral index of a source and its position in the primary beam, making it less tractable.

5.2.2. α–*Flux Density Correlation*

Several studies have reported flattening of spectral index with decreasing flux density (e.g., Prandoni et al. 2006; de Gasperin et al. 2018; Tiwari 2019), but counter examples have also been reported (e.g., Ibar et al. 2009). The statistically large sample of spectral indices from MALS DR1 offers an opportunity to test this. To derive a suitable sample of spectral indices for this purpose, we consider the following cuts on the properties of radio sources:

1. For an "S"-type detection in both SPWs, we require that no other source is present within 6″ radius.
2. For an "M"-type source detected in both the SPWs, this condition is modified to finding the same number of radio sources within a circle of radius (R_M) defined by the distance of the farthest Gaussian component from the source position, plus the FWHM of the synthesized beam, taken to be 10″ for all of the cases.

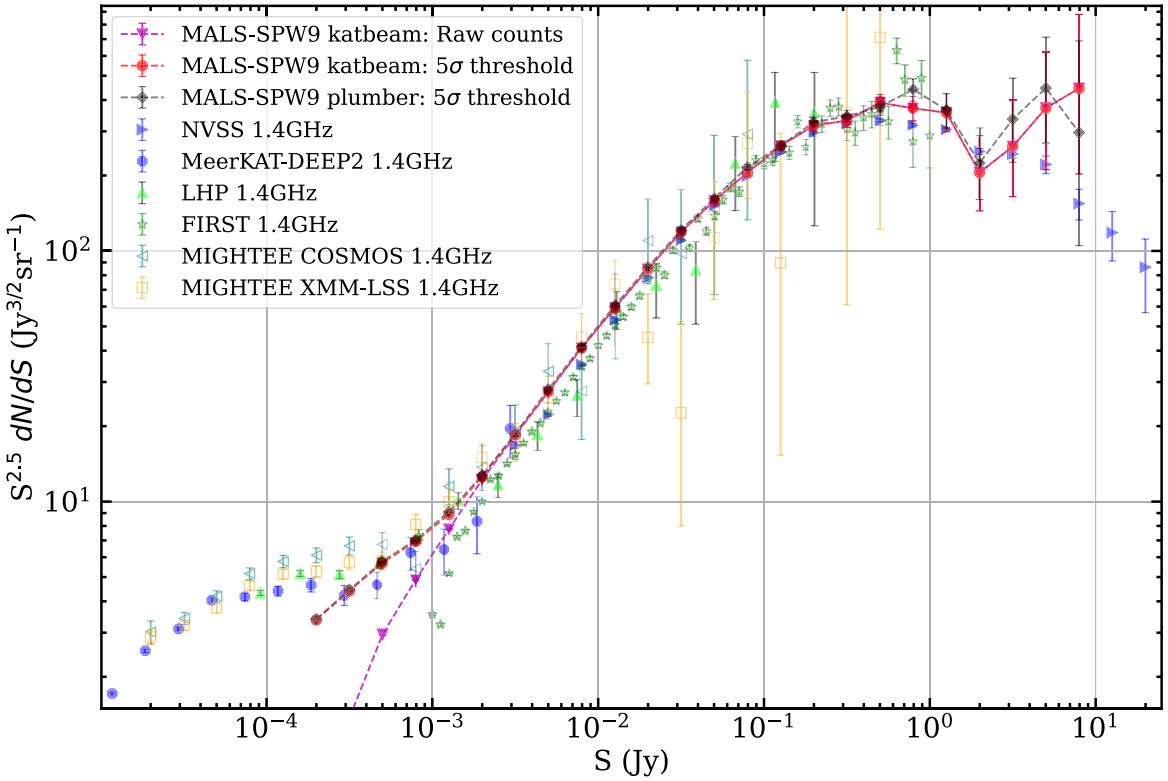

Figure 21. Differential source counts at 1.4 GHz. The MALS source counts corrected for the 5σ detection threshold, shown for both the `katbeam` (red filled circles) and `plumber` (black filled diamonds) beam models and the raw source counts (magenta filled triangles pointing downwards), have been scaled to 1.4 GHz using $\alpha = -0.74$. The counts from NVSS (blue filled triangles pointing to the right; Condon et al. 1998) and MeerKAT-DEEP2 (scaled from 1.266 GHz using $\alpha = -0.7$ and displayed using blue filled circles; Mauch et al. 2020) presented in Matthews et al. (2021), FIRST (empty green asterisks; White et al. 1997), the Lockman hole project (green filled triangles pointing up; Prandoni et al. 2018), and the MIGHTEE COSMOS (empty teal triangles pointing left) and XMM-LSS (empty orange boxes) counts based on the modified SKADS model (Hale et al. 2023) are also shown.

3. For an "M"-type source detected only in one of the SPWs, we require that no radio source is present within R_M in the other SPW.
4. For an "S"-type source detected only in one of the SPWs, we follow a two-step validation to eliminate blending and confusion with nearby sources: *(a)* no Gaussian component is present within $6''$, and *(b)* the position of the source is outside the circle defined by the nearest "M"-type source in the other SPW.

These criteria exclude the majority of sources that may have been resolved into multiple sources in SPW9 due to higher spatial resolution or weaker diffuse emission connecting the two radio lobes.

Through the abovementioned selection cuts, we derive a sample of 98,832 sources that are detected in both the SPWs at S/N $>$ 8, 10,962 detected only in SPW2, and 822 only in SPW9, at a distance $\leqslant 45'$ from the pointing center. We have again excluded the 12 pointings based on unusually high rms in the SPW2 images. Figure 23 shows the distribution of α_{spw9}^{spw2} for sources detected in both the SPWs. The median spectral index is -0.74. The median spectral indices for sources detected at S/N $>$ 8 and S/N $>$ 15 are $-0.736^{+0.003}_{-0.003}$ and $-0.757^{+0.003}_{-0.003}$, respectively. The errors define the 90% confidence level estimated by bootstrapping. The median spectral index of "M"-type sources in SPW2 is $-0.885^{+0.003}_{-0.003}$. This is slightly steeper compared to the overall median value and is expected as the extended radio emission is primarily from older electrons associated with radio lobes or even relics. Visual inspection was done on the population of sources with extreme spectral indices in Figure 23. These are generally "M"-type sources where the surrounding diffuse emission is brighter and hence well modeled in SPW2; however, in SPW9, only the brightest component's flux density is taken into consideration. Therefore, caution is advised while using spectral indices of "M"-type sources.

Figure 24 shows spectral index measurements (α_{spw9}^{spw2}) versus SPW2 (left panel) and SPW9 (right panel) flux densities. The effects of relative sensitivity limits due to the two SPWs can be seen below $\sim$0.5 mJy. To examine the spectral index versus flux density relationship, we binned all of the spectral index measurements into equally spaced logarithmic bins of flux densities, each consisting of $>$100 sources. Our initial investigation suggested that bins with S/N $<$ 15 are unsuitable for this analysis. This is primarily due to a steep increase of upper or lower limits on spectral indices in these bins (see the second and third rows of Figure 24).

Next, using the `ASURV`[25] package, which implements the survival analysis methods discussed in Feigelson & Nelson (1985) and Isobe et al. (1985), we estimate median spectral indices for bins with flux density $>$1 mJy. A clear flattening of spectral indices is seen with respect to decreasing flux densities at 1006 MHz (SPW2) and 1381 MHz (SPW9; bottom row in Figure 24). For the measurements based on `katbeam`, the gradients can be modeled as $(-0.07 \pm 0.01) \times \log S_{spw2} - (0.74 \pm 0.01)$ and $(-0.12 \pm 0.01) \times \log S_{spw9} - (0.65 \pm 0.01)$, where S is in mJy, implying that the trend is less steep

[25] ASURV Rev 1.2.

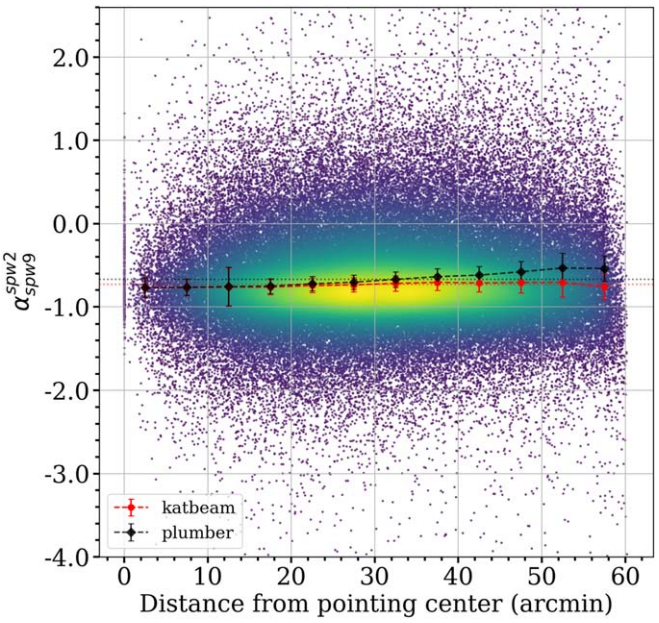

Figure 22. Spectral indices of 122,077 sources detected in both the SPWs vs. the distance from the pointing center. The red (black) points mark the median spectral indices derived from `katbeam` (`plumber`) corrected flux densities in bins of 5′. The horizontal dotted lines indicate median spectral indices for the full sample corrected using `katbeam` ($-0.732^{+0.003}_{-0.003}$) and `plumber` ($-0.680^{+0.003}_{-0.003}$) beam models. The points are color coded according to their space density. The error bars defining the 90% confidence level estimated by bootstrapping are enlarged by a factor of 10 for clarity.

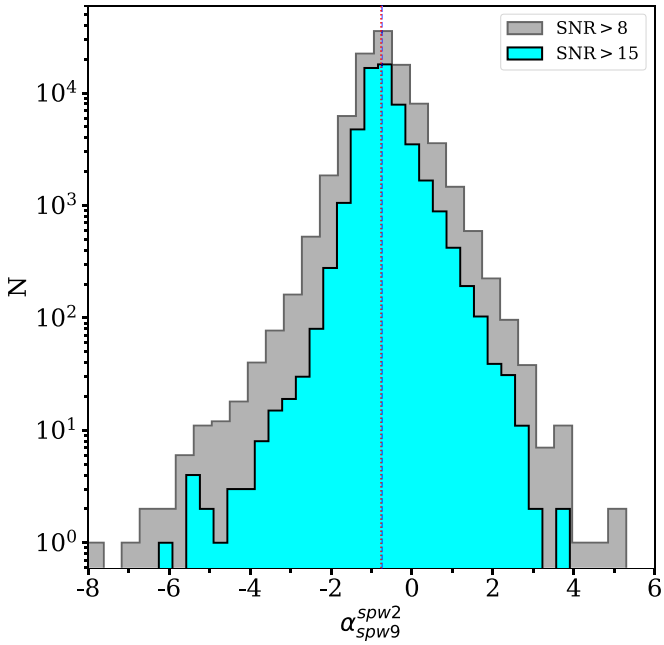

Figure 23. Spectral index (α^{spw2}_{spw9}) distribution of sources detected at S/N > 8 (median $\alpha = -0.736^{+0.003}_{-0.003}$) and at S/N > 15 (median $\alpha = -0.757^{+0.003}_{-0.003}$). The vertical lines mark the median spectral indices.

for sources selected at SPW2. The `plumber`-based measurements are flatter by ∼0.05 and also exhibit the same trend but with an offset as expected from Figure 22. Note that the systematic uncertainties due to the beam models are significantly larger than the errors (∼0.003) on mean spectral indices.

We also repeated the analysis for the subset of sources selected to be compact in both of the SPWs using the envelope presented in Figure 10. This selection primarily reduces the fraction of sources with extreme spectral indices ($|\alpha| > 3$). The median spectral index ($-0.685^{+0.003}_{-0.003}$) corresponding to the compact sources is flatter (dashed lines in the bottom row), but the trends with respect to the SPW2 and SPW9 flux densities are still apparent. In conclusion, a flattening of spectral indices at lower flux densities is indeed confirmed through our sample of 66,836 (SPW2) and 48,817 (SPW9) radio sources. For reference, we also show the median 1.4 GHz spectral indices obtained in two bins, ⩽4 mJy and >4 mJy at 1.4 GHz, by Prandoni et al. (2006) for a sample of 111 radio sources selected at 5 GHz. Higher-spatial-resolution imaging is required to confirm that the observed trend is indeed due to higher abundances of FRI, i.e., core-dominated population of radio sources in lower flux density bins.

Overall, the distribution of α^{spw2}_{spw9} in Figure 23 exhibits the presence of both flat ($\alpha^{spw2}_{spw9} > -0.5$) and steep ($\alpha^{spw2}_{spw9} < -0.5$) radio source populations. The former corresponds to core-dominated AGNs (Antonucci & Ulvestad 1985; Prandini & Ghisellini 2022) and latter to lobe-dominated AGNs (Saikia & Jamrozy 2009; Sirothia et al. 2013). A small fraction among these lobe-dominated AGNs are young radio sources (age $<10^5$ yr) that are often embedded in gas-rich environments, and may also exhibit a turnover at GHz frequencies, which is an indication of the subkiloparsec scale extent of the radio emission (O'Dea & Baum 1997; Orienti & Dallacasa 2014; Liao & Gu 2020; O'Dea & Saikia 2021). Also, present at the right end of the distribution in Figure 23 are sources with inverted spectra, with radio SED peaking at higher frequencies. These high-frequency peakers may be even younger than steep-spectrum sources (Stanghellini et al. 2009; Orienti & Dallacasa 2014). We will examine these aspects of the radio source population detected in MALS in the context of associated H I 21 cm absorption in future work.

5.2.3. Ultra-steep-spectrum Sources

Here, we focus on a special population of radio sources exhibiting ultra-steep-spectral indices ($\alpha < -1.3$) as prospective high-redshift radio galaxies (HzRGs; $z > 2$; Bornancini et al. 2007; Miley & De Breuck 2008; Saxena et al. 2018; Broderick et al. 2022). For this, we crossmatch all of the sources detected in SPW2 with the TGSS ADR1 (Intema et al. 2017) at 147 MHz. TGSS ADR1 has a spatial resolution of 25″ (median rms noise ∼3.5 mJy); therefore, we use a cross-matching radius of 10″ to maximize the coincidence of radio continuum peaks in the MALS and TGSS ADR1 images. We find counterparts for 34,735 sources of which 286 have $\alpha^{TGSSADR1}_{spw2} < -1.3$. The median SPW2 flux density for these sources is 5.5 mJy. The spectral indices and associated errors from this exercise are provided in columns `Spectral_MALS_Lit` and `Spectral_MALS_Lit_E`, respectively.

It is widely accepted in the literature that HzRGs are young and have compact morphology (Miley 1968; Neeser et al. 1995; Daly & Guerra 2002; Morabito et al. 2017). To discard sources that are clearly resolved in our sample, we visually inspected their SPW2 and SPW9 cutouts. A total of 90 sources were found to have extended emission and therefore discarded. Further, following the reliability criteria discussed in Section 3.3, we rejected any candidate HzRG that was within 3′ from the edge of the SPW2 primary beam. This led to a

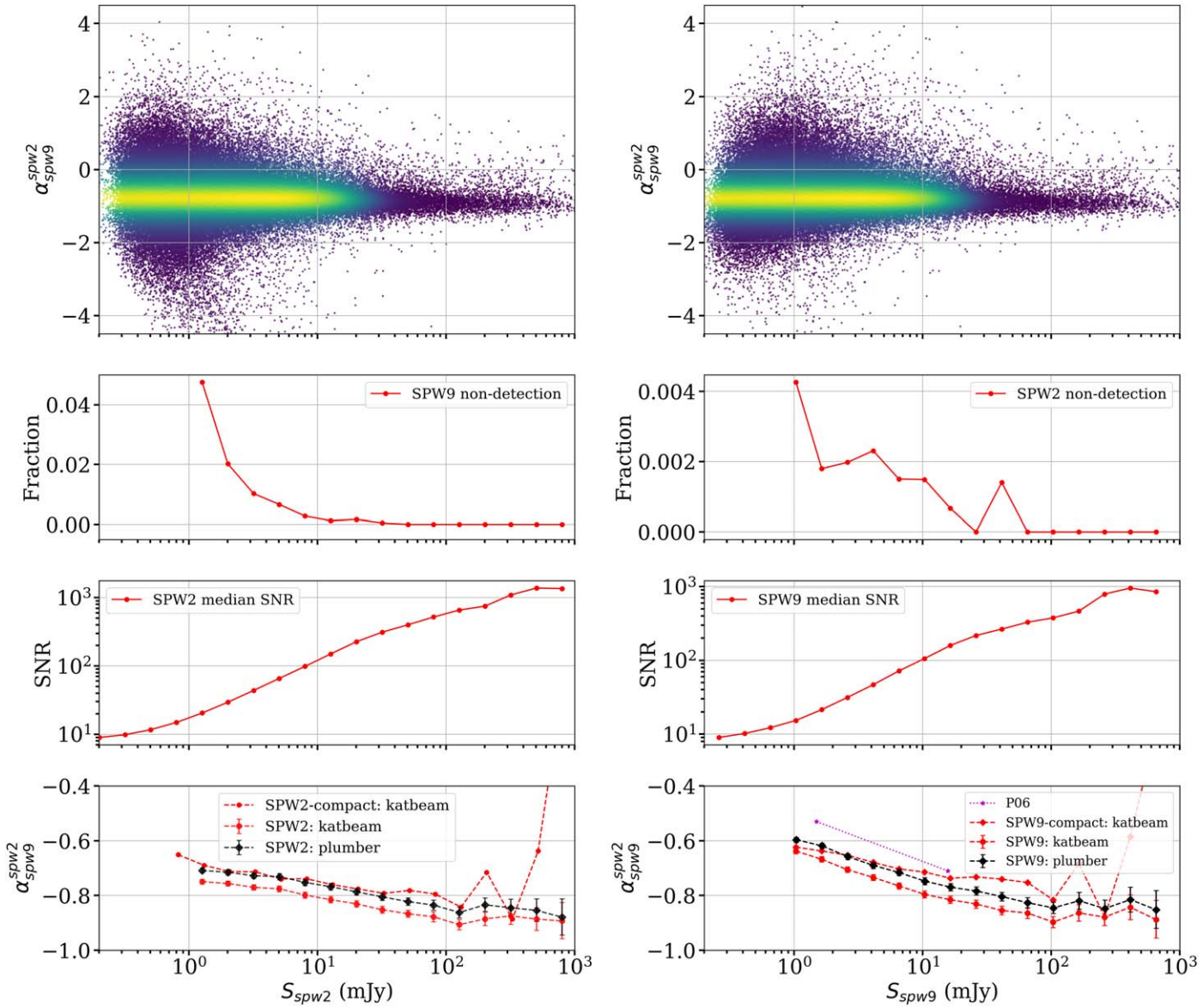

Figure 24. Spectral indices (α_{spw9}^{spw2}) as a function of flux density in SPW2 (left panels) and SPW9 (right panels). In the top row, the points are color coded according to their space density. The second row shows the fraction of upper (left) and lower (right) limits on spectral indices in each flux density bin. The third row shows the median S/N of sources in each bin. Note that the sources with S/N < 15 were excluded from the analysis. The median spectral indices calculated using survival analysis methods in bins of 0.2 dex in flux density are shown for both `katbeam` and `plumber` beam-corrected flux densities (bottom panels). The median spectral indices considering only compact sources for the case of `katbeam` model are also shown. For reference, 1.4 GHz measurements from Prandoni et al. (2006) (P06) are plotted in the bottom-right panel.

sample of 182 sources with spectral indices $\alpha_{spw2}^{\rm TGSSADR1} < -1.3$ and compact morphology on arcsecond scales.

In addition to having a steeper spectral index, nondetection in optical and/or infrared bands greatly enhances the probability of a source being at higher redshift. Therefore, we crossmatched the sample of remaining 182 candidate HzRGs with the *i*-band images from the Panoramic Survey Telescope and Rapid Response System (Pan-STARRS PS1; Chambers et al. 2016) and the AllWISE catalog from the Wide-field Infrared Survey Explorer (WISE; Wright et al. 2010; Cutri et al. 2014). The results of this crossmatching[26] by considering the nearest match within 2″ radius, chosen conservatively based on the astrometric accuracy of the MALS catalog, are reported in Table E1. In Table E1, a detection is marked as "True" and a nondetection is marked with "False." For convenience, we have added a column "Flag" to the table, the value of which for each source is based on detection in PS1 and WISE. Flag = 1 denotes 27 sources not detected in PS1 but detected in WISE. Flag = 2 denotes 113 sources not detected in both PS1 and WISE. Lower prospective candidates were given, Flag = 3: 14 sources detected in PS1 but not in WISE, and Flag = 4: 28 sources detected in both PS1 and WISE. The redshifts of eight sources, all at $z < 1$ and Flag = 4, are available from the NASA Extragalactic Database (NED; see last column of Table E1).

Overall, 140 sources with Flags 1 and 2 represent the prospective HzRG sample that needs further refinement through higher-spatial-resolution radio imaging, and then confirmation with infrared imaging and spectroscopy. In general, this candidate sample is expected to contain a mix of

[26] Thirty sources at $\delta < -30°$ were excluded from the PS1 crossmatch but are treated as nondetections in optical bands.

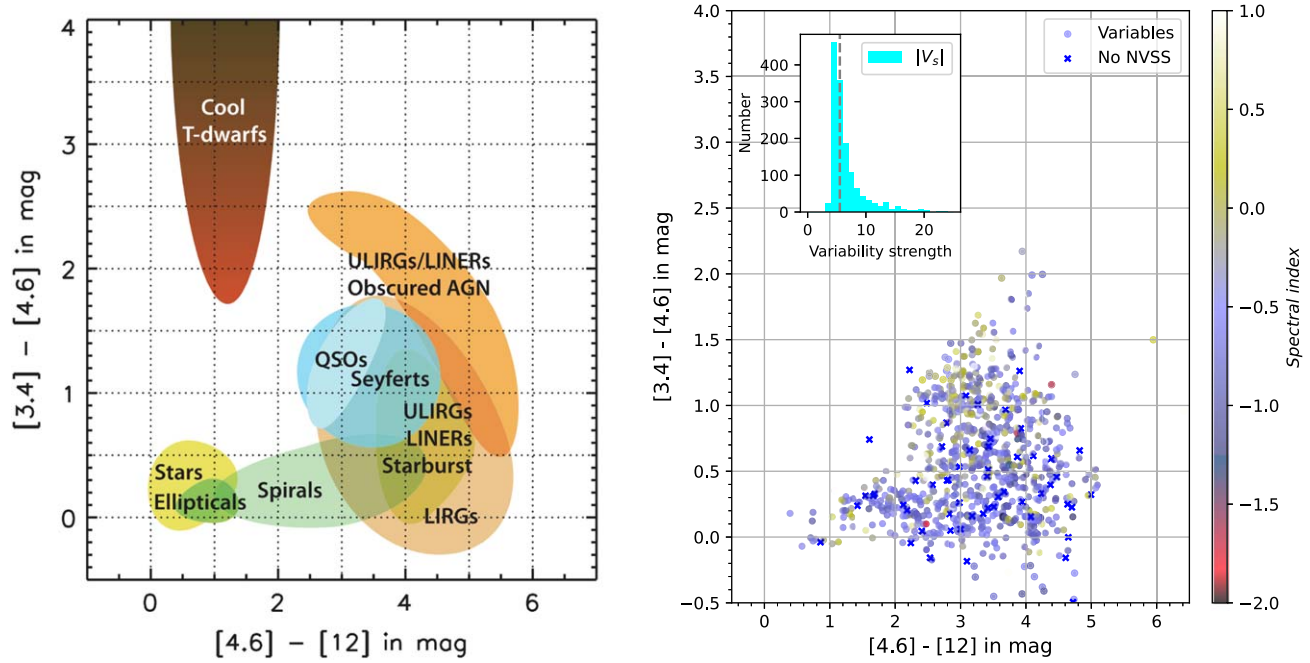

Figure 25. WISE color–color plot in Vega magnitudes of various classes of sources (left), reproduced from Wright et al. (2010) with permission, and variable radio sources from MALS (right). The points have been color coded based on spectral index, α_{spw9}^{spw2}. The inset in the right panel shows the distribution of variability strength ($|V_s|$), with the vertical dashed line marking the median value.

HzRGs and dust-obscured AGNs. The subset that are at $z < 1.5$ are expected to show H I 21 cm absorption in MALS *L*- and *UHF*-band spectroscopy. In a future paper, we will present an expanded sample of HzRG candidates using both *L*- and *UHF*-band continuum images from MALS, and report on the results from H I 21 cm absorption spectroscopy.

5.3. Long-term Radio Variability and Transients

The majority of NVSS observations were carried out between 1993 and 1996, i.e., about 26 yr prior to MALS *L*-band observations presented here. Here, we compare the SPW9 catalog with NVSS to identify variable and transient radio sources. We define the former to be detected in both NVSS and MALS, whereas the latter are detected only in one of these. We expect the majority of variable and transient radio sources to be compact at the arcsecond-scale resolutions of NVSS and MALS (e.g., Thyagarajan et al. 2011; Mooley et al. 2016). For unresolved sources brighter than 3.4 mJy, the NVSS catalog is 99% complete and has an rms position uncertainty of $<3''$ (see Figures 30 and 32 of Condon et al. 1998). Since the MALS SPW9 catalog is also nearly complete at this threshold flux density (Figure 21), we adopt 4.0 mJy as a stricter threshold to identify variable and transient sources.

For identifying variable sources, we consider 15,691 radio sources common between SPW9 and NVSS catalogs with the following properties: (i) brighter than 4.0 mJy and compact in NVSS, and (ii) isolated sources detected at S/N >8 in SPW9 with `Distance_NN` $>60''$ and `Distance_pointing` $<45'$, and (iii) SPW9—NVSS separation less than $3''$. These stringent criteria ensure that the positions of the selected sources are well-determined for the purpose of crossmatching with multiwavelength catalogs and minimize uncertainties due to a compact source being resolved in SPW9 or the presence of unrelated nearby source in either catalog, as already discussed in Section 5.2.

We measure random variation in the flux density of radio sources using χ^2 of the residuals around the mean flux density computed using the following equation:

$$\chi^2_{\rm obs} = \sum_{i=1}^{N} \frac{(S_i - \bar{S})^2}{\sigma_i^2}, \tag{6}$$

where

$$\bar{S} = \frac{\sum_{i=1}^{N} S_i/\sigma_i^2}{\sum_{i=1}^{N} 1/\sigma_i^2} \tag{7}$$

and S_i are N flux density measurements of a source with individual error σ_i. For MALS flux densities and errors, we adopted measurements based on the `plumber` beam model. Therefore, the NVSS flux densities have been modified assuming a spectral index of $\alpha = -0.7$ (Figure 22). Note that the selection of variables at low fractional variability ($f_{\rm var} = S_{\rm MALS} / S_{\rm NVSS}$) is affected by the MALS-to-NVSS offset of 1.06 (Section 4.2) and the choice of the beam model. For `katbeam` model, the sample would be smaller by ∼10% at $1 < f_{\rm var} < 1.15$.

For comparison with previous work, in addition to $f_{\rm var}$, we adopt two metrics to quantify the variability of the source. The first is the modulation index, $m = \sigma/\bar{S}$, where σ is the standard deviation of the flux density measurements. For the two-epoch variability relevant here, we define (Mooley et al. 2016; Hajela et al. 2019; Ross et al. 2021):

$$m = |\Delta S|/\bar{S}, \tag{8}$$

where $\Delta S = S_1 - S_2$, where S_1 and S_2 are two flux density measurements, and $\bar{S}$ is their mean as defined in Equation 7. The second quantity we adopt is variability strength, V_s,

defined as (Mooley et al. 2016; Hajela et al. 2019; Ross et al. 2021):

$$V_s = \frac{\Delta S}{\sqrt{\sigma_1^2 + \sigma_2^2}}. \quad (9)$$

V_s is expected to be distributed according to Student's t-distribution and may be preferred over χ^2-statistics when the degrees of freedom are small (Mooley et al. 2016).

We computed the abovementioned quantities for all 15,691 sources to produce a list of 1960 variable sources applying a 99.9% threshold based on χ^2 statistics. The arbitrary stringent threshold was adopted for practical reasons to generate a reasonable number of candidates, which can then be subjected to visual examination. This also yields a sample that is less affected by measurement uncertainties at low S/N. Indeed, the crucial process of visual examination revealed 631 candidates to be false. These are either imaging artifacts or the flux density comparison between MALS and NVSS is affected by the blending or proximity to a nearby source in NVSS or the splitting of a single source in NVSS into multiple components in MALS. We also omit 21 candidates corresponding to J0211 +1707 and J1833-2103, the pointings with extreme flux density offsets (see Section 4.2).

The list of 1308 variable targets is provided in Table F1. The distribution of $|V_s|$ (median = 5.5) is shown in an inset in Figure 25. The distribution of W_1, W_2, and W_3 colors of 763 sources detected in the AllWISE catalog are also shown in the *right* panel of Figure 25. The distribution of colors implies, as expected, that the majority of these variables are AGNs, although a few could also be stars.[27] The median radio spectral index (α_{spw9}^{spw2}) of the sample based on MALS SPW2 and SPW9 is $-0.65^{+0.02}_{-0.02}$, which is slightly flatter as compared to whole MALS SPW9 catalog (see Section 5.2). The errors define the 90% confidence level estimated by bootstrapping. The spectral indices are substantially flatter (median $\alpha_{spw9}^{spw2} = -0.48^{+0.04}_{-0.04}$) for the sources with color overlapping with the locus of powerful AGNs ($W_1 - W_2 > 0.5$; see also left panel of Figure 25), implying that a substantial fraction of these could be blazars.

The comparison between MALS and NVSS also revealed a subset of transients detected in NVSS but missing in the SPW9 catalog and vice versa. In summary, we identified 734 radio sources brighter than 4.0 mJy (S/N >8 ; `Distance_pointing` <45′) in the SPW9 catalog but no counterparts within 60″ in NVSS. In NVSS, there are 123 such radio sources with no counterparts within 60″ radius in the SPW9 catalog. Through visual inspection, we found only 115/734 and 7/123 to be *true* transients. The remaining are artifacts and false detections or misidentifications in NVSS. The median flux densities of radio sources explored among the transient candidates is 4.5 mJy, implying a large fraction is close to the detection limit of NVSS and is severely affected by incompleteness and source-finding inefficiencies. This is also implied by much larger fraction of transients detected with no counterparts in NVSS. A large fraction of these could simply be variable sources that were fainter during the NVSS observations, and hence missed. The distribution of 58 of these detected in the AllWISE catalog is shown in Figure 25, and is very similar to the colors of variables discussed above.

Further investigation of the variables and transients identified here requires inputs from multiepoch optical images and spectra. Even though only 30% of these have a counterpart within 2″ in Pan-STARRS (Chambers et al. 2016), other than being optically faint AGNs, a small fraction of these could also be supernovae and GRBs. This exploration is beyond the scope of this work and will be presented in a future paper.

6. Summary and Outlook

Through MALS (Gupta et al. 2016), we have observed 391 telescope pointings at the *L* band (900-1670 MHz) at declinations $\lesssim +20°$. For spectral line processing, the *L* band is split into 15 SPWs labeled SPW0–SPW14. This paper presents radio continuum images and a catalog of 495,325 (240,321) radio sources detected over an area of 2289 deg^2 (1132 deg^2) at 1006 MHz, i.e., SPW2 (1381 MHz, i.e., SPW9). This is the first of several data releases to come from MALS.

The 1381 MHz (SPW9) radio continuum images presented here have a spatial resolution of 8″ and rms noise of $\sim$22 μJy beam^{-1}. The catalog released here is primarily constructed from the cosine approximated analytic `katbeam` model (Mauch et al. 2020) but also provides measurements and corrections that can be used to obtain the values corresponding to the alternate beam model that implements holographic measurements through `plumber` (Sekhar et al. 2022). At 1381 MHz, the outcomes from these two models are in excellent agreement, but tend to diverge by a few percent in the outer regions (>45′ from the pointing center). Thus, the measurements in the outer regions may have larger systematic errors, and we advise caution in using these. Further improvements will follow from the application of primary beam corrections in the visibility plane via AW projection (Bhatnagar et al. 2013).

Through the analysis of 1150 multiply observed sources in MALS, we estimate the systematic uncertainties in astrometry and flux density scale ratio to be <1″ and 1% ($\sim$8% scatter). By comparing the positions and `katbeam`-based flux densities with NVSS and FIRST at 1.4 GHz, we establish the catalog's accuracy in astrometry and flux density scale to be better than 0.″8 and 6% (15% scatter), respectively. In comparison, with the `plumber` model we find a median flux density offset of 9% with respect to NVSS with an MAD of 16%, higher than the flux density offsets obtained using `katbeam`.

The majority ($\sim$90%) of sources in the catalog are modeled with single-Gaussian components, and only a few percent require three or more Gaussian components (median angular size $\sim$9.″8 in SPW9). We derived radio source counts from the catalogs at 1381 MHz and compared these with the existing measurements in the literature. Although not corrected for resolution and Eddington biases, the MALS counts show a good agreement—within 10%—with literature counts and remain complete down to 2 mJy, below which the counts rapidly decline. The slight offsets between source counts from various surveys could originate from instrumental and analysis effects, and need further investigations (Condon 2007).

For a matching radius of 6″, 205,435 sources are common between SPW2 and SPW9. We calculated spectral indices of 125,621 sources detected at S/N >8 in both of the SPWs. Using a sample of 66,836 (48,817) sources at SPW2 (SPW9), we confirm the flattening of spectral indices with decreasing

[27] Indeed, seven of these with a counterpart within 1″ in the Gaia catalog show significant (>3σ) proper motion (Gaia Collaboration et al. 2023).

flux density. This may be due to higher abundances of FRI, i.e., core-dominated population of radio sources in lower flux density bins. Using MALS SPW2 and TGSS ADR1 flux densities, we identify 182 USS sources, for which 140 due to optical-infrared properties are prime candidates for being HzRGs ($z > 2$). Through comparison with NVSS, we have identified the long-term variability (26 yr) of radio sources. We have determined 1308 variables (median variability strength, $|V_s| = 5.5$) and 122 transients, i.e., detected only in MALS or NVSS. These are primarily AGNs but may also comprise radio stars, supernovae, and GRBs. Further exploration of these will be presented in future papers.

The MALS SPW2 and SPW9 catalogs and primary beam-corrected Stokes-*I* images are available at https://mals.iucaa.in. We note that the calibration and imaging presented here, except for a static primary beam correction, do not correct for any direction-dependent errors. This will be addressed using AW-Projection (Bhatnagar et al. 2013) in future releases, which will also provide continuum and spectral line data products from the *L* and *UHF* bands.

Acknowledgments

We thank the anonymous referee for providing useful and detailed comments. We thank SARAO's team of engineers and commissioning scientists for years of intense and successful work toward delivering the wonderful MeerKAT telescope. The MeerKAT telescope is operated by the South African Radio Astronomy Observatory, which is a facility of the National Research Foundation, an agency of the Department of Science and Innovation. The MeerKAT data were processed using the MALS computing facility at IUCAA (https://mals.iucaa.in/releases). We thank Edward Wright and Chao-Wei Tsai for their permission to reproduce Figure 12 from Wright et al. (2010). K.M. and K.K. acknowledge support from the National Research Foundation of South Africa. The Common Astronomy Software Applications (CASA) package was developed by an international consortium of scientists based at the National Radio Astronomical Observatory (NRAO), the European Southern Observatory (ESO), the National Astronomical Observatory of Japan (NAOJ), the Academia Sinica Institute of Astronomy and Astrophysics (ASIAA), the CSIRO division for Astronomy and Space Science (CASS), and the Netherlands Institute for Radio Astronomy (ASTRON) under the guidance of NRAO. The National Radio Astronomy Observatory is a facility of the National Science Foundation operated under cooperative agreement by Associated Universities, Inc. This research has made use of the NASA/IPAC Extragalactic Database (NED), which is funded by the National Aeronautics and Space Administration and operated by the California Institute of Technology. This work has made use of data from the European Space Agency (ESA) mission Gaia (https://www.cosmos.esa.int/gaia), processed by the Gaia Data Processing and Analysis Consortium (DPAC; https://www.cosmos.esa.int/web/gaia/dpac/consortium). Funding for the DPAC has been provided by national institutions, in particular the institutions participating in the Gaia Multilateral Agreement.

Facility: MeerKAT

Software: ARTIP (Gupta et al. 2021), Astropy (The Astropy Collaboration et al. 2022), ASURV (Feigelson & Nelson 1985), CASA (THE CASA TEAM et al. 2022), katbeam (https://github.com/ska-sa/katbeam), Matplotlib (Hunter 2007), NumPy (Harris et al. 2020), plumber (Sekhar et al. 2022), and PyBDSF (Mohan & Rafferty 2015).

Appendix A
List of Pointings

Table A1 presents the list of 391 pointings observed during the first phase of MALS observations.

Table A1
All *L*-band MALS Pointings

Pointing ID	Date and Start Time (UTC)	σ_1^{SPW9} (μJy beam^{-1})	σ_2^{SPW9} (μJy beam^{-1})	S^{SPW9} (mJy)	Class	σ_1^{SPW2} (μJy beam^{-1})	σ_2^{SPW2} (μJy beam^{-1})	S^{SPW2} (mJy)	N_{src}^{SPW9}	N_{src}^{SPW2}
(1)	(2)	(3)	(4)	(5)	(6)	(7)	(8)	(9)	(10)	(11)
J000141.57−154040.6	2020-07-16T01:40	29.4	22.8	449.1	B	36.1	23.9	609.7	563	1347
J000234.52−052324.5	2020-08-19T20:40	27.2	23.7	248.8	A.2	40.8	33.5	326.8	690	1154
J000647.35+172815.4	2020-07-16T01:40	30.2	23.2	203.8	A.1	45.2	28.1	225.8	527	968
J001053.65−215703.9	2020-08-19T20:40	22.8	21.4	353.1	A.3	26.8	22.5	350.7	819	1813
J001508.49+082803.8	2020-07-16T01:40	29.1	24.0	428.9	A.3	46.2	30.7	519.4	592	1048
J001708.03−125624.9	2020-08-19T20:40	65.5	36.1	1065	B	73.8	43.3	1450	326	694
J002232.46+060804.6	2020-08-19T00:10	28.0	22.8	615.5	A.4	41.1	26.1	567.9	613	1224
J002355.84−235717.8	2020-08-19T00:10	23.2	21.3	215.6	A.1	29.0	23.6	285.2	744	1516
J002546.66−124725.2[a]	2020-08-19T00:10	32.4	23.5	432.6	B	496.8	189.2	1428	568	128
J021148.77+170723.2[b]	2020-09-12T22:45	47.1	34.5	762.0	A.4_R	59.6	40.9	911.4	472	942
J235722.47−073134.3	2020-09-09T21:35	27.8	22.4	247.2	A.2	39.4	26.2	295.1	648	1190
J235914.02+192420.6	2020-09-09T21:35	40.2	24.5	279.5	B	42.4	26.2	373.6	431	966

Notes. Column (1): pointing ID based on R.A. and decl. (J2000) of the bright radio source at the center of the pointing. Column (2): date and start time (UTC) of the observing run. Columns (3)–(5): rms at primary beam FWHM, rms at twice of the primary beam FWHM and flux density of the central radio source, for SPW9. Column (6): class of the pointing as described in Section 3.1. Column (7)–(9): rms at primary beam FWHM, rms at twice of the primary beam FWHM and flux density of the central radio source, for SPW2. Columns (10)–(11): total number of sources detected in the primary beam-corrected field for SPW9 and SPW2, respectively.
[a] Field removed from spectral index analysis (Section 5.2) owing to problematic SPW2 images. For the 50 representative pointings, _R is added to their class.
[b] One of the two pointings with extreme median flux density offset (Section 4.2) and Figure 17.

(This table is available in its entirety in machine-readable form.)

Appendix B
Catalog Columns

Table B1 provides a sample of the MALS SPW-based source catalog. Catalog column definitions are given in Table 3. Table B2 provides a sample of the Gaussian components (`N_Gauss`) for each source. These are linked to Table B1 through the parameter `Source_name`. Note the multiple occurrences of the "M"-type source in the table. The catalog column definitions are given in Table 3. The complete catalogs and images are available at https://mals.iucaa.in.

Table B1
Initial Six Rows from MALS SPW-based Source Catalog

Source_name (1)	Pointing_id (2)	Obs_date_U (3)	Obs_date_L (4)	Obs_band (5)	PBeamVersion (6)	Fluxcal (7)	Fluxscale (8)
J000719.65-153823.5	J000141.57-154040.6		["2020-07-16T01:40"]	*L*	katbeam_v0.1	["J1939-6342," "J0408-6545"]	["Stevens-Reynolds 2016," "MANUAL"]
J000710.64-152927.6	J000141.57-154040.6		["2020-07-16T01:40"]	*L*	katbeam_v0.1	["J1939-6342," "J0408-6545"]	["Stevens-Reynolds 2016," "MANUAL"]
J000708.60-152055.5	J000141.57-154040.6		["2020-07-16T01:40"]	*L*	katbeam_v0.1	["J1939-6342," "J0408-6545"]	["Stevens-Reynolds 2016," "MANUAL"]
J000708.20-153644.3	J000141.57-154040.6		["2020-07-16T01:40"]	*L*	katbeam_v0.1	["J1939-6342," "J0408-6545"]	["Stevens-Reynolds 2016," "MANUAL"]
J000705.44-155332.3	J000141.57-154040.6		["2020-07-16T01:40"]	*L*	katbeam_v0.1	["J1939-6342," "J0408-6545"]	["Stevens-Reynolds 2016," "MANUAL"]
J000659.56-152433.2	J000141.57-154040.6		["2020-07-16T01:40"]	*L*	katbeam_v0.1	["J1939-6342," "J0408-6545"]	["Stevens-Reynolds 2016," "MANUAL"]

SPW_id (9)	Ref_freq (MHz) (10)	Maj_restoring_beam (arcsec) (11)	Min_restoring_beam (arcsec) (12)	PA_restoring_beam (deg) (13)	Sigma_1 (μJy beam^{-1}) (14)	Sigma_2 (μJy beam^{-1}) (15)	Sigma_20 (μJy beam^{-1}) (16)	Distance_poitning (arcmin) (17)
Lspw_2	1005.94	10.8	8.9	−5.9	36.9	23.9	68.2	81.4
Lspw_2	1005.94	10.8	8.9	−5.9	36.9	23.9	68.2	80.0
Lspw_2	1005.94	10.8	8.9	−5.9	36.9	23.9	68.2	81.2
Lspw_2	1005.94	10.8	8.9	−5.9	36.9	23.9	68.2	78.7
Lspw_2	1005.94	10.8	8.9	−5.9	36.9	23.9	68.2	79.0
Lspw_2	1005.94	10.8	8.9	−5.9	36.9	23.9	68.2	78.3

Distance_NN (arcmin) (18)	S_Code (19)	N_Gauss (20)	Maxsep_Gauss (arcsec) (21)	Maj (arcsec) (22)	Maj_E (arcsec) (23)	Min (arcsec) (24)	Min_E (arcsec) (25)
3.2	S	1	−1	0.003046	0.000065	0.002559	0.000046
3.9	S	1	−1	0.004009	0.000526	0.003136	0.000343
4.2	S	1	−1	0.004841	0.000856	0.002783	0.000331
3.2	S	1	−1	0.003432	0.000721	0.002479	0.000384
3.8	S	1	−1	0.002837	0.000275	0.002489	0.000211
2.1	M	2	10.4	0.004325	0.000047	0.002412	0.000016

PA (deg) (26)	PA_E (deg) (27)	DC_Maj (arcsec) (28)	DC_Maj_E (arcsec) (29)	DC_Min (arcsec) (30)	DC_Min_E (arcsec) (31)	DC_PA (deg) (32)	DC_PA_E (deg) (33)
160.6	4.6	0.000000	0.000065	0.000000	0.000047	0.1	4.6
145.0	22.5	0.002831	0.000526	0.001658	0.000343	130.7	22.5
59.3	14.0	0.004114	0.000855	0.000000	0.000331	63.0	14.0
167.2	25.9	0.001670	0.000721	0.000000	0.000384	160.3	25.9
4.8	29.4	0.000000	0.000275	0.000000	0.000211	0.1	29.4
170.9	0.8	0.003105	0.000046	0.000000	0.000016	170.1	0.8

RA_mean (deg) (34)	RA_mean_E (deg) (35)	DEC_mean (deg) (36)	DEC_mean_E (deg) (37)	RA_max (deg) (38)	RA_max_E (deg) (39)	DEC_max (deg) (40)	DEC_max_E (deg) (41)
1.83187868637453	0.00002066615631	−15.6398776348322	0.00002698152798	1.83187868637453	0.00002066615631	−15.6398776348322	0.00002698152798
1.79433683090078	0.00017465334069	−15.4910060485520	0.00020171832911	1.79433683090078	0.00017465334069	−15.4910060485520	0.00020171832911
1.78587019980654	0.00032185228765	−15.3487510151291	0.00021979869525	1.78587019980654	0.00032185228765	−15.3487510151291	0.00021979869525
1.78419192604535	0.00017239690781	−15.6123271992311	0.00030099512716	1.78419192604535	0.00017239690781	−15.6123271992311	0.00030099512716
1.77266691158313	0.00008978010356	−15.8923209657271	0.00011654082226	1.77266691158313	0.00008978010356	−15.8923209657271	0.00011654082226
1.74818678200049	0.00001948799639	−15.4092218248728	0.00000729532113	1.74844056895094	0.00001948799639	−15.4092666854546	0.00000729532113

Total_flux (mJy) (42)	Total_flux_E (mJy) (43)	Total_flux_E_fit (mJy) (44)	Total_flux_E_sys (mJy) (45)	Total_flux_measured (mJy) (46)	Total_flux_measured_E (mJy) (47)	Peak_flux (mJy beam^{-1}) (48)	Peak_flux_E (mJy beam^{-1}) (49)
24.51	1.70	0.83	1.49	22.32	1.55	23.34	0.46
6.88	1.96	1.22	1.53	6.27	1.78	4.06	0.49
5.63	1.91	1.21	1.48	5.13	1.74	3.10	0.45
2.59	1.13	0.79	0.81	2.38	1.04	2.26	0.41
3.87	0.97	0.62	0.74	3.55	0.89	4.06	0.37
91.95	3.02	1.13	2.80	84.72	2.78	57.40	0.44

Isl_Total_flux (mJy) (50)	Isl_Total_flux_E (mJy) (51)	Isl_rms (mJy beam^{-1}) (52)	Isl_mean (mJy beam^{-1}) (53)	Resid_Isl_rms (mJy beam^{-1}) (54)	Resid_Isl_mean (mJy beam^{-1}) (55)	Flux_correction (56)	Spectral_index (57)	Spectral_index_E (58)
24.99	0.75	0.46	0.074	0.25	0.087	0.911	…	…
5.93	0.69	0.45	0.003	0.14	0.008	0.911	…	…
3.86	0.67	0.43	0.061	0.25	0.068	0.911	…	…
2.39	0.46	0.40	0.174	0.02	0.174	0.918	…	…
3.32	0.42	0.37	0.039	0.08	0.041	0.918	…	…
90.50	0.85	0.44	0.005	0.30	−0.032	0.921	…	…

Spectral_index _spwused (59)	Spectral_index _spwfit (60)	Spectral_index _spwfit_E (61)	Spectral_index _MALS_Lit (62)	Spectral_index _MALS_Lit_E (63)	Spectral_index _Lit (64)	Real _source (65)	Resolved (66)	Source _linked (67)
			[−0.501]	[0.084]	[“TGSS-ADR1,” “L:2”]	True	False	null
…	…	…	…	…	…	True	True	null
…	…	…	…	…	…	True	True	null
…	…	…	…	…	…	True	False	null
…	…	…	…	…	…	True	False	null
…	…	…	[−0.829]	[0.055]	[“TGSS-ADR1,” “L:2”]	True	True	null

Note. The catalog column definitions are given in Table 3. The complete catalog and the images are available at https://mals.iucaa.in.

Table B2
Gaussian Components (N_Gauss) for Each Source Presented in Table B1

Source_name	N_Gauss	G_RA (deg)	G_RA_E (deg)	G_DEC (deg)	G_DEC_E (deg)	G_Peak_flux (mJy beam^{-1})	G_Peak_flux_E (mJy beam^{-1})
(1)	(2)	(3)	(4)	(5)	(6)	(7)	(8)
J000719.65-153823.5	1	1.83187868637453	0.00002066615631	−15.6398776348321	0.00002698152798	23.34	0.46
J000710.64-152927.6	1	1.79433683090078	0.00017465334069	−15.4910060485520	0.00020171832911	4.06	0.49
J000708.60-152055.5	1	1.78587019980654	0.00032185228765	−15.3487510151291	0.00021979869525	3.10	0.45
J000708.20-153644.3	1	1.78419192604535	0.00017239690781	−15.6123271992311	0.00030099512716	2.26	0.41
J000705.44-155332.3	1	1.77266691158313	0.00008978010356	−15.8923209657271	0.00011654082226	4.06	0.37
J000659.56-152433.2	2	1.74799553848509	0.00000781826425	−15.4082879357922	0.00001157303107	56.79	0.45
J000659.56-152433.2	2	1.74858297350623	0.00001354648886	−15.4111268668004	0.00002044672516	30.58	0.44

G_Maj (arcsec)	G_Maj_E (arcsec)	G_Min (arcsec)	G_Min_E (arcsec)	G_PA (deg)	G_PA_E (deg)
(9)	(10)	(11)	(12)	(13)	(14)
10.964209	0.235017	9.214115	0.166663	160.6	4.6
14.433258	1.894917	11.290056	1.235068	145.0	22.5
17.427389	3.081403	10.016273	1.190850	59.3	14.0
12.354763	2.594940	8.922901	1.383234	167.2	25.9
10.212684	0.989746	8.958766	0.758822	4.8	29.3
11.280227	0.098207	9.221270	0.066132	176.2	1.4
10.861899	0.173346	8.841788	0.114819	0.5	2.8

G_DC_Maj (arcsec)	G_DC_Maj_E (arcsec)	G_DC_Min (arcsec)	G_DC_Min_E (arcsec)	G_DC_PA (deg)	G_DC_PA_E (deg)	G_id
(15)	(16)	(17)	(18)	(19)	(20)	(21)
0.000000	0.235017	0.000000	0.166663	0.0	4.6	1
10.193370	1.894917	5.968889	1.235068	130.7	22.5	2
14.809919	3.081403	0.000000	1.190849	63.0	14.0	3
6.011094	2.594940	0.000000	1.383233	160.3	25.9	4
0.000000	0.989746	0.000000	0.758822	0.0	29.4	5
3.232344	0.098207	2.361490	0.066132	17.9	1.4	6
0.000000	0.173346	0.000000	0.114819	0.0	2.8	7

Note. These are linked to Table B1 through the parameter Source_name. Note the multiple occurrences of the "M"-type source in the table. The catalog column definitions are given in Table 3. The complete catalog and the images are available at https://mals.iucaa.in.

Appendix C
MALS SPW2 and SPW9 Primary Beam Ratios

Table C1 presents the annular averaged MALS SPW2 and SPW9 primary beams generated using `katbeam` and `plumber`.

Table C1
MALS SPW2 and SPW9 Annular Averaged `katbeam` and `plumber`

Distance_pointing (1)	SPW2 `plumber` (2)	SPW2 `katbeam` (3)	SPW2 $\frac{\texttt{katbeam}}{\texttt{plumber}}$ (4)	SPW9 `plumber` (5)	SPW9 `katbeam` (6)	SPW9 $\frac{\texttt{katbeam}}{\texttt{plumber}}$ (7)	$\alpha_{\rm kat}/\alpha_{\rm plum}$ (8)
1	0.999	0.999	1.000	0.999	0.999	1.000	⋯
3	0.997	0.997	1.000	0.993	0.993	1.000	1.000
5	0.991	0.991	1.000	0.982	0.982	1.000	1.000
7	0.983	0.983	1.000	0.965	0.966	1.001	0.944
9	0.972	0.972	1.000	0.944	0.945	1.001	0.964
11	0.959	0.959	1.000	0.917	0.919	1.002	0.951
13	0.943	0.943	1.000	0.887	0.889	1.002	0.963
15	0.925	0.925	1.000	0.852	0.854	1.003	0.971
17	0.905	0.905	1.000	0.813	0.817	1.004	0.954
19	0.883	0.883	1.000	0.772	0.776	1.005	0.962
21	0.858	0.859	1.000	0.728	0.733	1.006	0.965
23	0.832	0.833	1.001	0.682	0.688	1.008	0.962
25	0.805	0.805	1.000	0.635	0.641	1.009	0.960
27	0.776	0.776	1.000	0.587	0.594	1.011	0.958
29	0.746	0.746	1.001	0.539	0.546	1.013	0.960
31	0.714	0.715	1.001	0.492	0.499	1.015	0.966
33	0.682	0.683	1.000	0.445	0.452	1.017	0.967
35	0.650	0.650	1.000	0.399	0.407	1.019	0.959
37	0.617	0.617	1.000	0.355	0.363	1.022	0.960
39	0.583	0.583	1.000	0.313	0.321	1.025	0.959
41	0.550	0.550	1.000	0.274	0.281	1.028	0.964
43	0.517	0.517	0.999	0.237	0.244	1.032	0.963
45	0.484	0.483	0.999	0.202	0.210	1.037	0.953
47	0.452	0.451	0.998	0.171	0.178	1.041	0.956
49	0.420	0.419	0.997	0.143	0.150	1.046	0.953
51	0.389	0.387	0.996	0.118	0.124	1.051	0.954
53	0.359	0.357	0.994	0.095	0.101	1.056	0.950
55	0.330	0.327	0.992	0.076	0.081	1.062	0.950
57	0.302	0.299	0.990	0.059	0.064	1.069	0.944
59	0.275	0.272	0.988	0.045	0.049	1.076	0.947
61	0.250	0.246	0.985	⋯	⋯	⋯	⋯
63	0.225	0.221	0.981	⋯	⋯	⋯	⋯
65	0.203	0.198	0.977	⋯	⋯	⋯	⋯
67	0.181	0.176	0.972	⋯	⋯	⋯	⋯
69	0.161	0.156	0.966	⋯	⋯	⋯	⋯
71	0.143	0.137	0.959	⋯	⋯	⋯	⋯
73	0.125	0.119	0.951	⋯	⋯	⋯	⋯
75	0.110	0.103	0.942	⋯	⋯	⋯	⋯
77	0.095	0.089	0.931	⋯	⋯	⋯	⋯
79	0.082	0.075	0.919	⋯	⋯	⋯	⋯

Note. Column (1): distance from the pointing center in arcminutes. Columns (2) and (3): annular averaged `plumber` beam and `katbeam`, respectively, for SPW2. Column (4): ratio between annular averaged `katbeam` and `plumber` beam for SPW2. Columns (5) and (6): annular averaged `plumber` beam and `katbeam`, respectively, for SPW9. Column (7): ratio of annular averaged `katbeam` and `plumber` beam for SPW9. Column (8): ratio of spectral indices corresponding to the two beam models.

Appendix D
MALS SPW9 Source Counts

Table D1 presents radio source counts derived from the SPW9 catalog.

Table D1
MALS 1.4 GHz Radio Source Counts

ΔS (mJy)	log[S (Jy)]	N	Area (deg^2)	$\frac{dN}{dS} S^{2.5}$ (Jy$^{1.5}$ sr^{-1})
0.16–0.25	−3.7	18315	108.2	$3.3708^{+0.0249}_{-0.0249}$
0.25–0.40	−3.5	36764	331.8	$4.4030^{+0.0230}_{-0.0230}$
0.40–0.63	−3.3	39717	552.3	$5.7011^{+0.0286}_{-0.0286}$
0.63–1.00	−3.1	32942	751.5	$6.9341^{+0.0382}_{-0.0382}$
1.00–1.58	−2.9	26201	930.6	$8.8867^{+0.0549}_{-0.0549}$
1.58–2.51	−2.7	20713	1038.0	$12.5661^{+0.0873}_{-0.0873}$
2.51–3.98	−2.5	15548	1057.7	$18.471^{+0.148}_{-0.148}$
3.98–6.31	−2.3	11666	1063.0	$27.516^{+0.255}_{-0.255}$
6.31–10.00	−2.1	8726	1064.6	$41.000^{+0.439}_{-0.439}$
10.00–15.85	−1.9	6330	1065.3	$59.306^{+0.745}_{-0.745}$
15.85–25.12	−1.7	4524	1065.7	$84.54^{+1.26}_{-1.26}$
25.12–39.81	−1.5	3194	1065.9	$119.07^{+2.11}_{-2.11}$
39.81–63.10	−1.3	2133	1066.0	$158.64^{+3.44}_{-3.44}$
63.10–100.00	−1.1	1383	1066.0	$205.24^{+5.52}_{-5.52}$
100.00–158.49	−0.9	887	1066.0	$262.6^{+8.8}_{-8.8}$
158.49–251.19	−0.7	535	1066.0	320^{+14}_{-14}
251.19–398.11	−0.5	281	1066.0	330^{+20}_{-20}
398.11–630.96	−0.3	166	1066.0	390^{+30}_{-30}
630.96–1000.00	−0.1	79	1066.0	370^{+42}_{-42}
1000.00–1584.89	0.1	38	1066.0	360^{+68}_{-58}
1584.89–2511.89	0.3	11	1066.0	210^{+83}_{-61}
2511.89–3981.07	0.5	7	1066.0	300^{+100}_{-100}
3981.07–6309.57	0.7	5	1066.0	400^{+300}_{-200}
6309.57–10000.00	0.9	3	1066.0	400^{+400}_{-200}

Note. Column (1): flux density range of each bin in mJy. Column (2): log of mean flux density of each bin in Jy. Column (3): number of sources detected in each bin. Column (4): total survey area in square degrees in which a source with the mean flux density of the bin can be detected at more than 5σ threshold. Column (5): Euclidean normalized differential source counts.

Appendix E
List of USS as Candidate HzRGs

Table E1 presents the list of USS identified as promising HzRG candidates. Note that the redshifts of eight sources, all at $z < 1$ and Flag = 4, are available from the literature. For completeness, these are included in the table. The candidates with Flags 1 and 2 constitute the most promising candidates.

Table E1
List USS as Candidate HzRGs

ID (J2000) (1)	S_Code (2)	Flux Density (mJy) (3)	$\alpha_{SPW2}^{TGSSADR1} \pm \sigma_\alpha$ (4)	PS1 (5)	WISE (6)	Flag (7)	z (8)	Ref. z (9)
J122204.80−134745.8	S	11.1	-1.57 ± 0.05	False	False	2	⋯	⋯
J231750.42−410627.7	S	4.29	-1.53 ± 0.07	⋯	True	1	⋯	⋯
J155624.36+031906.4	M	8.91	-1.34 ± 0.06	False	False	2	⋯	⋯
J233125.38+141819.2	S	2.64	-1.36 ± 0.09	False	False	2	⋯	⋯
J160615.40−153738.5	S	10.6	-1.38 ± 0.06	False	False	2	⋯	⋯
J160530.70−142315.0	S	4.70	-1.34 ± 0.09	False	True	1	⋯	⋯
J064045.47−320104.1	S	4.04	-1.48 ± 0.08	⋯	False	2	⋯	⋯
J122705.51+041654.3	S	31.9	-1.38 ± 0.07	True	True	4	0.305	Albareti et al. (2017)

Note. Column (1): source ID (J2000). Column (2): S_Code (defined in Table 3) from PyBDSF catalog. Column (3): total integrated flux density from SPW2. Column (4): spectral index and its associated uncertainty based on TGSS ADR1 (147 MHz) and SPW2 measurements. Column (5): counterpart in PS1? Column (6): counterpart in WISE? Column (7): Boolean flag based on PS1 and WISE matching; 1 = detected in WISE but not in PS1, 2 = not detected in both, 3 = detected in PS1 but not in WISE, and 4 = detected in both. Column (8): redshift measurements from NED. Column (9): reference for redshift measurement.
References. Bornancini et al. (2007), Alam et al. (2015), Albareti et al. (2017).

(This table is available in its entirety in machine-readable form.)

Appendix F
List of Variable Radio Sources

Table F1 presents the list of variable radio sources.

Table F1
List of Variable Radio Sources Providing Variability Strength (V_s), Modulation Index (m), and Fractional Variability (f_{var})

ID (J2000)	V_s	m	f_{var}
J035422.58-252049.9	5.72	0.26	1.35
J035130.75-243919.2	43.40	0.87	2.81
J034906.59-252914.4	5.27	0.57	1.67
J035318.51-024411.8	−6.88	0.29	0.77
J035023.88-035626.3	6.96	0.34	1.50
J034720.50-035418.4	6.69	0.20	1.24
J162849.11-131055.4	5.21	0.30	1.42
J162600.57-130147.1	4.24	0.30	1.41
J163145.15-142111.2	4.90	0.19	1.23
J162952.03-145721.4	5.69	0.17	1.19
J162835.24-144855.1	4.64	0.37	1.56

(This table is available in its entirety in machine-readable form.)

ORCID iDs

P. P. Deka https://orcid.org/0000-0001-9174-1186
N. Gupta https://orcid.org/0000-0001-7547-4241
P. Jagannathan https://orcid.org/0000-0002-5825-9635
S. Sekhar https://orcid.org/0000-0002-8418-9001
E. Momjian https://orcid.org/0000-0003-3168-5922
S. Bhatnagar https://orcid.org/0000-0001-7164-0089
S. A. Balashev https://orcid.org/0000-0002-3814-9666
F. Combes https://orcid.org/0000-0003-2658-7893
M. Hilton https://orcid.org/0000-0002-8490-8117
K. L. Emig https://orcid.org/0000-0001-6527-6954
G. I. G. Józsa https://orcid.org/0000-0003-0608-6258
K. Knowles https://orcid.org/0000-0002-8452-0825
J.-K. Krogager https://orcid.org/0000-0002-4912-9388
K. Moodley https://orcid.org/0000-0001-6606-7142
Sébastien Muller https://orcid.org/0000-0002-9931-1313
P. Noterdaeme https://orcid.org/0000-0002-5777-1629
P. Salas https://orcid.org/0000-0001-8271-0572

References

Abazajian, K. N., Adelman-McCarthy, J. K., Agüeros, M. A., et al. 2009, ApJS, 182, 543
Alam, S., Albareti, F. D., Allende Prieto, C., et al. 2015, ApJS, 219, 12
Albareti, F. D., Allende Prieto, C., Almeida, A., et al. 2017, ApJS, 233, 25
Algera, H. S. B., Hodge, J. A., Riechers, D., et al. 2021, ApJ, 912, 73
Algera, H. S. B., van der Vlugt, D., Hodge, J. A., et al. 2020, ApJ, 903, 139
An, F., Vaccari, M., Smail, I., et al. 2021, MNRAS, 507, 2643
Antonucci, R. R. J., & Ulvestad, J. S. 1985, ApJ, 294, 158
Baum, S. A., O'Dea, C. P., Murphy, D. W., & de Bruyn, A. G. 1990, A&A, 232, 19
Becker, R. H., White, R. L., & Helfand, D. J. 1995, ApJ, 450, 559
Bhatnagar, S., Rau, U., & Golap, K. 2013, ApJ, 770, 91
Bicknell, G. V., Dopita, M. A., & O'Dea, C. P. O. 1997, ApJ, 485, 112
Boettcher, E., Chen, H.-W., Zahedy, F. S., et al. 2021, ApJ, 913, 18
Bonaldi, A., An, T., Brüggen, M., et al. 2021, MNRAS, 500, 3821
Bondi, M., Ciliegi, P., Schinnerer, E., et al. 2008, ApJ, 681, 1129
Bornancini, C. G., De Breuck, C., de Vries, W., et al. 2007, MNRAS, 378, 551
Broderick, J. W., Drouart, G., Seymour, N., et al. 2022, PASA, 39, e061
Chambers, K. C., Magnier, E. A., Metcalfe, N., et al. 2016, arXiv:1612.05560
Combes, F., Gupta, N., Muller, S., et al. 2021, A&A, 648, A116
Condon, J. J. 1992, ARA&A, 30, 575
Condon, J. J. 2007, in ASP Conf. Ser. 380, Deepest Astronomical Surveys, ed. J. Afonso et al. (San Francisco, CA: ASP), 189
Condon, J. J., Cotton, W. D., Greisen, E. W., et al. 1998, AJ, 115, 1693
Cordes, J. M., Lazio, T. J. W., & McLaughlin, M. A. 2004, NewAR, 48, 1459
Cornwell, T. J., Uson, J. M., & Haddad, N. 1992, A&A, 258, 583
Cutri, R. M., Wright, E. L., Conrow, T., et al. 2014, yCat, II/328
Daly, R. A., & Guerra, E. J. 2002, AJ, 124, 1831
Davoust, E., & Considere, S. 1995, A&AS, 110, 19
de Gasperin, F., Intema, H. T., & Frail, D. A. 2018, MNRAS, 474, 5008
de Villiers, M. S. 2023, AJ, 165, 78
de Vries, N., Snellen, I. A. G., Schilizzi, R. T., Mack, K.-H., & Kaiser, C. R. 2009, A&A, 498, 641
de Vries, W. H., Barthel, P. D., & O'Dea, C. P. 1997, A&A, 321, 105
Eddington, A. S. 1913, MNRAS, 73, 359
Eddington, A. S. S. 1940, MNRAS, 100, 354
Emig, K. L., Gupta, N., Salas, P., et al. 2023, ApJ, 944, 93
Fanaroff, B. L., & Riley, J. M. 1974, MNRAS, 167, 31P
Fanidakis, N., Baugh, C. M., Benson, A. J., et al. 2012, MNRAS, 419, 2797
Feigelson, E. D., & Nelson, P. I. 1985, ApJ, 293, 192
Gaia Collaboration, Vallenari, A., Brown, A. G. A., et al. 2023, A&A, 674, A1
Garn, T., Green, D. A., Riley, J. M., & Alexander, P. 2008, MNRAS, 383, 75
Gordon, Y. A., Boyce, M. M., O'Dea, C. P., et al. 2021, ApJS, 255, 30
Greisen, E. W. 2003, in AIPS, the VLA, and the VLBA, ed. A. Heck (Dordrecht: Springer), 109
Gupta, N., Jagannathan, P., Srianand, R., et al. 2021, ApJ, 907, 11
Gupta, N., Shukla, G., Srianand, R., et al. 2022, ApJ, 929, 108

Gupta, N., Srianand, R., Baan, W., et al. 2016, in Proc. of Science 277, Proceedings of MeerKAT Science: On the Pathway to the SKA, ed. R. Taylor (Trieste: SISSA)
Hajela, A., Mooley, K. P., Intema, H. T., & Frail, D. A. 2019, MNRAS, 490, 4898
Hale, C. L., McConnell, D., Thomson, A. J. M., et al. 2021, PASA, 38, e058
Hale, C. L., Whittam, I. H., Jarvis, M. J., et al. 2023, MNRAS, 520, 2668
Harris, C. R., Millman, K. J., van der Walt, S. J., et al. 2020, Natur, 585, 357
Heckman, T. M., & Best, P. N. 2014, ARA&A, 52, 589
Heywood, I., Jarvis, M. J., Hale, C. L., et al. 2022, MNRAS, 509, 2150
Hopkins, A. M., & Beacom, J. F. 2006, ApJ, 651, 142
Hopkins, A. M., Miller, C. J., Connolly, A. J., et al. 2002, AJ, 123, 1086
Hunter, J. D. 2007, CSE, 9, 90
Hurley-Walker, N., Callingham, J. R., Hancock, P. J., et al. 2017, MNRAS, 464, 1146
Hurley-Walker, N., Galvin, T. J., Duchesne, S. W., et al. 2022, PASA, 39, e035
Ibar, E., Ivison, R. J., Biggs, A. D., et al. 2009, MNRAS, 397, 281
Intema, H. T., Jagannathan, P., Mooley, K. P., & Frail, D. A. 2017, A&A, 598, A78
Isobe, T., Feigelson, E. D., & Nelson, P. I. 1985, BAAS, 17, 573
Jarvis, M. J., Taylor, A. R., Agudo, I., et al. 2016, in Proc. of Science 277, Proceedings of MeerKAT Science: On the Pathway to the SKA, ed. R. Taylor et al. (Trieste: SISSA), 6
Jonas, J. & MeerKAT Team 2016, in Proc. of Science 277, Proc. of MeerKAT Science: On the Pathway to the SKA, ed. R. Taylor (Trieste: SISSA), 1
Jones, P. A., & McAdam, W. B. 1992, ApJS, 80, 137
Kameno, S., Horiuchi, S., Shen, Z.-Q., et al. 2000, PASJ, 52, 209
Keim, M. A., Callingham, J. R., & Röttgering, H. J. A. 2019, A&A, 628, A56
Krogager, J. K., Gupta, N., Noterdaeme, P., et al. 2018, ApJS, 235, 10
Lacy, M., Baum, S. A., Chandler, C. J., et al. 2020, PASP, 132, 035001
Liao, M., & Gu, M. 2020, MNRAS, 491, 92
Linden, S. T., Murphy, E. J., Dong, D., et al. 2020, ApJS, 248, 25
Maina, E. K., Mohapatra, A., Józsa, G. I. G., et al. 2022, MNRAS, 516, 2050
Mandal, S., Prandoni, I., Hardcastle, M. J., et al. 2021, A&A, 648, A5
Matthews, A. M., Condon, J. J., Cotton, W. D., & Mauch, T. 2021, ApJ, 909, 193
Mauch, T., Cotton, W. D., Condon, J. J., et al. 2020, ApJ, 888, 61
Mauch, T., Murphy, T., Buttery, H. J., et al. 2003, MNRAS, 342, 1117
McConnell, D., Hale, C. L., Lenc, E., et al. 2020, PASA, 37, e048
Miley, G., & De Breuck, C. 2008, A&ARv, 15, 67
Miley, G. K. 1968, Natur, 218, 933
Mohan, N., & Rafferty, D., 2015 PyBDSF: Python Blob Detection and Source Finder, Astrophysics Source Code Library, ascl:1502.007
Mooley, K. P., Hallinan, G., Bourke, S., et al. 2016, ApJ, 818, 105
Morabito, L. K., Williams, W. L., Duncan, K. J., et al. 2017, MNRAS, 469, 1883
Murgia, M., Fanti, C., Fanti, R., et al. 1999, A&A, 345, 769
Murphy, E. J., Condon, J. J., Schinnerer, E., et al. 2011, ApJ, 737, 67
Neeser, M. J., Eales, S. A., Law-Green, J. D., Leahy, J. P., & Rawlings, S. 1995, ApJ, 451, 76
Niklas, S., Klein, U., & Wielebinski, R. 1997, A&A, 322, 19
Norris, R. P., Marvil, J., Collier, J. D., et al. 2021, PASA, 38, e046
O'Dea, C. P., & Baum, S. A. 1997, AJ, 113, 148
O'Dea, C. P., & Saikia, D. J. 2021, A&ARv, 29, 3
Orienti, M., & Dallacasa, D. 2014, MNRAS, 438, 463
Owen, F. N. 2018, ApJS, 235, 34
Padovani, P., Alexander, D. M., Assef, R. J., et al. 2017, A&ARv, 25, 2
Partridge, B., López-Caniego, M., Perley, R. A., et al. 2016, ApJ, 821, 61
Perley, R. A., & Butler, B. J. 2017, ApJS, 230, 7
Planck Collaboration, Aghanim, N., Akrami, Y., et al. 2020, A&A, 641, A6
Prandini, E., & Ghisellini, G. 2022, Galax, 10, 35
Prandoni, I., Guglielmino, G., Morganti, R., et al. 2018, MNRAS, 481, 4548
Prandoni, I., Parma, P., Wieringa, M. H., et al. 2006, A&A, 457, 517
Rau, U., & Cornwell, T. J. 2011, A&A, 532, A71
Rengelink, R. B., Tang, Y., de Bruyn, A. G., et al. 1997, A&AS, 124, 259
Ricci, R., Prandoni, I., De Ruiter, H. R., & Parma, P. 2019, A&A, 621, A19
Ross, K., Callingham, J. R., Hurley-Walker, N., et al. 2021, MNRAS, 501, 6139
Rybicki, G. B., & Lightman, A. P. 1979, Radiative Processes in Astrophysics (New York: Wiley-Interscience)
Saikia, D. J., & Gupta, N. 2003, A&A, 405, 499
Saikia, D. J., & Jamrozy, M. 2009, BASI, 37, 63
Saxena, A., Jagannathan, P., Röttgering, H. J. A., et al. 2018, MNRAS, 475, 5041
Sekhar, S., Jagannathan, P., Kirk, B., Bhatnagar, S., & Taylor, R. 2022, AJ, 163, 87
Seymour, N., Dwelly, T., Moss, D., et al. 2008, MNRAS, 386, 1695
Shimwell, T. W., Hardcastle, M. J., Tasse, C., et al. 2022, A&A, 659, A1
Shimwell, T. W., Röttgering, H. J. A., Best, P. N., et al. 2017, A&A, 598, A104
Shimwell, T. W., Tasse, C., Hardcastle, M. J., et al. 2019, A&A, 622, A1
Silverman, J. D., Lamareille, F., Maier, C., et al. 2009, ApJ, 696, 396
Simpson, C., Martínez-Sansigre, A., Rawlings, S., et al. 2006, MNRAS, 372, 741
Sirothia, S. K., Gopal-Krishna, & Wiita, P. J. 2013, ApJL, 765, L11
Smolčić, V., Delvecchio, I., Zamorani, G., et al. 2017a, A&A, 602, A2
Smolčić, V., Novak, M., Bondi, M., et al. 2017b, A&A, 602, A1
Snellen, I. A. G., Schilizzi, R. T., Miley, G. K., et al. 2000, MNRAS, 319, 445
Srianand, R., Gupta, N., Petitjean, P., et al. 2022, MNRAS, 516, 1339
Stanghellini, C., Dallacasa, D., & Orienti, M. 2009, AN, 330, 223
Stein, M., Heesen, V., Dettmar, R. J., et al. 2023, A&A, 670, A158
Tabatabaei, F. S., Schinnerer, E., Krause, M., et al. 2017, ApJ, 836, 185
The Astropy Collaboration, Price-Whelan, A. M., Lim, P. L., et al. 2022, ApJ, 935, 167
THE CASA TEAM, Bean, B., Bhatnagar, S., et al. 2022, PASP, 134, 114501
Thyagarajan, N., Helfand, D. J., White, R. L., & Becker, R. H. 2011, ApJ, 742, 49
Tiwari, P. 2019, RAA, 19, 096
van der Vlugt, D., Algera, H. S. B., Hodge, J. A., et al. 2021, ApJ, 907, 5
Wagenveld, J. D., Klöckner, H. R., Gupta, N., et al. 2023, A&A, 673, A113
White, R. L., Becker, R. H., Helfand, D. J., & Gregg, M. D. 1997, ApJ, 475, 479
Wright, E. L., Eisenhardt, P. R. M., Mainzer, A. K., et al. 2010, AJ, 140, 1868